

# A Conservative Nodal Variational Multiscale Method for Lagrangian Shock Hydrodynamics.<sup>☆</sup>

G. Scovazzi<sup>a,\*</sup>, J. N. Shadid<sup>b</sup>, E. Love<sup>a</sup>, W. J. Rider<sup>a</sup>

<sup>a</sup>1431 Computational Shock- and Multi-physics Department, Sandia National Laboratories,  
P.O. Box 5800, MS 1319, Albuquerque, NM 87185-1319, USA

<sup>b</sup>1437 Electrical and Microsystem Modeling Department, Sandia National Laboratories,  
P.O. Box 5800, MS 0378, Albuquerque, NM 87185-0378, USA

---

## Abstract

A new method based on a continuous, piece-wise linear approximation of the equations for Lagrangian shock hydrodynamics is presented. Numerical instabilities are controlled by a stabilizing operator derived using the paradigm of the variational multiscale analysis. Encouraging numerical comparisons with existing methods in the case of quadrilateral and hexahedral elements indicate that the proposed method is capable of preventing hourglass patterns in the solution, while maintaining accuracy in regions of smooth flow. The proposed approach satisfies Galilean invariance properties and hinges upon the interpretation of the Lagrangian shock hydrodynamics equations as a system of nonlinear wave equations. A specific implementation in terms of a predictor/multi-corrector version of the mid-point time integrator guarantees global conservation of mass, momentum, and total energy for each iterate. Stability and formal order of accuracy are investigated applying the von Neumann analysis to the linearized shock hydrodynamics equations in one dimension. This approach yields tight bounds for stable time-step estimation, formal second-order accuracy of the method in time and space, and valuable indications on the choice of the most appropriate values for the stabilization parameters present in the formulation.

**Key words:** Lagrangian shock hydrodynamics, stabilized methods, variational multiscale analysis, updated Lagrangian formulation, hourglass control, nodal finite element method.

---

## 1. Introduction

In recent years, renewed effort has been devoted to the technical advancement of Lagrangian shock hydrodynamics algorithms (*hydrocodes* in short), spurred by the current and foreseeable computational challenges in terms of physical and geometric complexity (for a non-exhaustive list of publications on this topic, see [2, 3, 5, 6, 9–11, 13, 14, 19, 20, 40–46, 53, 55, 56]). In particular, the developments in [3, 9–11, 13, 14, 44–46] focussed on improving the robustness of simulations with respect to mesh distortion, while maintaining second-order accuracy in smooth regions of the flow.

This article presents a new stabilization concept in which the variational multiscale approach [26, 27, 33] is applied to Lagrangian shock hydrodynamic flows in combination with piece-wise linear, continuous finite element approximations. Specifically, the proposed method adopts a continuous piece-wise linear approximation of both thermodynamic and kinematic variables. This is in contrast with more traditional approaches

in shock hydrodynamics, which rely on a piece-wise constant discretization of the thermodynamic variables. A multiscale decomposition of the solution into coarse (discretely representable) scales and fine (subgrid) scales is adopted. An approximation of the subgrid-scale component of the solution is used to control instabilities of acoustic type, which are typically responsible for spurious hourglass modes in the case of quadrilateral/hexahedral elements, or pressure instabilities (often referred to as element artificial stiffness) in the case of triangular/tetrahedral elements (see [4, 25] for a detailed introduction to the subject). The solution enrichment by fine-scale subgrid contributions provides enhanced stability without reducing accuracy, as the method relies on residual-based (therefore variationally consistent) approximations of the fine scales (see also [57]). Stabilization operators are developed in the context of smooth flows, and need to be complemented by appropriate discontinuity capturing operators (e.g., artificial viscosities [65]), whenever shock wave discontinuities are expected.

The present work stems from earlier work [52, 53], and represents a considerable advance from many points of view. The method leverages a variational formulation of the shock hydrodynamics equations in updated Lagrangian form, for which most integrals are computed directly in the current configuration (see [4] for details on this nomenclature). This strategy contrasts with the formulation in [53], which was posed in the original configuration (total or pure Lagrangian approach [4]),

---

<sup>☆</sup>This research was partially funded by the DOE NNSA Advanced Scientific Computing Program and the Computer Science Research Institute at Sandia National Laboratories. Sandia is a multiprogram laboratory operated by Sandia Corporation, a Lockheed Martin Company, for the United States Department of Energy under contract DEAC04-94-AL85000.

\*Corresponding author

Email addresses: gscovaz@sandia.gov (G. Scovazzi)

and allows for a reduction in the computational costs. In fact, the deformation gradient mapping from the original to the current configuration does not need to be evaluated explicitly, but is implicitly calculated by updating the coordinates of the mesh nodes. In addition, algorithms for fast dynamics posed in the current configuration usually enjoy improved discrete invariance and objectivity properties relative to corresponding algorithms cast in the original configuration. This is due to the fact that the discretization of the unsymmetric Piola stress tensor does not always preserve the same invariance properties of the analytical counterpart (see [4, 25, 39, 59] and references therein, for more details).

The proposed method is implemented using a second-order predictor/multi-corrector, mid-point type time integration procedure similar to [55, 56], to preserve at each iteration global mass, momentum, and total energy. This is in contrast to the predictor/multi-corrector space-time integrator proposed in [53], in which conservation is guaranteed only when convergence of the iterative process is attained. It is also important to appreciate that the general variational multi-scale approach is not limited in applicability to mid-point type integrators, but can be extended - with minor modifications - to a larger class of time integrators, including, for example, explicit Runge-Kutta methods.

In the current implementation, lumped mass matrices are used to integrate in time the momentum and internal energy equations, providing increased robustness under severe shock conditions. One of the problematic issues discovered in the development of the algorithm presented in [53] was that negative undershoots of the pressure and internal energy could occur in a number of challenging test cases. The combination of mass lumping with the new time-integrator has eliminated this problem. This result is very important especially when complex constitutive models, usually in tabular form, are used in the computations. The overall result is a method of improved robustness and accuracy, with very encouraging performance on a number of challenging computations, such as the three-dimensional Saltzman, Noh [49] and Sedov [58] tests on Cartesian (i.e., non-polar) meshes.

This article also presents the full von Neumann analysis of stability for the predictor/multi-corrector algorithm applied to the linearized one-dimensional shock hydrodynamics equations, governing acoustic wave propagation in a compressible medium. Because the proposed algorithm is often used in combination with shock capturing artificial viscosities, stability bounds are derived not only in the case of a purely acoustic, undamped system of equations, but also in the case when diffusion is present. A simple time-step control condition is developed by analyzing the stability of the highest wave numbers in the discrete system of equations, and compared with results from the complete von Neumann analysis. Furthermore, by means of Taylor series expansions, it is shown that the formal accuracy of the method in the case of no artificial viscosity is second order in time and space. Finally, the von Neumann analysis is also used to provide effective estimates of the values of the stabilization parameters present in the formulation, and for this reason, constitutes a fundamental part in the design of the algorithm.

Although the proposed method can also be applied to triangular and tetrahedral finite element meshes (see [53], for an example in the context of earlier developments), the focus of the present paper is on computations with quadrilaterals and hexahedral elements. Focusing exclusively on these types of mesh topologies allows us to present extensive numerical comparisons with respect to earlier methods developed by some of the authors [53, 55, 56], and other research groups [2, 42]. The results of numerical computations show that hourglass patterns are virtually absent in two and three dimensions, a remarkable property of the proposed algorithm when compared to state-of-the-art methods in the field. Additional developments on triangular and tetrahedral meshes will be the object of future publications.

The rest of the exposition is organized as follows: Section 2 is devoted to presenting the equations of Lagrangian hydrodynamics and highlighting their structure as a nonlinear (mixed) system for acoustic wave propagation. A linearization of this system of equations is also derived. In Section 3, the variational multiscale analysis is applied first to the linearized version of the shock hydrodynamics system of equations (Section 3.1), and finally, to the full nonlinear case (Section 3.2). Although the nonlinear method was originally developed first, the authors find that the linearized problem offers an easier way of introducing the main concepts. Section 4 details a predictor/multi-corrector implementation of the variational multiscale approach. Invariance and global conservation properties of the method are discussed in Section 5. The von Neumann analysis is applied to a linearized version of this algorithm in Section 6, in order to evaluate its stability, accuracy and numerical diffusion/dispersion properties. Results from a number of challenging numerical computations are discussed in Section 7, and conclusions are summarized in Section 8.

## 2. General equations of Lagrangian shock hydrodynamics

The classical equations of Lagrangian shock hydrodynamics govern the rate of change in position, momentum and energy of a compressible body of fluid, as it deforms. Let  $\Omega_0$  and  $\Omega$  be open sets in  $\mathbb{R}^{n_d}$  (where  $n_d$  is the number of spatial dimensions). The *deformation*

$$\varphi : \Omega_0 \rightarrow \Omega = \varphi(\Omega_0) , \quad (1)$$

$$X \mapsto x = \varphi(X, t) , \quad \forall X \in \Omega_0, t \geq 0 , \quad (2)$$

maps the material coordinate  $X$ , representing the initial position of an infinitesimal material particle of the body, to  $x$ , the position of that particle in the current configuration (see Fig. 1).  $\Omega_0$  is the domain occupied by the body in its initial configuration, with boundary  $\partial\Omega_0$ .  $\varphi$  maps  $\Omega_0$  to  $\Omega$ , the domain occupied by the body in its current configuration, with boundary  $\partial\Omega$ .  $\varphi$  is usually a *smooth*, invertible map, so that the *deformation gradient*, and the *deformation Jacobian determinant* can be defined as

$$F = \nabla_x \varphi , \quad (3)$$

$$J = \det(F) , \quad (4)$$



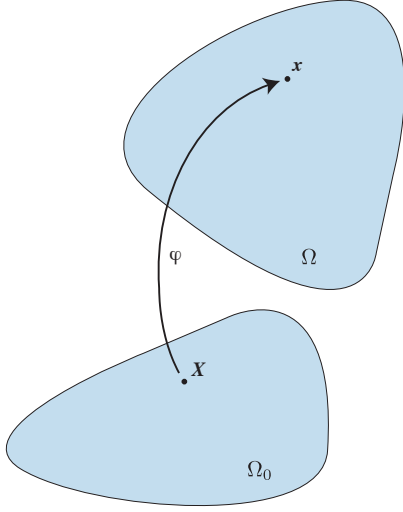


Figure 1: Sketch of the Lagrangian map  $\varphi$ .

where  $\nabla_x$  is the gradient in the original configuration. In the domain  $\Omega$ , the equations for the displacement update and conservation of mass, momentum, and energy read:

$$\dot{\mathbf{u}} = \mathbf{v} , \quad (5)$$

$$\rho J = \rho_0 , \quad (6)$$

$$\rho \dot{\mathbf{v}} = \rho \mathbf{b} + \nabla_x \cdot \boldsymbol{\sigma} , \quad (7)$$

$$\rho \dot{\epsilon} = \rho r + \nabla_x \mathbf{v} : \boldsymbol{\sigma} + \nabla_x \cdot \mathbf{q} . \quad (8)$$

Here,  $\nabla_x$  and  $\nabla_x \cdot$  are the current configuration gradient and divergence operators, and  $\dot{(\cdot)}$  indicates the material, or Lagrangian, time derivative.  $\mathbf{u} = \mathbf{x} - \mathbf{X}$  is the displacement vector,  $\rho_0$  is the reference (initial) density,  $\rho$  is the (current) density,  $\mathbf{v}$  is the velocity,  $\mathbf{b}$  is the body force (e.g., gravity),  $\boldsymbol{\sigma}$  is the symmetric Cauchy stress tensor,  $r$  is the energy source term, and  $\mathbf{q}$  is the heat flux. Using index notation,  $\boldsymbol{\sigma}^T : \nabla_x \mathbf{v} = \sigma_{ji} \partial_{x_i} v_j$ , and  $\nabla_x \mathbf{v} : \boldsymbol{\sigma} = \boldsymbol{\sigma} : \nabla_x \mathbf{v} = \boldsymbol{\sigma}^T : \nabla_x \mathbf{v}$ , since  $\boldsymbol{\sigma}$  is symmetric. We also denote by  $E = \epsilon + \mathbf{v} \cdot \mathbf{v} / 2$  the total energy, the sum of the internal energy  $\epsilon$  and the kinetic energy  $\mathbf{v} \cdot \mathbf{v} / 2$ . Obviously,  $E, \epsilon, \mathbf{b}, r$  are measured per unit mass.

Equations (5)–(8) are most commonly adopted in shock-hydrodynamics algorithms [6], and make use of the quasi-linear rather than the conservative form of the internal energy equation. The sum of the internal energy equation (8) and the kinetic energy equation (the product of (7) by the velocity vector  $\mathbf{v}$ ) yields the equation for the conservation of total energy. Although (8) is not in conservative form, it can still be used to develop a globally conservative variational formulation, as shown in Section 5. Assuming that the boundary  $\partial\Omega$  is partitioned as  $\partial\Omega = \partial\Omega^g \cup \partial\Omega^h$ ,  $\partial\Omega^g \cap \partial\Omega^h = \emptyset$ , displacement boundary conditions are enforced on the Dirichlet boundary  $\partial\Omega^g$ , that is,

$$\mathbf{u}|_{\partial\Omega^g} = \mathbf{u}_{bc}(\mathbf{x}, t) , \quad (9)$$

and traction boundary conditions are enforced on the Neumann

boundary  $\partial\Omega^h$ , by means of a physical traction vector  $\mathbf{t}$ , that is,

$$\boldsymbol{\sigma} \mathbf{n}|_{\partial\Omega^h} = \mathbf{t}(\mathbf{x}, t) . \quad (10)$$

Equations (5)–(8), and boundary conditions (9)–(10) completely define the evolution of the system, once constitutive relationships for the stress  $\boldsymbol{\sigma}$  and heat flux  $\mathbf{q}$  are specified, together with appropriate initial conditions.

### 2.1. Constitutive laws

For a fluid, the Cauchy stress  $\boldsymbol{\sigma}$  reduces to an isotropic tensor, dependent only on the thermodynamic pressure:

$$\boldsymbol{\sigma} = -p \mathbf{I}_{n_d \times n_d} , \quad (11)$$

An equation of state of the type

$$p = \hat{p}(\rho, \epsilon) , \quad (12)$$

is assumed. For example, equations of state of Mie-Grüneisen type are compatible with (12), namely

$$\hat{p}(\rho, \epsilon) = f_1(\rho) + f_2(\rho)\epsilon , \quad (13)$$

and apply to materials such as compressible ideal gases, co-volume gases, high explosives, etc. (See [47] for more details.) Ideal gases satisfy (13), with  $f_1 = 0$  and  $f_2 = (\gamma - 1)\rho$ , to yield

$$\hat{p}(\rho, \epsilon) = (\gamma - 1)\rho\epsilon . \quad (14)$$

### 2.2. Structure of the Lagrangian flow equations

It is important at this point to further elaborate on the structure of the Lagrangian shock hydrodynamic equations, because of its implications on the choice of stabilization techniques for the discrete variational formulation. To this end, recall that, in general, if an equation of state of the type  $\epsilon = \hat{\epsilon}(\rho, p)$  exists, then

$$d\epsilon = \left. \frac{\partial \epsilon}{\partial \rho} \right|_p d\rho + \left. \frac{\partial \epsilon}{\partial p} \right|_\rho dp . \quad (15)$$

Assuming, without loss of generality,  $\mathbf{q} = \mathbf{0}$  and  $r = 0$ , equation (15) can be used together with the mass conservation equation in differential form

$$\dot{\rho} + \rho \nabla_x \cdot \mathbf{v} = 0 , \quad (16)$$

to rearrange the energy equation (8):

$$\begin{aligned} 0 &= \rho \dot{\epsilon} + \rho \nabla_x \cdot \mathbf{v} \\ &= \rho \left. \frac{\partial \epsilon}{\partial \rho} \right|_p \dot{\rho} + \rho \left. \frac{\partial \epsilon}{\partial p} \right|_\rho \dot{p} + \rho \nabla_x \cdot \mathbf{v} \\ &= \rho \left. \frac{\partial \epsilon}{\partial p} \right|_\rho \left( \dot{p} + \frac{\frac{p}{\rho} - \rho \left. \frac{\partial \epsilon}{\partial \rho} \right|_p}{\left. \frac{\partial \epsilon}{\partial p} \right|_\rho} \nabla_x \cdot \mathbf{v} \right) , \end{aligned} \quad (17)$$

where, for a general compressible flow,  $\rho \partial_p \epsilon|_\rho \neq 0$ . It is possible to further manipulate the previous result using thermodynamic identities. First note that, by standard calculus derivations,

$$\left( \frac{\partial \epsilon}{\partial p} \right)_\rho^{-1} = \frac{\partial p}{\partial \epsilon} \Big|_\rho. \quad (18)$$

By the Gibbs identity (i.e., the combined first and second law of thermodynamics)  $d\epsilon - p/\rho^2 d\rho = \theta d\eta$  ( $\theta$  being the temperature and  $\eta$  the entropy per unit mass),

$$\frac{p}{\rho} = \rho \frac{\partial \epsilon}{\partial \rho} \Big|_\eta. \quad (19)$$

Combining (18) and (19) in the term multiplying the divergence in (17) yields

$$\begin{aligned} \frac{\frac{p}{\rho} - \rho \frac{\partial \epsilon}{\partial \rho} \Big|_p}{\frac{\partial \epsilon}{\partial p} \Big|_\rho} &= \rho \frac{\partial p}{\partial \epsilon} \Big|_\rho \left( \frac{\partial \epsilon}{\partial \rho} \Big|_\eta - \frac{\partial \epsilon}{\partial \rho} \Big|_p \right) \\ &= \rho \left( \frac{\partial p}{\partial \epsilon} \Big|_\rho \frac{\partial \epsilon}{\partial \rho} \Big|_\eta - \frac{\partial p}{\partial \epsilon} \Big|_\rho \frac{\partial \epsilon}{\partial \rho} \Big|_p \right) \end{aligned} \quad (20)$$

Equation (20) can be further simplified recalling that a thermodynamic relation of the type  $p = \hat{p}(\rho, \epsilon)$  yields

$$dp = \frac{\partial p}{\partial \rho} \Big|_\epsilon d\rho + \frac{\partial p}{\partial \epsilon} \Big|_\rho d\epsilon, \quad (21)$$

and, particularly,

$$0 = \frac{\partial p}{\partial \rho} \Big|_p = \frac{\partial p}{\partial \rho} \Big|_\epsilon + \frac{\partial p}{\partial \epsilon} \Big|_\rho \frac{\partial \epsilon}{\partial \rho} \Big|_p. \quad (22)$$

Substituting (22) into (20) yields

$$\begin{aligned} \frac{\frac{p}{\rho} - \rho \frac{\partial \epsilon}{\partial \rho} \Big|_p}{\frac{\partial \epsilon}{\partial p} \Big|_\rho} &= \rho \left( \frac{\partial p}{\partial \epsilon} \Big|_\rho \frac{\partial \epsilon}{\partial \rho} \Big|_\eta - \frac{\partial p}{\partial \epsilon} \Big|_\rho \frac{\partial \epsilon}{\partial \rho} \Big|_p \right) \\ &= \rho \left( \frac{\partial p}{\partial \epsilon} \Big|_\rho \frac{\partial \epsilon}{\partial \rho} \Big|_\eta + \frac{\partial p}{\partial \rho} \Big|_\epsilon \right) \\ &= \rho \frac{\partial p}{\partial \rho} \Big|_\eta \\ &= \rho c_s^2, \end{aligned} \quad (23)$$

where  $c_s$  is the isentropic speed of sound in the medium. Hence (17) reduces to

$$0 = \rho \frac{\partial \epsilon}{\partial p} \Big|_\rho \left( \dot{p} + \rho c_s^2 \nabla_x \cdot \mathbf{v} \right). \quad (24)$$

The term  $\rho \partial_p \epsilon|_\rho \neq 0$  can be simplified in (24), and the momentum and energy equations can be combined into the mixed, first-order system form of a nonlinear wave equation in  $\mathbf{v}$  and  $p$ :

$$0 = \rho \dot{\mathbf{v}} + \nabla_x p, \quad (25)$$

$$0 = \dot{p} + \rho c_s^2 \nabla_x \cdot \mathbf{v}. \quad (26)$$

**Remark1.** It is important to recognize the relation between  $\partial_p \epsilon|_\rho$  and the Grüneisen parameter [47], defined as

$$\Gamma = \frac{1}{\rho \frac{\partial \epsilon}{\partial p} \Big|_\rho} = \frac{1}{\rho} \frac{\partial p}{\partial \epsilon} \Big|_\rho. \quad (27)$$

The thermodynamic parameter  $\Gamma$  varies only mildly with the thermodynamic state of a fluid system, unless phase transitions occur [47]. In the case of an ideal gas satisfying a  $\gamma$ -law equation of state, it is easy to derive  $\Gamma = \gamma - 1 = \text{constant}$ .

### 2.3. Linearization of the equations

A linearized version of the shock hydrodynamic equations is developed next. This simplified setting is valuable in allowing a clearer understanding of the stabilization mechanisms to be discussed in what follows. For this purpose, the small-strain approximation is adopted, which implies small values of the displacement, velocity and acceleration, namely:

$$\mathbf{v} = \tilde{\mathbf{v}} \ll 1, \quad (28)$$

$$\mathbf{u} = \tilde{\mathbf{u}} \ll 1. \quad (29)$$

In particular, the small-strain approximation allows for the simplification  $\nabla_x \approx \nabla_x$  (the motion of the mesh is neglected when computing gradients). Assume also that the solution for the thermodynamic variables (density, pressure, internal energy) is given by a small perturbation of constant reference fields, namely:

$$\rho = \bar{\rho} + \tilde{\rho}, \quad \bar{\rho} = \text{const.}, \quad \tilde{\rho} \ll 1, \quad (30)$$

$$p = \bar{p} + \tilde{p}, \quad \bar{p} = \text{const.}, \quad \tilde{p} \ll 1, \quad (31)$$

$$c_s = \bar{c}_s + \tilde{c}_s, \quad \bar{c}_s = \text{const.}, \quad \tilde{c}_s \ll 1. \quad (32)$$

Hence, neglecting quadratic and higher-order terms, the linearized version of (25)–(26) is given by:

$$\bar{\rho} \dot{\tilde{\mathbf{v}}} + \nabla_x \tilde{p} = \mathbf{0}, \quad (33)$$

$$\dot{\tilde{p}} + \bar{\rho} \bar{c}_s^2 \nabla_x \cdot \tilde{\mathbf{v}} = 0, \quad (34)$$

which correspond to (25)–(26) with constant coefficients. Similar linearization procedures, applied to the displacement equations (5) and the differential form of the mass conservation equation (16), yield

$$\dot{\tilde{\mathbf{u}}} = \tilde{\mathbf{v}}, \quad (35)$$

$$\dot{\tilde{p}} + \bar{\rho} \nabla_x \cdot \tilde{\mathbf{v}} = 0. \quad (36)$$

Therefore, the linearized mass and displacement equations *decouple* from the linearized momentum and energy equations.

**Remark2.** In what follows, for the sake of simplicity, we will drop the “tildes” and “bars” from equations (33)–(34).

Taking the sum of the divergence of the momentum equation (33) and the time derivative of the energy equation (34) yields

$$0 = \ddot{p} - c_s^2 \Delta_x p, \quad (37)$$

where  $\Delta_x(\cdot) = \nabla_x \cdot (\nabla_x(\cdot))$  is the Laplace operator. Taking instead the sum of the time derivative of the momentum equation and the gradient of the energy equation,

$$\mathbf{0} = \dot{\mathbf{v}} - c_s^2 \Delta_x \mathbf{v} . \quad (38)$$

Therefore, the pressure and each of the velocity components abide a wave equation, with speed of propagation of disturbances given by  $c_s$ .

### 3. Variational multiscale analysis

Although the method presented here was originally developed in the nonlinear case, the linearized setting is probably the best starting point for introducing the main concepts. The variational multiscale analysis assumes that fine scales are small with respect to the coarse scales, in some integral sense. As a consequence, this approach applies naturally to smooth flow fields, and is less appropriate in the presence of solution discontinuities. This point is of particular importance in the nonlinear case, for which variational multiscale operators are based on a *locally* linearized approach.

#### 3.1. The linearized problem

The displacement and mass equations will not be discussed, since, as already pointed out in Section 2.3, they decouple from the momentum and energy equations.

##### 3.1.1. Variational equations

Neglecting body forces, heat fluxes, and heat sources, and assuming, without loss of generality, homogeneous Dirichlet boundary conditions for the velocity, the variational statement of (33)–(34), can be expressed as:

Find  $p \in S_\gamma$ ,  $\mathbf{v} \in S_\kappa$ , such that,  $\forall \psi \in \mathcal{V}_\gamma$ ,  $\forall \boldsymbol{\psi} \in \mathcal{V}_\kappa$ ,

$$0 = \int_{\Omega_0} \boldsymbol{\psi} \cdot (\rho \dot{\mathbf{v}}) \, d\Omega_0 - \int_{\Omega_0} \nabla_x \cdot \boldsymbol{\psi} \, p \, d\Omega_0 , \quad (39)$$

$$0 = \int_{\Omega_0} \psi \left( \dot{p} + \rho c_s^2 \nabla_x \cdot \mathbf{v} \right) \, d\Omega_0 , \quad (40)$$

where  $\rho$  and  $c_s$  are assumed constant. In particular,  $S_\kappa$  denotes the *trial* space of admissible values for the kinematic variables (velocities, in this case, with boundary conditions *strongly* embedded in the function space definition), and  $S_\gamma$  the trial space of admissible thermodynamic states (pressures). In addition, *test* spaces have been introduced:  $\mathcal{V}_\kappa$  is the space of variations for the kinematic variables (compatible with the boundary conditions), and  $\mathcal{V}_\gamma$  is the space of variations for the thermodynamic variables.

##### 3.1.2. Scale decomposition

The variational multiscale analysis of (39)–(40) is accomplished by decomposing the exact solution state vector  $\mathbf{Y} = [\mathbf{v}^T, p]^T \in \mathcal{S}$  as  $\mathbf{Y} = \mathbf{Y}^h + \mathbf{Y}'$ .  $\mathbf{Y}^h \in \mathcal{S}^h$  is the *mesh-* or *coarse-* scale solution, belonging to the discrete approximation space  $\mathcal{S}^h$ .  $\mathbf{Y}' \in \mathcal{S}'$  is the *subgrid-* or *fine-* scale solution, the component of the solution not represented on the computational mesh.

Hence,  $\mathcal{S} = \mathcal{S}^h \oplus \mathcal{S}'$  (here  $\oplus$  does not denote an orthogonal sum decomposition), and analogously,  $\mathcal{V} = \mathcal{V}^h \oplus \mathcal{V}'$ . In view of the adopted boundary conditions, the following choice of function spaces can be made

$$\mathcal{S}_\kappa^h = \mathcal{V}_\kappa^h = \left\{ \boldsymbol{\psi}^h \in (C^0(\Omega_0))^{n_d} : \boldsymbol{\psi}^h|_{\Omega_{0;e}} \in (\mathcal{P}_1(\Omega_{0;e}))^{n_d}, \right. \\ \left. \boldsymbol{\psi}^h = \mathbf{0} \text{ on } \partial\Omega_0^g = \partial\Omega_0 \right\} , \quad (41)$$

$$\mathcal{S}_\gamma^h = \mathcal{V}_\gamma^h = \left\{ \psi^h \in C^0(\Omega_0) : \psi^h|_{\Omega_{0;e}} \in \mathcal{P}_1(\Omega_{0;e}), \right\} , \quad (42)$$

where  $\mathcal{P}_1(\Omega_{0;e})$  is the space of piece-wise linear polynomials over the element  $e$ ,  $n_d$  is the number of space dimensions, and homogeneous Dirichlet boundary conditions have been incorporated (strongly) into the definition of the function spaces. We obtain

$$\mathbf{v} = \mathbf{v}^h + \mathbf{v}' , \quad (43)$$

$$p = p^h + p' , \quad (44)$$

so that (39)–(40), when tested on  $\mathcal{V}_\kappa^h$  and  $\mathcal{V}_\gamma^h$ , respectively, reduce to

$$\int_{\Omega_0} \boldsymbol{\psi}^h \cdot \rho (\dot{\mathbf{v}}^h + \dot{\mathbf{v}}') \, d\Omega_0 - \int_{\Omega_0} (\nabla_x \cdot \boldsymbol{\psi}^h) (p^h + p') \, d\Omega_0 = 0 , \quad (45)$$

and

$$\int_{\Omega_0} \psi^h (\dot{p}^h + \dot{p}' + \rho c_s^2 (\nabla_x \cdot (\mathbf{v}^h + \mathbf{v}')) \, d\Omega_0 = 0 . \quad (46)$$

Using integration by parts, equation (46) can be rearranged as

$$\int_{\Omega_0} \psi^h (\dot{p}^h + \dot{p}' + \rho c_s^2 (\nabla_x \cdot \mathbf{v}^h)) \, d\Omega_0 \\ - \int_{\Omega_0} \nabla_x \psi^h \cdot (\rho c_s^2 \mathbf{v}') \, d\Omega_0 \\ + \sum_{e=1}^{n_{el}} \int_{\partial\Omega_{0;e}} \psi^h (\rho c_s^2 \mathbf{v}') \cdot \mathbf{n}_e \, d(\partial\Omega_{0;e}) = 0 , \quad (47)$$

where  $\mathbf{n}_e$  indicates the outward pointing normal with respect to the element  $e$ , and  $n_{el}$  the total number of elements in the mesh. Recalling now that  $\psi^h$  is continuous across the interface between elements, and that  $\rho$  and  $c_s$  are constant in the linearized case, one can express the last term in (47) using the following identity, often employed in discontinuous Galerkin formulations:

$$\sum_{e=1}^{n_{el}} \int_{\partial\Omega_{0;e}} \psi^h (\rho c_s^2 \mathbf{v}') \cdot \mathbf{n}_e \, d(\partial\Omega_{0;e}) \\ = \int_{\partial\Omega_0} \psi^h (\rho c_s^2 \mathbf{v}') \cdot \mathbf{n} \, d(\partial\Omega_0) + \int_{\tilde{\mathcal{E}}_0} \psi^h \rho c_s^2 \llbracket \mathbf{v}' \rrbracket \, d\tilde{\mathcal{E}}_0 . \quad (48)$$

The term  $\llbracket \mathbf{w} \rrbracket = \mathbf{w}^- \cdot \mathbf{n}^- + \mathbf{w}^+ \cdot \mathbf{n}^+$  is often referred to as the jump operator, with the superscripts  $\pm$  indicating the values of  $\mathbf{w}$  and  $\mathbf{n}$  on either side of an interface between two elements (i.e., an

edge or face in the interior of the domain).  $\tilde{\mathcal{E}}_0$  denotes the set of interior element interfaces, in the initial configuration of the mesh. Note that *no approximation* has been made so far (the fields  $\mathbf{v}^h, \mathbf{v}', p^h, p'$  are assumed to be known *exactly*). In order to obtain a viable stabilization strategy, a few conditions on the terms in the coarse-scale equations are required. Some of the conditions have a straightforward justification, while others are dictated by simplicity and ease of implementation.

#### Coarse-scale conditions

- (i) Time derivatives of the fine-scales are neglected. This *quasi-static* approximation is equivalent to assuming that the fine scales adjust instantaneously to complement the coarse scales. Some authors [16] have been arguing in favor of tracking in time the subgrid-scale component of the solution. However, this would involve the additional computational cost of storing and integrating in time the fine-scale component of the state variables.
- (ii) For smooth flows, one can expect that the spaces  $\mathcal{S}_\gamma, \mathcal{S}_\kappa$  are composed of smooth functions (in particular, *continuous* functions). Recalling that, by definition,  $\mathcal{S}'_\gamma, \mathcal{S}'_\kappa$  are discrete spaces of continuous functions, we can conclude that, for smooth flows, also  $\mathcal{S}'_\gamma, \mathcal{S}'_\kappa$  are constituted of continuous functions. The condition

$$\int_{\tilde{\mathcal{E}}_0} \psi^h \llbracket \mathbf{v}' \rrbracket d\tilde{\mathcal{E}}_0 = 0, \quad (49)$$

representing a weak enforcement of the continuity of  $\mathbf{v}'$  across element interfaces, is automatically satisfied in this case.

- (iii) Analogously, the condition

$$\int_{\partial\Omega_0} \psi^h \mathbf{v}' \cdot \mathbf{n} d(\partial\Omega_0) = 0 \quad (50)$$

is weakly enforcing a vanishing fine-scale solution at the boundary of the domain  $\Omega_0$ , where boundary conditions apply. This is again a fairly standard hypothesis in variational multiscale formulations [26, 27, 33].

With the previous assumptions, (45) and (48) reduce to:

$$\int_{\Omega_0} \psi^h \cdot (\rho \dot{\mathbf{v}}^h) d\Omega_0 - \int_{\Omega_0} (\nabla_x \cdot \psi^h)(p^h + p') d\Omega_0 = 0, \quad (51)$$

$$\begin{aligned} \int_{\Omega_0} \psi^h (\dot{p}^h + \rho c_s^2 (\nabla_x \cdot \mathbf{v}^h)) d\Omega_0 \\ - \int_{\Omega_0} \nabla_x \psi^h \cdot (\rho c_s^2 \mathbf{v}') d\Omega_0 = 0. \end{aligned} \quad (52)$$

The variational multiscale approach now requires to test the momentum and energy equations on the fine-scale spaces, that is,

$$\int_{\Omega_0} \psi' \cdot (\rho \dot{\mathbf{v}}') d\Omega_0 - \int_{\Omega_0} (\nabla_x \cdot \psi') p' d\Omega_0 = -\langle \text{Res}_v^h, \psi' \rangle, \quad (53)$$

$$\int_{\Omega_0} \psi' (\dot{p}' + \psi' \rho c_s^2 (\nabla_x \cdot \mathbf{v}')) d\Omega_0 = -\langle \text{Res}_\epsilon^h, \psi' \rangle, \quad (54)$$

where  $\text{Res}_v^h$  and  $\text{Res}_p^h$  are operators belonging to the dual spaces  $(\mathcal{S}'_\kappa)^*$  and  $(\mathcal{S}'_\gamma)^*$ , the spaces of continuous linear functionals over  $\mathcal{S}'_\kappa$  and  $\mathcal{S}'_\gamma$ , respectively. Recalling that, by definition, the test functions vanish where pure Dirichlet boundary conditions are applied, and that the discrete test and trial spaces are constituted of continuous functions (so that inter-element jumps vanish) the residual operators have the expressions:

$$\begin{aligned} \langle \text{Res}_v^h, \mathbf{w} \rangle &= \int_{\Omega_0} \mathbf{w} \cdot (\rho^h \dot{\mathbf{v}}^h) d\Omega_0 - \int_{\Omega_0} (\nabla_x \cdot \mathbf{w}) p^h d\Omega_0 \\ &= \int_{\Omega_0} \mathbf{w} \cdot (\rho^h \dot{\mathbf{v}}^h + \nabla_x p^h) d\Omega_0, \end{aligned} \quad (55)$$

$$\langle \text{Res}_\epsilon^h, w \rangle = \int_{\Omega_0} w (\dot{p}^h + \rho c_s^2 (\nabla_x \cdot \mathbf{v}^h)) d\Omega_0. \quad (56)$$

Assuming (as usually reasonable) that  $\mathcal{S}'_\kappa \subset (L^2(\Omega_0))^{n_d}$  and  $\mathcal{S}'_\gamma \subset L^2(\Omega_0)$  (i.e.,  $\mathbf{w}$  and  $w$  are Lebesgue square-integrable functions), the Riesz Representation Theorem [7, 68] allows to identify

$$\text{Res}_v^h = \rho \dot{\mathbf{v}}^h + \nabla_x p^h, \quad (57)$$

$$\text{Res}_p^h = \dot{p}^h + \rho c_s^2 (\nabla_x \cdot \mathbf{v}^h), \quad (58)$$

where  $\text{Res}_v^h$  and  $\text{Res}_p^h$  are now considered as elements of  $(L^2(\Omega_0))^{n_d}$  and  $L^2(\Omega_0)$ , respectively. Ideally, one would like to solve exactly the fine-scale equations, but, in practice, this is rarely possible and, for the purpose of stabilization, *unnecessary*. In fact, simple approximated *ansatz* based on the scaling of the residual are sufficient to provide the needed stabilization mechanisms.

#### Fine-scale conditions

- (iv) Probably the simplest option is to assume that

$$\mathbf{v}' = -\tau \frac{1}{\rho} \text{Res}_v^h, \quad (59)$$

$$p' = -\tau \text{Res}_p^h, \quad (60)$$

where  $\tau$  is an appropriate parameter with the dimension of time. This amounts to postulate that the dynamics of the fine scales decouples, as the fine-scale velocity  $\mathbf{v}'$  is assumed to depend only on the momentum equation residual  $\text{Res}_v^h$ , and the fine-scale pressure  $p'$  only on the pressure equation residual  $\text{Res}_p^h$ . The factor  $1/\rho$  in front of  $\text{Res}_v^h$  is needed for a correct dimensional scaling of  $\mathbf{v}'$ . A unique definition of  $\tau$  is used for both the pressure and velocity equations, governing the propagation of acoustic waves. Because the coarse-scale momentum and pressure equations are tightly coupled, using different definitions of  $\tau$  in each of them may have potentially negative effects on the dissipation and dispersion error characteristics of the stabilized algorithm.

- (v) Using criteria similar to [52, 53, 56], the stabilization parameter  $\tau$  can be defined as

$$\tau = c_\tau \frac{\Delta t}{2}. \quad (61)$$

In practice,  $\tau$  represents the average effect of the Green's function associated with the fine-scale equations [8, 26, 27, 33]. For the purpose of constructing stabilization mechanisms, it is not necessary to have a very accurate approximation of the Green's function, and a correct scaling is sufficient. Consequently, there is some freedom in defining the constant  $c_\tau$ . An effective choice of  $c_\tau$  depends on the particular spatial and temporal discretization, and a complete discussion on how to estimate appropriate values using the von Neumann analysis of dissipation and dispersion errors is presented in Section 6.

**Remark3.** Similar results would have been obtained if the standard SUPG methodology for systems of equations were used in place of the multiscale analysis (see [15, 52, 53]). In fact, it is possible to rewrite equations (39)–(40) as

$$A_0 \dot{Y} + A_i Y_{,X_i} = \mathbf{0}, \quad (62)$$

where  $Y = [v^T, p]^T$ , and

$$A_0 = \begin{bmatrix} \rho \mathbf{I}_{3 \times 3} & \mathbf{0}_{3 \times 1} \\ \mathbf{0}_{1 \times 3} & 1 \end{bmatrix}, \quad (63)$$

$$A_i = \begin{bmatrix} 0 & 0 & 0 & \delta_{1i} \\ 0 & 0 & 0 & \delta_{2i} \\ 0 & 0 & 0 & \delta_{3i} \\ \rho c_s^2 \delta_{1i} & \rho c_s^2 \delta_{2i} & \rho c_s^2 \delta_{3i} & 0 \end{bmatrix}, \quad (64)$$

with  $\delta_{ij}$  the Kronecker tensor ( $\delta_{ij} = 1$  if  $i = j$ ,  $\delta_{ij} = 0$  otherwise). The stabilization proposed in [15, 52, 53] follows a methodology similar to [22, 23, 28, 29, 31, 32] and yields:

$$Y' = -\tau(A_0 \dot{Y} + A_i Y_{,X_i}) = -\tau(\dot{Y} + A_0^{-1} A_i Y_{,X_i}), \quad (65)$$

where  $\tau = \tau A_0^{-1}$ , so that

$$\dot{Y} + A_0^{-1} A_i Y_{,X_i} = \begin{bmatrix} \frac{1}{\rho} \text{Res}_v^h \\ \text{Res}_p^h \end{bmatrix}. \quad (66)$$

The fundamental reason why these derivations match the previous multiscale analysis is due to the fact that  $\tau$  has been chosen as a diagonal matrix. The precise definition of  $\tau$  is somewhat arbitrary, and many different approaches to its design have been proposed [15, 22, 23, 28, 29, 31, 32, 34, 38, 52, 53, 63, 64]. Had not  $\tau$  been diagonal, a fully coupled residual ansatz for  $Y'$  would have been obtained. This aspect is a consequence of the connection between  $\tau$  and the Green's function for the fine-scale equations [26, 27, 33]. In the discussion to follow on the nonlinear case, it will be easy to appreciate that the variational multiscale approach and the more classical instantiations of the SUPG method for compressible flows may have some substantial differences in the overall structure of the stabilizing terms.

### 3.1.3. Stability properties

In [15], a numerical stability analysis is presented for a SUPG-stabilized method applied to the system form of a general linear hyperbolic wave equation. Although the present work and the work in [15] have been developed over the years

in complete independence and aiming at different applications, there are similarities in the form of the stabilizing operators, at least in the linear case. Most importantly, the detailed stability analysis – for the time-continuous case in multiple dimensions – included in [15] directly applies to the linearized acoustic system under investigation in the present article. This result and the classical stability analysis of SUPG methods for compressible flows [28–30, 35, 36, 62] show that the proposed variational multiscale approach provides stability to formulations with equal-order interpolation for pressure and velocity in the linearized case. Consequently, the nonlinear method to be described next lays on solid theoretical foundations. It is worthwhile at this point to present the overall stabilized variational form of the linearized acoustic problem:

$$0 = \int_{\Omega_0} \psi^h \cdot \rho \dot{v}^h d\Omega_0 - \int_{\Omega_0} (\nabla_x \cdot \psi^h) p^h d\Omega_0 + \int_{\Omega_0} (\nabla_x \cdot \psi^h) \tau (\dot{p}^h + \rho c_s^2 (\nabla_x \cdot v^h)) d\Omega_0, \quad (67)$$

$$0 = \int_{\Omega_0} \psi^h (\dot{p}^h + \rho c_s^2 (\nabla_x \cdot v^h)) d\Omega_0 + \int_{\Omega_0} \nabla_x \psi^h \cdot c_s^2 \tau (\rho \dot{v}^h + \nabla_x p^h) d\Omega_0. \quad (68)$$

It is clear that the terms

$$\int_{\Omega_0} \tau c_s^2 (\nabla_x \cdot \psi^h) (\nabla_x \cdot v^h) d\Omega_0, \quad (69)$$

$$\int_{\Omega_0} \tau c_s^2 \nabla_x \psi^h \cdot \nabla_x p^h d\Omega_0 \quad (70)$$

have a stabilizing effect on equations (67)–(68), since they are the weak forms of a divergence-type ( $H^{div}$ ) incomplete Laplacian of the velocity and a full Laplacian of the pressure, respectively. The stability analysis in [15] confirms such conjecture.

It is interesting to observe the terms (69)–(70) scale with  $\tau c_s^2$ , which represents an acoustic-inspired kinematic viscosity. There are therefore some similarities between the stabilizing terms in (67)–(68) and the so-called linear artificial viscosity [6, 49, 66], used to control acoustic oscillations past shock fronts. There is however *one major difference*, since the linear artificial viscosity approach is not variationally consistent, and degrades the order of accuracy of the method to first order. In the case of the stabilized equations (67)–(68), the terms (69)–(70) do not degrade the original order of accuracy of the method to first order, since they are complemented by time derivative terms to form complete, variationally consistent residuals (see also Section 6 for an analysis of formal order of accuracy).

### 3.2. The nonlinear problem

The nonlinear case is attacked next. In particular, this section describes in a more general sense how the variational multiscale methodology yields stabilization operators. For a practical numerical implementation, the reader should refer to Section 4.

### 3.2.1. Variational equations

As in the linear case, the first step in the development of a variational form for (5)–(8) is to define the *trial* spaces for the kinematic and thermodynamic variables, which characterize the *state* of the system. Let  $\mathcal{S}_\kappa$  denote the space of admissible values for the kinematic variables (displacements, velocities, accelerations), and  $\mathcal{S}_\gamma$  the space of admissible thermodynamic states (densities, pressures, internal energies). In addition,  $\mathcal{V}_\kappa$  is the (test) space of variations (compatible with the boundary condition (9)) for the kinematic variables, and  $\mathcal{V}_\gamma$  is the (test) space of variations for the thermodynamic variables. The complete variational problem reads:

Find  $\rho, p, \epsilon \in \mathcal{S}_\gamma$ ,  $\mathbf{u}, \mathbf{v} \in \mathcal{S}_\kappa$ , such that,  $\forall \psi \in \mathcal{V}_\gamma$ ,  $\forall \boldsymbol{\psi} \in \mathcal{V}_\kappa$ ,

$$0 = \int_{\Omega_0} \boldsymbol{\psi} \cdot (\dot{\mathbf{u}} - \mathbf{v}) \, d\Omega_0, \quad (71)$$

$$0 = \int_{\Omega_0} \psi (\rho_0 - \rho J) \, d\Omega_0, \quad (72)$$

$$0 = \int_{\Omega_0} \boldsymbol{\psi} \cdot (\rho_0 \dot{\mathbf{v}}) \, d\Omega_0 + \int_{\Omega} \nabla_x^s \boldsymbol{\psi} : \boldsymbol{\sigma} \, d\Omega - \int_{\Gamma^h} \boldsymbol{\psi} \cdot \mathbf{t} \, d\Gamma - \int_{\Omega} \boldsymbol{\psi} \cdot (\rho \mathbf{b}) \, d\Omega, \quad (73)$$

$$0 = \int_{\Omega_0} \psi (\rho_0 \dot{\epsilon}) \, d\Omega_0 - \int_{\Omega} \psi (\nabla_x^s \mathbf{v} : \boldsymbol{\sigma} + \rho r) \, d\Omega + \int_{\Omega} \nabla_x \psi \cdot \mathbf{q} \, d\Omega, \quad (74)$$

where  $\nabla_x^s = 1/2(\nabla_x^T + \nabla_x)$  is the symmetric part of the gradient operator, and  $\boldsymbol{\sigma} = -p\mathbf{I}$ , so that  $\nabla_x^s \boldsymbol{\psi} : \boldsymbol{\sigma} = -(\nabla_x \cdot \boldsymbol{\psi})p$ , and  $\nabla_x^s \mathbf{v} : \boldsymbol{\sigma} = -(\nabla_x \cdot \mathbf{v})p$ . In (73)–(74), we have used the identity  $\rho_0 \, d\Omega_0 = \rho \, d\Omega$ , which states that the mass of an infinitesimal particle  $dm = \rho_0 \, d\Omega_0$  does not change under the Lagrangian deformation map. In the current formulation, the traction (i.e., *natural*) boundary conditions (10) are imposed in (73) through the weak form, while the space  $\mathcal{S}_\kappa$  incorporates the set of *essential* boundary conditions (9). Consequently, boundary conditions of kinematic (Dirichlet) type are imposed *strongly*. The specific types of function spaces adopted in the formulation will be given subsequently.

### 3.2.2. Scale decomposition and stabilization

It is important to observe that the following analysis applies in the case of smooth flows (smooth solutions), for which the fine scales are assumed small with respect to the coarse scales. In particular, in the case of nonlinear systems, the variational multiscale framework leverages a *local* linearization of the equations. As in the linear case, the first step consists in developing a multiscale description of the solution. For the sake of simplicity, and without loss of generality, the heat source/sink  $r$ , the body force  $\mathbf{b}$ , and the thermal heat flux  $\mathbf{q}$  are assumed absent. The exact solution for the state  $\mathbf{Y} = [\mathbf{u}^T, \mathbf{v}^T, \rho, \epsilon, p]^T \in \mathcal{S}$  of the system is decomposed as  $\mathbf{Y} = \mathbf{Y}^h + \mathbf{Y}'$ , where  $\mathbf{Y}^h \in \mathcal{S}^h$  is the *mesh-* or *coarse-scale* solution, and  $\mathbf{Y}' \in \mathcal{S}'$  is the *subgrid-*

or *fine-scale* solution, with  $\mathcal{S} = \mathcal{S}^h \oplus \mathcal{S}'$ . In the proposed spatial approximation, *all* variables (both kinematic and thermodynamic, including pressure, density and internal energy) are approximated by piece-wise linear, continuous functions (node-centered degrees-of-freedom). Consequently, the test-spaces for the equations consist of piece-wise linear, continuous functions. More precisely:

$$\mathcal{S}_\kappa^h = \{ \boldsymbol{\psi}^h \in (C^0(\Omega))^{n_d} : \boldsymbol{\psi}^h|_{\Omega_e} \in (\mathcal{P}_1(\Omega_e))^{n_d}, \boldsymbol{\psi}^h = \mathbf{g}_{bc}(t) \text{ on } \partial\Omega^g \}, \quad (75)$$

$$\mathcal{V}_\kappa^h = \{ \boldsymbol{\psi}^h \in (C^0(\Omega))^{n_d} : \boldsymbol{\psi}^h|_{\Omega_e} \in (\mathcal{P}_1(\Omega_e))^{n_d}, \boldsymbol{\psi}^h = \mathbf{0} \text{ on } \partial\Omega^g \}, \quad (76)$$

and

$$\mathcal{S}_\gamma^h = \{ \psi^h \in C^0(\Omega) : \psi^h|_{\Omega_e} \in \mathcal{P}_1(\Omega_e) \}, \quad (77)$$

$$\mathcal{V}_\gamma^h = \mathcal{S}_\gamma^h, \quad (78)$$

where  $\mathbf{g}_{bc}(t)$  indicates the generalized essential (Dirichlet) boundary conditions, possibly dependent on time. For example, if  $\mathcal{S}_\kappa^h$  is used to approximate displacements, then  $\mathbf{g}_{bc} = \mathbf{u}_{bc}$ . If instead  $\mathcal{S}_\kappa^h$  is used to approximate velocities, then  $\mathbf{g}_{bc}$  indicates a velocity at the boundary compatible with  $\mathbf{u}_{bc}$ . Hence:

$$\mathbf{u} = \mathbf{u}^h + \mathbf{u}', \quad (79)$$

$$\mathbf{v} = \mathbf{v}^h + \mathbf{v}', \quad (80)$$

$$\rho_0 = \rho_0^h + \rho_0', \quad (81)$$

$$\rho = \rho^h + \rho', \quad (82)$$

$$\epsilon = \epsilon^h + \epsilon', \quad (83)$$

$$p = p^h + p'. \quad (84)$$

In the Lagrangian setting, the displacement and mass conservation equations (5)–(6) are associated with a standing entropy wave (with respect to the Lagrangian material coordinates) governing the motion of contact discontinuities. In this context, it is also important to observe that numerical schemes in Lagrangian coordinates, by construction, are capable of precisely capturing and tracking contact discontinuities without adding any numerical dissipation. Consequently, the incorporation of the equations (71)–(72) is not critical in the analysis, which can be restricted to equations (73) and (74). This simplified approach has the main advantage of producing a “minimalist stabilization”, of easier numerical implementation. Namely, when tested on the discrete spaces  $\mathcal{V}_\kappa^h$  and  $\mathcal{V}_\gamma^h$ , (73) and (74) reduce to

$$0 = \int_{\Omega_0} \boldsymbol{\psi}^h \cdot (\rho_0^h + \rho_0')(\dot{\mathbf{v}}^h + \dot{\mathbf{v}}') \, d\Omega_0 - \int_{\Omega} (\nabla_x \cdot \boldsymbol{\psi}^h)(p^h + p') \, d\Omega, \quad (85)$$

$$0 = \int_{\Omega_0} \psi^h (\rho_0^h + \rho_0')(\dot{\epsilon}^h + \dot{\epsilon}') \, d\Omega_0 + \int_{\Omega} \psi^h (\nabla_x \cdot (\mathbf{v}^h + \mathbf{v}'))(p^h + p') \, d\Omega, \quad (86)$$

where, for the sake of simplicity and without loss of generality, homogenous Dirichlet boundary conditions are imposed for the velocity. Using integration by parts, the energy equation (86) can be rearranged as follows:

$$\begin{aligned} & \int_{\Omega_0} \psi^h(\rho_0^h + \rho_0')(\dot{\epsilon}^h + \dot{\epsilon}') d\Omega_0 + \int_{\Omega} \psi^h \nabla_x \cdot \mathbf{v}^h (p^h + p') d\Omega \\ & - \int_{\Omega} \nabla_x \psi^h \cdot ((p^h + p')\mathbf{v}') d\Omega - \int_{\Omega} \psi^h (\nabla_x(p^h + p')) \cdot \mathbf{v}' d\Omega \\ & + \sum_{e=1}^{n_{el}} \int_{\partial\Omega_e} \psi^h (p^h + p') \mathbf{v}' \cdot \mathbf{n}_e d(\partial\Omega) = 0. \end{aligned} \quad (87)$$

Recalling that  $\psi^h$  is continuous across element interfaces, the last term in (87) can be expressed as

$$\begin{aligned} \sum_{e=1}^{n_{el}} \int_{\partial\Omega_e} \psi^h (p^h + p') \mathbf{v}' \cdot \mathbf{n}_e d\Omega &= \int_{\partial\Omega} \psi^h p \mathbf{v}' \cdot \mathbf{n} d(\partial\Omega) \\ &+ \int_{\tilde{\mathcal{E}}} \psi^h \llbracket p \mathbf{v}' \rrbracket d\tilde{\mathcal{E}}, \end{aligned} \quad (88)$$

where, analogous to the linear case,  $\llbracket \mathbf{w} \rrbracket = \mathbf{w}^- \cdot \mathbf{n}^- + \mathbf{w}^+ \cdot \mathbf{n}^+$ , and  $\tilde{\mathcal{E}}$  is the set of interior element interfaces (this time in the current configuration mesh). Then (87) becomes

$$\begin{aligned} & \int_{\Omega_0} \psi^h(\rho_0^h + \rho_0')(\dot{\epsilon}^h + \dot{\epsilon}') d\Omega_0 + \int_{\Omega} \psi^h \nabla_x \cdot \mathbf{v}^h (p^h + p') d\Omega \\ & - \int_{\Omega} \nabla_x \psi^h \cdot ((p^h + p')\mathbf{v}') d\Omega - \int_{\Omega} \psi^h (\nabla_x(p^h + p')) \cdot \mathbf{v}' d\Omega \\ & + \int_{\partial\Omega} \psi^h p^h \mathbf{v}' \cdot \mathbf{n} d(\partial\Omega) + \int_{\tilde{\mathcal{E}}} \psi^h \llbracket p^h \mathbf{v}' \rrbracket d\tilde{\mathcal{E}} = 0. \end{aligned} \quad (89)$$

From now on, we will focus on the variational forms (85) and (89). Analogous projections of (85) and (89) onto the fine scale test spaces  $\mathcal{V}'_\kappa$  and  $\mathcal{V}'_\gamma$  can be considered, to generate the fine-scale problems. *No approximation* has been made so far, and the initial geometry of the computational grid, as well as the displacement field are assumed to be known *exactly*. In order to obtain a treatable problem, a number of conditions has to be enforced on some of the terms in the coarse-scale equations. As in the linear case, some of these conditions are straightforward, others are dictated by simplicity and ease of implementation.

#### Coarse-scale conditions

- (i) Fine-scale terms are considered *small* with respect to coarse-scale terms. Therefore, if necessary, products of fine-scale terms can be neglected, being higher-order corrections. This is, essentially, a statement of local linearization of the variational problem under consideration.
- (ii) Fine-scale components of the displacements  $\mathbf{u}'$  (i.e., fine-scale node positions and mesh geometry) are considered negligible, with the purpose of a simpler implementation. Although not pursued here, there is a possibility to quantify these fine-scale contributions.
- (iii)  $\rho_0'$  is considered negligible, since  $\rho_0$  is a *datum* of the problem.

- (iv) As in the linear case, time derivatives of the fine-scales are neglected, in favor of a quasi-static approximation.
- (v) In order to preserve global conservation properties, we enforce as a design condition that the last three integral terms in (89) vanish. Let us review each of these conditions:

$$\int_{\Omega} \psi^h (\nabla_x(p^h + p')) \cdot \mathbf{v}' d\Omega = 0 \quad (90)$$

enforces that the projection onto the test function space of the inner product between the pressure gradient and fine-scale velocity vanishes. An equivalent interpretation is that, in a weak sense, the fine-scale component of the velocity does not produce any internal work. This condition can also be understood as the constraint on  $\mathbf{v}'$  to be a zero-energy, hourglass mode [4, 6]. The condition

$$\int_{\partial\Omega} \psi^h p^h \mathbf{v}' \cdot \mathbf{n} d(\partial\Omega) = 0 \quad (91)$$

weakly enforces that the fine-scale velocity does not produce any work at the boundary  $\partial\Omega$  of the domain. This condition is equivalent to imposing that the fine-scale velocity vanishes at the boundary  $\partial\Omega$ , and, as already mentioned in Section 3.1.2, is a standard (often implicit) hypothesis in variational multiscale formulations [26, 27, 33]. Finally, the condition

$$\int_{\tilde{\mathcal{E}}} \psi^h \llbracket p^h \mathbf{v}' \rrbracket d\tilde{\mathcal{E}} = 0 \quad (92)$$

weakly enforces that the surface work  $p^h \mathbf{v}' \cdot \mathbf{n}$ , produced by the interaction of the fine-scale velocity and coarse-scale pressure, is continuous across element interfaces. In the case of a smooth  $\mathbf{v}$ , recalling that  $p^h$  and  $\mathbf{v}^h$  are continuous, then  $\mathbf{v}' = \mathbf{v} - \mathbf{v}^h$  is also continuous, and condition (92) is automatically satisfied. Condition (92) is often implicitly invoked in SUPG stabilized formulations for compressible flows [22, 23, 26–29, 31–33].

Applying the previous conditions, and pushing forward to the current configuration the integrals in (85) and (87) involving time derivatives, it is easy to derive:

$$\int_{\Omega} \psi^h \cdot (\rho^h \dot{\mathbf{v}}^h) d\Omega - \int_{\Omega} \nabla_x \cdot \psi^h (p^h + p') d\Omega = 0, \quad (93)$$

$$\begin{aligned} & \int_{\Omega} \psi^h (\rho^h \dot{\epsilon}^h + p^h \nabla_x \cdot \mathbf{v}^h) d\Omega + \int_{\Omega} \psi^h p' \nabla_x \cdot \mathbf{v}^h d\Omega \\ & - \int_{\Omega} \nabla_x \psi^h \cdot (p^h \mathbf{v}') d\Omega = 0. \end{aligned} \quad (94)$$

In particular, from the derivation in Section 2.2 (see eq. 24),

$$\rho^h \dot{\epsilon}^h + p^h \nabla_x \cdot \mathbf{v}^h = \rho^h \partial_\epsilon p^h \Big|_\rho^h (\dot{p}^h + \rho^h (c_s^h)^2 (\nabla_x \cdot \mathbf{v}^h)). \quad (95)$$

Therefore, the variational multiscale stabilization of the nonlinear case retains part of the structure of the linearized case. This observation is important in designing appropriate approximations to  $p'$  and  $\mathbf{v}'$ .

**Remark4.** The term

$$\int_{\Omega} \psi^h p' \nabla_x \cdot \mathbf{v}^h d\Omega \quad (96)$$

is not present in the linearized case, and is of fundamental importance in preserving global conservation of total energy in the nonlinear case. It is also important to notice that this term would not appear if a standard SUPG approach were applied. Details on the global conservation properties of the proposed stabilization approach are presented in Section 5.

The variational multiscale approach now requires to test the momentum and energy equations on the fine-scale spaces  $\mathcal{V}'_{\kappa}$  and  $\mathcal{V}'_{\gamma}$ , that is,

$$\begin{aligned} & \int_{\Omega_0} \psi' \cdot (\rho_0^h + \rho'_0) \dot{\mathbf{v}}' d\Omega_0 \\ & + \int_{\Omega_0} \psi' \cdot (\rho'_0 \dot{\mathbf{v}}^h) d\Omega_0 \\ & - \int_{\Omega} (\nabla_x \cdot \psi') p' d\Omega = -\langle \text{Res}_{\mathbf{v}}^h, \psi' \rangle, \end{aligned} \quad (97)$$

$$\begin{aligned} & \int_{\Omega_0} \psi' (\rho_0^h + \rho'_0) \dot{\epsilon}' d\Omega_0 + \int_{\Omega_0} \psi' \rho'_0 \dot{\epsilon}^h d\Omega_0 \\ & + \int_{\Omega} \psi' (\nabla_x \cdot (\mathbf{v}^h + \mathbf{v}')) p' d\Omega \\ & + \int_{\Omega} \psi' (\nabla_x \cdot \mathbf{v}') p^h d\Omega = -\langle \text{Res}_{\epsilon}^h, \psi' \rangle, \end{aligned} \quad (98)$$

where, for pure Dirichlet boundary conditions,  $\langle \text{Res}_{\mathbf{v}}^h, \cdot \rangle \in (\mathcal{S}'_{\kappa})^*$  and  $\langle \text{Res}_{\epsilon}^h, \cdot \rangle \in (\mathcal{S}'_{\gamma})^*$  are defined by pushing forward to the current configuration and integrating by parts:

$$\langle \text{Res}_{\mathbf{v}}^h, \mathbf{w} \rangle = \int_{\Omega} \mathbf{w} \cdot (\rho^h \dot{\mathbf{v}}^h + \nabla_x p^h) d\Omega, \quad (99)$$

$$\langle \text{Res}_{\epsilon}^h, w \rangle = \int_{\Omega} w (\rho^h \dot{\epsilon}^h + (\nabla_x \cdot \mathbf{v}^h) p^h) d\Omega. \quad (100)$$

As in the linear case, by means of the Riesz Representation Theorem, it is possible to identify the residual operators with the following members of the space  $(L^2(\Omega))^{n_d}$ , and  $L^2(\Omega)$ , respectively:

$$\text{Res}_{\mathbf{v}}^h = \rho^h \dot{\mathbf{v}}^h + \nabla_x p^h, \quad (101)$$

$$\text{Res}_{\epsilon}^h = \rho^h \dot{\epsilon}^h + (\nabla_x \cdot \mathbf{v}^h) p^h. \quad (102)$$

We now need to make further assumptions about the subgrid dynamics, to obtain a treatable fine-scale problem. The fundamental idea is to explore a simple solution *ansatz*, inspired by the results already obtained in the linear wave propagation case.

#### Fine-scale conditions

- (vi) Recalling the structure of the momentum equation (25), we can assume the following structure for the fine-scale velocity:

$$\mathbf{v}' = -\tau \rho^h \frac{(c_s^h)^2}{p^h} \frac{\partial \epsilon}{\partial p} \Big|_{\rho}^h \text{Res}_{\mathbf{v}}^h, \quad (103)$$

where  $\tau$  is defined as in (61). This produces the stabilizing term

$$p^h \mathbf{v}' = -\rho^h \frac{\partial \epsilon}{\partial p} \Big|_{\rho}^h \tau (c_s^h)^2 \text{Res}_{\mathbf{v}}^h, \quad (104)$$

in the coarse-scale energy equation (94). The specific scaling in front of the momentum residual in (103) (and also (104)) is chosen so that the stabilized formulation respects the structure of the nonlinear wave problem analyzed in Section 2.2. This observation becomes more clear when looking at the final form of the stabilizing operators, to be presented momentarily.

- (vii) Recalling the structure of the energy equation (26), we have that  $\text{Res}_{\epsilon}^h = \rho^h \frac{\partial \epsilon}{\partial p} \Big|_{\rho}^h \text{Res}_p^h$ , with

$$\text{Res}_p^h = \dot{p}^h + \rho^h (c_s^h)^2 \nabla_x \cdot \mathbf{v}^h. \quad (105)$$

It was shown in [56] that the expression for  $\text{Res}_p^h$  can also be derived by considering isentropic processes in perfect materials (materials free from internal dissipation mechanisms). It was also observed in [55, 56] that  $\text{Res}_p^h$  measures the *production* of entropy due to the numerical discretization. In regions of smooth flow,  $\text{Res}_p^h$  should vanish, but because of algorithmic instabilities, entropy can be *numerically* generated. At this point, it becomes natural to use the pressure residual to build an approximation to the fine-scale pressure as follows:

$$p' = -\tau \text{Res}_p^h. \quad (106)$$

It was shown in [56] that the same approximation can be obtained by taking the difference  $p' = p - p^h$  and linearizing the equation of state  $p = \hat{p}(\rho, \epsilon)$  about  $p^h$ . Because the system of equations at hand has the structure of a nonlinear wave equation, it makes sense to use the same parameter  $\tau$  in both the momentum and energy equations (see also Section 6 for more details on this interpretation from the point view of the von Neumann analysis of stability).

**Remark5.** In [56], the variational multiscale approach was used to stabilize formulations with piece-wise constant thermodynamic variables, enriching the discrete pressure by a fine-scale pressure defined as in (106). In the present approach, we also add the contribution of the fine-scale velocity  $\mathbf{v}'$  to stabilize the energy equation.

**Remark6.** By definition, the terms  $\mathbf{v}'$  and  $p'$  vanish at pure contact discontinuities, where the pressure and velocity are constant in space and time, and perfectly matched (equal) across the contact interface. Therefore, interpreting the term  $p^h \mathbf{v}'$  as an artificial heat flux would be *utterly incorrect*. This term, instead, represents the work produced by the interaction between the fine-scale velocity and the coarse-scale pressure.

**Remark7.** When shock waves are present in the material, the analysis just presented does not apply. From a physical point of view, a shock wave is an infinitely thin layer in which the



flow does not behave as a perfect material, due to internal dissipation mechanisms. At the numerical level, these irreversible mechanisms are introduced by shock-capturing operators in the form of artificial viscosities, which smear the discontinuity over a few cells of the computational grid.

Recalling that  $\text{Res}_\epsilon^h = \rho^h \partial_p \epsilon_p^h \text{Res}_p^h$  and collecting terms, (93)–(94) can also be written as

$$0 = \int_{\Omega} \psi^h \cdot (\rho^h \mathbf{v}^h) \, d\Omega - \int_{\Omega} \nabla_x \cdot \psi^h p^h \, d\Omega + \int_{\Omega} \nabla_x \cdot \psi^h \tau (\dot{p}^h + \rho^h (c_s^h)^2 \nabla_x \cdot \mathbf{v}^h) \, d\Omega, \quad (107)$$

$$0 = \int_{\Omega} \rho^h \frac{\partial \epsilon}{\partial p} \Big|_p^h (\psi^h (\dot{p}^h + \rho^h (c_s^h)^2 \nabla_x \cdot \mathbf{v}^h)) \, d\Omega + \int_{\Omega} \rho^h \frac{\partial \epsilon}{\partial p} \Big|_p^h (\tau (c_s^h)^2 \nabla_x \psi^h \cdot (\rho^h \mathbf{v}^h + \nabla_x p^h)) \, d\Omega + \int_{\Omega} \psi^h \nabla_x \cdot \mathbf{v}^h \tau (\dot{p}^h + \rho^h (c_s^h)^2 \nabla_x \cdot \mathbf{v}^h) \, d\Omega. \quad (108)$$

Equations (107)–(108) do not represent the practical implementation of the proposed method (see instead Section 4), but are very insightful in the interpretation of the stabilization mechanisms introduced. In fact, it is easy to appreciate that (107) bears striking similarities to (67). The first two terms in equation (108) resemble the terms in (68) scaled by  $\rho^h \partial_p \epsilon_p^h$ . Also note that for an ideal gas

$$\rho^h \partial_p \epsilon_p^h = 1/(\gamma - 1), \quad (109)$$

and the connection between (108) and its linear counterpart (68) is even more stringent. Stabilization is provided by the term

$$\int_{\Omega} \tau (c_s^h)^2 \rho^h (\nabla_x \cdot \psi^h) (\nabla_x \cdot \mathbf{v}^h) \, d\Omega, \quad (110)$$

in the momentum equation (107), and by the terms

$$\int_{\Omega} \tau (c_s^h)^2 \rho^h \frac{\partial \epsilon}{\partial p} \Big|_p^h (\nabla_x \psi^h \cdot \nabla_x p^h) \, d\Omega, \quad (111)$$

$$\int_{\Omega} \tau (c_s^h)^2 \psi^h \rho^h (\nabla_x \cdot \mathbf{v}^h)^2 \, d\Omega, \quad (112)$$

in the energy equation (108). As in the linear wave propagation case, these stabilizing terms are scaled by the acoustic-type kinematic viscosity  $\tau (c_s^h)^2$ . Analogous to the linear case, since the stabilized formulation is residual-based and variationally consistent, it does not produce a degradation of the order of accuracy, as shown in Section 6.

The value  $c_\tau = 2$  (for which  $\tau = \Delta t$ , see Section 3.1.2) seems to give best results in the nonlinear computations using the algorithm described in Section 4. The von Neumann analysis of stability documented in Section 6 shows that this choice corresponds to very low dispersion error in the linearized version of such algorithm.

#### 4. A predictor/multi-corrector time integrator

This section provides a specific implementation of the variational multiscale approach, using an explicit iterative time integrator, derived by applying a predictor/multi-corrector strategy to the well-known mid-point method. The proposed formulation conserves mass, momentum and total energy without resorting to any staggered approach in time, and stems from previous work in [56] (and also from similar ideas developed in the context of *mimetic* or *compatible* discretizations [3, 14]).

The time discretization is directly applied to the formulation given by equations (71)–(74). The time step is indicated by  $\Delta t$ , and the mid-point value of a quantity  $f$  is defined as:

$$f_{n+1/2} = \frac{f_n + f_{n+1}}{2}, \quad (113)$$

where  $f_n = f(t_n)$ .

The function spaces are given by (75)–(78). Note that in contrast with previous work in [53], the density is also expressed with piece-wise linear continuous functions.

For the sake of generality, the term  $\tilde{\sigma}$  is used in place of  $\sigma$ , denoting the generalized symmetric algorithmic stress tensor

$$\tilde{\sigma} = -p^h \mathbf{I} + \sigma_{vms} + \sigma_{art}, \quad (114)$$

where  $\sigma_{vms}$  is a variational multiscale stabilizing stress tensor, and  $\sigma_{art}$  is an artificial viscosity stress tensor, designed to capture shock layers. Analogously,  $\tilde{\mathbf{q}}$  is used in place of  $\mathbf{q}$ , to denote the algorithmic flux vector,

$$\tilde{\mathbf{q}} = \mathbf{q}^h + \lambda_{vms} + \lambda_{art}, \quad (115)$$

where  $\lambda_{art}$  is an artificial, shock-capturing vector flux, and  $\lambda_{vms}$  is a variational multiscale stabilizing vector flux. Both  $\sigma_{vms}$  and  $\lambda_{vms}$  are residual-based quantities. Specific derivations and definitions for the terms  $\tilde{\sigma}$  and  $\tilde{\mathbf{q}}$  will be given in subsequent sections. For reasons that will become completely clear subsequently (see Section 4.3 and Section 4.4),  $\lambda_{vms}$  and  $\lambda_{art}$  *do not* possess the structure of heat fluxes, and this terminology is therefore inappropriate. For the sake of simplicity, in the discussion that follows, it is assumed that the body force  $\mathbf{b}$ , the heat flux  $\mathbf{q}^h$  and the heat source/sink  $r$  are absent.

##### 4.1. A point of departure: The mid-point integrator

The predictor/multi-corrector approach pursued here stems from a classical, implicit, mid-point time integrator. In particular, the predictor/multi-corrector scheme is equivalent to a fixed-point iterative solution strategy of the nonlinear system of equations associated with the mid-point method. It is then important to briefly summarize the discrete equations associated with the latter before attacking the presentation of the former. In this section, with slight abuse of notation, the superscript “ $h$ ” - denoting numerical discretization - is omitted from the solution variables, discrete gradient operators, and the domain geometry.

#### 4.1.1. Momentum balance

Discretizing (73) in time yields:

Find  $\mathbf{v} \in \mathcal{S}_K^h$ , such that,  $\forall \psi^h \in \mathcal{V}_K^h$ ,

$$\begin{aligned} 0 = & \int_{\Omega_0} \psi^h \cdot \rho_0 (\mathbf{v}_{n+1} - \mathbf{v}_n) \, d\Omega_0 \\ & + \Delta t \int_{\Omega_{n+1/2}} (\nabla_x \psi^h)_{n+1/2} : \tilde{\sigma}_{n+1/2} \, d\Omega \\ & - \Delta t \int_{\Gamma_{n+1/2}^h} \psi^h \cdot \mathbf{t}_{n+1/2} \, d\Gamma, \end{aligned} \quad (116)$$

where the physical traction  $\mathbf{t}$  acts only on the Neumann boundary (i.e.,  $\mathbf{t}|_{\Gamma^g} = 0$ ). The variational form (116) yields the following discrete equations, for the nodal vector  $\mathbf{v}$  of velocity degrees-of-freedom:

$$[\mathbf{M}_v] (\mathbf{v}_{n+1} - \mathbf{v}_n) + \Delta t \mathbf{F}_{n+1/2} = \mathbf{0}, \quad (117)$$

where mass lumping has been applied to

$$[\mathbf{M}_v] = [\text{diag}(\mathbf{M}_0, \mathbf{M}_0, \mathbf{M}_0)], \quad (118)$$

a diagonal  $[(n_d \times n_{np}) \times (n_d \times n_{np})]$ -matrix ( $n_{np}$  is the number of nodes in the mesh). Specifically, using  $N_A$  to indicate the shape function associated with node  $A$  in the global node numbering, the vector  $\mathbf{M}_0$  is defined as

$$\mathbf{M}_0 = \{M_{0;A}\}, \quad (119)$$

$$M_{0;A} = \int_{\Omega_0} N_A \rho_0 \, d\Omega_0. \quad (120)$$

Analogously,  $\mathbf{F}_{n+1/2}$  is a  $(n_d \times n_{np})$ -vector:

$$\mathbf{F}_{n+1/2} = \{\mathbf{F}_{n+1/2;A}\}, \quad (121)$$

$$\mathbf{F}_{n+1/2;A} = \int_{\Omega_{n+1/2}} \tilde{\sigma}_{n+1/2} (\nabla_x N_A)_{n+1/2} \, d\Omega - \int_{\Gamma_{n+1/2}} N_A \mathbf{t}_{n+1/2} \, d\Gamma. \quad (122)$$

#### 4.1.2. Energy balance

Discretizing (74) in time yields:

Find  $\epsilon \in \mathcal{S}_\gamma^h$ , such that,  $\forall \psi^h \in \mathcal{V}_\gamma^h$ ,

$$\begin{aligned} 0 = & \int_{\Omega_0} \psi^h \rho_0 (\epsilon_{n+1} - \epsilon_n) \, d\Omega_0 \\ & - \Delta t \int_{\Omega_{n+1/2}} \psi^h (\nabla_x \mathbf{v})_{n+1/2} : \tilde{\sigma}_{n+1/2} \, d\Omega \\ & - \int_{\Omega_{n+1/2}} \nabla_x \psi^h \cdot \tilde{\mathbf{q}}_{n+1/2} \, d\Omega, \end{aligned} \quad (123)$$

so that an update equation for the nodal vector  $\epsilon$  of internal energy degrees-of-freedom can be derived:

$$[\mathbf{M}_\epsilon] (\epsilon_{n+1} - \epsilon_n) + \Delta t \mathbf{W}_{n+1/2} = \mathbf{0}, \quad (124)$$

where  $[\mathbf{M}_\epsilon] = [\text{diag}(\mathbf{M}_0)]$ , and  $\mathbf{W}_{n+1/2}$  is a  $n_{np}$ -dimensional vector defined as

$$\mathbf{W}_{n+1/2} = \{\mathbf{W}_{n+1/2;A}\}, \quad (125)$$

$$\begin{aligned} \mathbf{W}_{n+1/2;A} = & - \int_{\Omega_{n+1/2}} N_A (\nabla_x \mathbf{v})_{n+1/2} : \tilde{\sigma}_{n+1/2} \, d\Omega \\ & + \int_{\Omega_{n+1/2}} (\nabla_x N_A) \cdot \tilde{\mathbf{q}}_{n+1/2} \, d\Omega. \end{aligned} \quad (126)$$

#### 4.1.3. Mass balance

The mass conservation equation (72) can be slightly rearranged to yield:

Find  $\rho \in \mathcal{S}_\gamma^h$ , such that,  $\forall \psi^h \in \mathcal{V}_\gamma^h$ ,

$$\int_{\Omega_0} \psi^h \rho_0 \, d\Omega_0 = \int_{\Omega_0} \psi^h \rho J \, d\Omega_0 = \int_{\Omega} \psi^h \rho \, d\Omega. \quad (127)$$

Testing the previous equation using nodal shape functions yields

$$[\mathbf{V}_{n+1}] \rho_{n+1} = \mathbf{M}_0, \quad (128)$$

where  $\rho_{n+1}$  is the vector of nodal degrees-of-freedom for the density at  $t_{n+1}$ , that is,

$$\rho_{n+1} = \{\rho_{n+1;A}\}, \quad (129)$$

and  $[\mathbf{V}_{n+1}] = [\text{diag}(\mathbf{V}_{n+1})]$  is the diagonal matrix of (lumped) nodal volumes, with

$$\mathbf{V}_{n+1} = \{\mathbf{V}_{n+1;A}\}, \quad (130)$$

$$\mathbf{V}_{n+1;A} = \int_{\Omega_0} N_A J_{n+1} \, d\Omega_0 = \int_{\Omega_{n+1}} N_A \, d\Omega. \quad (131)$$

**Remark8.** Following the finite-volume method nomenclature, the interpretation of  $\{\mathbf{V}_{n+1}\}$  is analogous to a vector of (nodal) co-volumes.

#### 4.1.4. Displacement equations

Positions are updated from velocities using a weak projection, rather than using a set of ordinary differential equations for the nodal positions. The time-discretization of the rate equations for the position yields:

Find  $\mathbf{u} \in \mathcal{S}_\gamma^h$ , such that,  $\forall \psi^h \in \mathcal{V}_\gamma^h$ ,

$$\int_{\Omega_0} \psi^h \cdot (\mathbf{u}_{n+1} - \mathbf{u}_n) \, d\Omega_0 - \Delta t \int_{\Omega_0} \psi^h \cdot \mathbf{v}_{n+1/2} \, d\Omega_0 = 0. \quad (132)$$

The vector  $\mathbf{u}$  of nodal displacements can be computed with an explicit procedure very similar in structure to the discrete momentum update:

$$\mathbf{u}_{n+1} - \mathbf{u}_n - \Delta t \hat{\mathbf{v}}_{n+1/2} = \mathbf{0}, \quad (133)$$

with

$$\hat{\mathbf{v}}_{n+1/2} = \{\hat{\mathbf{v}}_{n+1/2;A}\}, \quad (134)$$

$$\hat{\mathbf{v}}_{n+1/2;A} = \mathbf{V}_{0;A}^{-1} \left( \int_{\Omega_0} N_A \mathbf{v}_{n+1/2} \, d\Omega_0 \right). \quad (135)$$

Note that in the displacement update (133), the inverse of a lumped volume matrix is premultiplied by the vector of nodal positions, and the velocities are tested against the nodal shape functions. This choice was preferred in [53] to the simpler (and more efficient) approach of integrating in time ordinary differential equations for the nodal displacements, namely

$$\mathbf{u}_{n+1} - \mathbf{u}_n - \Delta t \mathbf{v}_{n+1/2} = \mathbf{0}, \quad (136)$$

due to superior results in terms of mesh smoothness. In a number of tests with the proposed new method, not reported here for the sake of brevity, it was observed that both (133) and (136) performed well, with only slight improvements in mesh smoothness in the case of (133). The numerical tests in Section 7 were performed using (133).

**Remark9.** An early attempt to apply the proposed displacement update to the more traditional finite element method in [56] (i.e., with thermodynamic variables *constant* on element interiors) proved disastrous. In fact, a number of basic tests performed with this combination could not be run to completion due to inversion of some of the element volumes. This fact seems to indicate that the proposed displacement update is effective *only* in the context of piece-wise linear approximation of thermodynamic variables.

#### 4.1.5. Equation of state

The equation of state is evaluated at each time step at the nodal points, and a nodal pressure is computed as a function of nodal internal energy and nodal density:

$$\sigma_{n+1} = -p_{n+1} \mathbf{I} = -\hat{p}(\rho_{n+1}, \epsilon_{n+1}) \mathbf{I}. \quad (137)$$

A piece-wise continuous pressure field is then interpolated from the vector  $\mathbf{p}$  of pressure nodal values. Therefore, we can write a discrete form of the pressure degrees-of-freedom update equation as follows:

$$\mathbf{p}_{n+1} = \hat{p}(\rho_{n+1}, \epsilon_{n+1}). \quad (138)$$

#### 4.2. A fixed-point, predictor/multi-corrector

The algorithm developed in Section 4.1 requires the inversion of a matrix: The force and work terms are computed at the mid-point in time, and necessitate knowledge of the solution at time  $t_{n+1}$ . However, a fully explicit procedure can be recovered by resorting to a predictor/multi-corrector approach. For this purpose, a number of preliminary definitions are needed. The state of the system at time  $t = t_n$  is defined by means of the vector  $\mathbf{Y}_n = [\mathbf{u}_n^T, \mathbf{v}_n^T, \rho_n^T, \epsilon_n^T, \mathbf{p}_n^T]^T$ . As described in Table 1, the proposed approach consists of a velocity update, followed, in order, by internal energy, position, density and pressure (or, more generally, stress) updates.  $\mathbf{F}_{n+1/2}^{(i)}$  indicates the evaluation of  $\mathbf{F}_{n+1/2}$  using the state  $\mathbf{Y}$  at iterate  $(i)$ . The definition of the iterate of the work vector  $\mathbf{W}_{n+1/2}^{(i,j)}$  is somewhat different, since

$$\mathbf{W}_{n+1/2}^{(i,j)} = \{\mathbf{W}_{n+1/2;A}^{(i,j)}\}, \quad (139)$$

$$\begin{aligned} \mathbf{W}_{n+1/2;A}^{(i,j)} = & - \int_{\Omega_{n+1/2}^{(i)}} N_A ((\nabla_x)^{(i)}_{n+1/2} \mathbf{v}_{n+1/2}^{(j)}) : \tilde{\sigma}_{n+1/2}^{(i)} d\Omega \\ & + \int_{\Omega_{n+1/2}^{(i)}} ((\nabla_x)^{(i)}_{n+1/2} N_A) \cdot \tilde{\mathbf{q}}_{n+1/2}^{(i)} d\Omega. \end{aligned} \quad (140)$$

Here  $(\nabla_x)^{(i)}_{n+1/2}$  and  $\mathbf{v}_{n+1/2}^{(j)}$  indicate the (current configuration) gradient operator and the velocity field at  $t = t_{n+1/2}$  and iterate  $i$  and  $j$ , respectively. In the case of the proposed predictor corrector,  $j = i + 1$ . This notation is needed to understand how conservation is enforced *at each iteration* of the predictor/multi-corrector procedure.

Table 1: Outline of the predictor/multi-corrector algorithm. Note that, because of mass lumping, all matrices are diagonal, so that all inverse operations are just vector divisions. Three iterations were typically used in the computations.

Retrieve loop parameters: $n_{\text{step}}, i_{\text{max}}$
Initialize all variables with initial conditions
Form $\mathbf{M}_0$ , $[\mathbf{M}_v]$ , and $[\mathbf{M}_\epsilon]$
<b>For</b> $n = 0, \dots, n_{\text{step}}$ ( <i>Time-step loop begins</i> )
Set $\Delta t$ (respecting the CFL condition)
Predictor: $\mathbf{Y}_{n+1}^{(0)} = \mathbf{Y}_n$
<b>For</b> $i = 0, \dots, i_{\text{max}} - 1$ ( <i>Multi-corr. loop begins</i> )
Assembly: $\mathbf{F}_{n+1/2}^{(i)}$
Velocity update: $\mathbf{v}_{n+1}^{(i+1)} = \mathbf{v}_n - \Delta t [\mathbf{M}_v]^{-1} \mathbf{F}_{n+1/2}^{(i)}$
Assembly: $\mathbf{W}_{n+1/2}^{(i,i+1)}$
Energy update: $\epsilon_{n+1}^{(i+1)} = \epsilon_n - \Delta t [\mathbf{M}_\epsilon]^{-1} \mathbf{W}_{n+1/2}^{(i,i+1)}$
Position update: $\mathbf{u}_{n+1}^{(i+1)} = \mathbf{u}_n + \Delta t \mathbf{v}_{n+1}^{(i+1)}$
Volume update: $\mathbf{V}_{n+1}^{(i+1)} = \mathbf{V}(\mathbf{u}_{n+1}^{(i+1)})$
Density update: $\rho_{n+1}^{(i+1)} = [\mathbf{V}_{n+1}^{(i+1)}]^{-1} \mathbf{M}_0$
Pressure update: $\mathbf{p}_{n+1}^{(i+1)} = \hat{p}(\rho_{n+1}^{(i+1)}, \epsilon_{n+1}^{(i+1)})$
<b>End</b> ( <i>Multi-corrector loop ends</i> )
Time update: $\mathbf{Y}_{n+1} = \mathbf{Y}_{n+1}^{(i_{\text{max}})}$
<b>End</b> ( <i>Time-step loop ends</i> )
<b>Exit</b>

#### 4.3. Implementation of the variational multiscale stabilization

Recalling the structure of the algorithmic stress (114) and the algorithmic vector flux (115), we have:

$$\sigma_{vms} = -p' \mathbf{I}, \quad (141)$$

$$\lambda_{vms} = p^h \mathbf{v}', \quad (142)$$

where equations (141) and (142) correspond to equation (106) and (104), respectively. Then, we just need to discretize in time (106) and (104). In the context of the proposed predictor/multi-corrector method, this amounts to setting

$$p' = -\tau (\text{Res}_p^h)^{(i)}_{n+1/2}, \quad (143)$$

$$\mathbf{v}' = -\tau \left( \rho \frac{\partial \epsilon}{\partial p} \bigg|_{\rho} \frac{c_s^2}{p} \right)_{n+1/2}^{h;(i)} (\text{Res}_v^h)^{(i,i+1)}_{n+1/2}, \quad (144)$$

with

$$(\text{Res}_p^h)^{(i)}_{n+1/2} = \frac{p_{n+1}^{h;(i)} - p_n^h}{\Delta t} + (\rho c_s^2 \nabla_x \cdot \mathbf{v})_{n+1/2}^{h;(i)}, \quad (145)$$

$$(\text{Res}_v^h)^{(i,i+1)}_{n+1/2} = \rho_{n+1/2}^{h;(i)} \frac{\mathbf{v}_{n+1}^{h;(i+1)} - \mathbf{v}_n^h}{\Delta t} + (\nabla_x p)_{n+1/2}^{h;(i)}. \quad (146)$$

The definition of the stabilization parameter is slightly different from the one given in (61):

$$\tau = c_\tau \frac{\Delta t \text{CFL}_{\text{nominal}}}{2 \text{CFL}_{\text{actual}}}. \quad (147)$$

Here  $CFL_{nominal}$  is the target global *Courant-Friedrichs-Lewy* (CFL) number (specified by the user) while  $CFL_{actual}$  is the actual CFL number at time  $t$ . In practice the ratio  $CFL_{nominal}/CFL_{actual}$  is almost always unity, so that  $\tau$  perfectly matches definition (61). The only exceptions are the startups of highly transient computations, in which time steps are initially forced to be very small and are progressively increased to nominal values by means of a compound (exponential growth) scaling. Under these conditions, the parameter  $\tau$  defined in (61), because of the scaling with  $\Delta t$ , would be extremely small, negatively affecting the spatial stability of the overall algorithm. After the initial transient has elapsed (typically involving between 30 and 50 time steps), the ratio  $CFL_{nominal}/CFL_{actual}$  becomes and stays equal to unity. The value  $c_\tau = 2$  (for which  $\tau = \Delta t$ ) was used in the numerical experiments presented in Section 7. The value  $c_\tau = 2$  (for which  $\tau = \Delta t$ ) appeared to give the best results in a series of numerical experiments, although values in the range  $[1/2, 3]$  proved also effective. The analysis of stability and accuracy presented in Section 6 shows that three iterations of the predictor/multi-corrector method, in combination with  $c_\tau = 2$  and a safety parameter  $CFL = 0.8$  yield very good performance (see also Section 6). This is because the method is characterized by high wave number dissipation, accurate low wave number behavior, and very low dispersion error over the entire wave number spectrum. These theoretical findings were confirmed in computations, not reported here, for the sake of brevity.

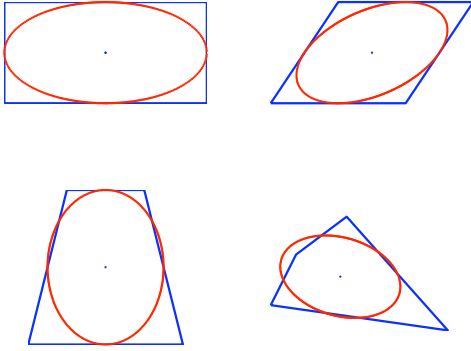


Figure 2: Sketch of the length-scale  $h_{art}$  as a function of the direction of  $\mathbf{n}_{sh}$ . The plots show the envelope of  $h_{art}$  as the angle that  $\mathbf{n}_{sh}$  forms with the  $x_1$ -axis varies from 0 to 360 degrees. Note the smooth transition of the length-scale near the corners of the elements.

#### 4.4. Artificial viscosity and discontinuity capturing operator

The discontinuity capturing operator is given by:

$$\sigma_{art} = \begin{cases} \rho v_{art,y} \nabla_x^s \mathbf{v} & \text{if } \nabla_x \cdot \mathbf{v} < 0, \\ \mathbf{0}_{n_d \times n_d} & \text{otherwise.} \end{cases} \quad (148)$$

$$\lambda_{art} = \begin{cases} \rho \partial_p \epsilon|_\rho v_{art,p} \nabla_x p & \text{if } \nabla_x \cdot \mathbf{v} < 0, \\ \mathbf{0}_{n_d} & \text{otherwise.} \end{cases} \quad (149)$$

The scaling and structure of  $\lambda_{art}$  are chosen with the purpose of dissipating pressure oscillations in the energy equation. The artificial viscosities are

$$v_{art,y} = c_1 |\nabla_x \cdot \mathbf{v}| h_{art}^2, \quad (150)$$

$$v_{art,p} = c_2 \sqrt{\frac{|\nabla_x p|}{\rho}} h_{art}^{3/2}, \quad (151)$$

The values  $c_1 = 1.4$  and  $c_2 = 1.0$  were found to perform best in the computations of Section 7. There is however some flexibility in the choice of the viscosity constant, as comparable results were obtained also with different combinations of values. The values  $c_1 = 1.4$  and  $c_2 = 1.0$  were chosen so that  $v_{art,y}$  and  $v_{art,p}$  peak at about the same value in computations, while maintaining a slightly different spatial variation (see, e. g., the numerical examples in Section 7, where both artificial viscosities are plotted).

Possibly the most striking peculiarity of the adopted discontinuity operator is the introduction of the diffusive term  $\lambda_{art}$  in the energy equation. This approach is in clear contrast with [56], and was already explored in [53]. One would be tempted to think about  $\lambda_{art}$  as an artificial heat flux, but this interpretation would be incorrect. In fact, the term  $\lambda_{art}$  involves only pressure gradients, and not temperature (i.e., internal energy) gradients. Most importantly, the term  $\lambda_{art}$  is not active at contact discontinuities, where the pressure is continuous and typically constant.  $\lambda_{art}$  is only active where shocks are present, and because the corresponding artificial viscosity does not scale with the speed of sound, this term is expected to be negligible also in compression regions characterized by small pressure gradients.

**Remark10.** Artificial viscosities implemented in traditional hydrocodes also include a linear scaling with the speed of sound, to control acoustic oscillations past shock fronts [6]. For the present method, instead, best computational results were obtained using only a quadratic viscosity of von Neumann-Richtmyer type [6, 65]. This indicates that the variational multiscale stabilization in (69)–(70) performed well in controlling numerical instabilities of acoustic (e.g., hourglass) nature.

**Remark11.** The definition (148) is more effective in damping artificial pure shear motion, with respect to the more common definition [6]

$$\sigma_{art} = -(\rho v_{art} \nabla_x \cdot \mathbf{v}) \mathbf{I}. \quad (152)$$

Artificially produced homogeneous shear motion can have disruptive consequences on shock hydrodynamics computations of fluids, since it is not resisted by hourglass controls (of any type), nor the discretized physical stress.

**Remark12.** The use of the symmetric part rather than the full gradient of the velocity gradient in definition (148) ensures that angular momentum and algorithmic objectivity are preserved in computations. For more details, see [39].

The length-scale  $h_{art}$  is defined in a similar fashion to [53], and is designed to *stably* sample a mesh length along the normal to the shock front. This means that, for a given mesh,  $h_{art}$

should not vary abruptly for small changes in the direction of the shock normal. An effective definition was found to be

$$h_{art} = \frac{2}{\sqrt{\mathbf{n}_{sh}^T (\mathbf{F}_\square \mathbf{F}_\square^T)^{-1} \mathbf{n}_{sh}}}, \quad (153)$$

$$\mathbf{F}_\square = \frac{\partial \mathbf{x}}{\partial \xi}, \quad (154)$$

where  $\mathbf{n}_{sh}$  is a unit vector in the direction normal to the shock front, and  $\mathbf{F}_\square$  the gradient of the mapping from the element's parent domain to its current configuration. In practice,  $(\mathbf{F}_\square \mathbf{F}_\square^T)$  measures the *stretch* in the direction given by  $\mathbf{n}_{sh}$ . A plot of the envelope of  $h_{art}$  as the shock normal angle spans the interval  $[0, 360]$ -degrees is presented in Figure 2, for various quadrilateral elements. This definition is analogous to the one adopted in [32]. A reliable approximation to  $\mathbf{n}_{sh}$  was found to be:

$$\mathbf{n}_{sh} = \frac{0.75 \frac{\dot{\mathbf{v}}}{\|\dot{\mathbf{v}}\|} + 0.25 \frac{\nabla_x \rho}{\|\nabla_x \rho\|}}{\left\| 0.75 \frac{\dot{\mathbf{v}}}{\|\dot{\mathbf{v}}\|} + 0.25 \frac{\nabla_x \rho}{\|\nabla_x \rho\|} \right\|}. \quad (155)$$

Basically, the direction of the shock normal is a weighted average of the direction of the acceleration vector  $\dot{\mathbf{v}}$ , and the density gradient (see also [63, 64]). Again, there is some flexibility in the definition of the shock direction, and alternative choices are possible.

## 5. Invariance and conservation properties

### 5.1. Galilean invariance and frame objectivity

A Galilean transformation of reference frames is a translation by a constant velocity  $\mathbf{V}^G$ . Particularly, the transformed velocity is given by  $\tilde{\mathbf{v}} = \mathbf{v} - \mathbf{V}^G$ , where  $\mathbf{v}$  is the velocity prior to the frame change. Accordingly, the spatial and temporal coordinates transform as

$$\begin{bmatrix} \tilde{t} \\ \tilde{\mathbf{x}} \end{bmatrix} = \begin{bmatrix} 1 & \mathbf{0}_{1 \times n_d} \\ -\mathbf{V}^G & \mathbf{I}_{n_d \times n_d} \end{bmatrix} \begin{bmatrix} t \\ \mathbf{x} \end{bmatrix}. \quad (156)$$

Observing that  $d\tilde{\mathbf{x}} = d\mathbf{x}$ , and that a Lagrangian time derivative tracks a material particle irrespective of reference frames (i.e.,  $\tilde{X} = X$ ), it is also straightforward to obtain

$$\left. \frac{\partial}{\partial t} \right|_{\tilde{X}} = \left. \frac{\partial}{\partial t} \right|_X, \quad (157)$$

$$\nabla_x = \nabla_{\tilde{x}}. \quad (158)$$

It is then easy to verify that the proposed stabilization approach satisfies Galilean invariance properties, in both its abstract form (93)–(94) or the specific predictor/multi-corrector implementation detailed in Section 4. In fact, the velocity appears always in differentiated (or incremental) form with respect to space or time in all the terms in the formulation, including the variational multiscale and discontinuity capturing operators. Hence, after a Galilean transformation is applied, the structure of the discrete stabilized equations stays the same. Galilean invariance properties were recognized as important in [50–52, 54] in the

specific case of Lagrangian and arbitrary Lagrangian-Eulerian (ALE) computations.

It is also not very difficult to prove (see, e.g., [39]), that in the limit case of infinite iterations of the predictor/multi-corrector scheme (i.e., the mid-point time integrator), objectivity properties are also satisfied [59]. In the case of a finite number of iterations, it is shown in [39] that the error in objectivity is usually converging very fast, becoming negligible with respect to the numerical error in the computations. This is also in view of the specific form (148) of the artificial viscosity operator.

### 5.2. Global conservation for the mid-point integrator

A point of departure in the discussion is the analysis of global conservation properties for the mid-point integrator from which the predictor/multi-corrector algorithm is derived. In particular, mass and momentum conservation statements for the predictor/multi-corrector method are virtually identical to the ones developed for the mid-point implicit integrator, while small adjustments are needed in the proof of total energy conservation.

#### 5.2.1. Conservation of mass

Equation (128) (or, correspondingly, (127)) is a statement of global conservation of mass. This can be easily seen by testing (127) against a constant unit test function, which yields

$$\int_{\Omega_0} \rho_0 d\Omega_0 = \int_{\Omega} \rho d\Omega = \text{total mass}. \quad (159)$$

In the context of the discrete equations (with lumping applied to the second integral above), we can easily see that (159) is equivalent to contracting (128) with the vector  $\mathbf{1}$ , a  $n_{np}$ -dimensional vector whose entries are all unity, namely

$$\mathbf{1}^T [\mathbf{V}_{n+1}] \rho_{n+1} = \mathbf{1}^T \{\mathbf{M}_0\} = \text{discrete total mass}. \quad (160)$$

#### 5.2.2. Conservation of linear and angular momentum

Let us assume, as is customary when proving conservation statements, that only homogenous Neumann (zero-traction) boundary conditions are imposed, so that the test and trial function spaces for the velocities coincide (i.e.,  $\mathcal{S}_\kappa^h = \mathcal{V}_\kappa^h$ ). Testing (116) against the shape function  $\psi^h = \mathbf{e}_i$ ,  $i = 1, \dots, n_d$  (the *constant* unit vector of the Cartesian basis in the  $i$ th direction) yields a conservation statement for the global momentum in the direction  $\mathbf{e}_i$ . Namely, as the boundary term and the integral involving the test function gradient simplify, (116) yields

$$\begin{aligned} 0 &= \int_{\Omega_0} \rho_0 (v_{i,n+1} - v_{i,n}) d\Omega_0 \\ &= \int_{\Omega_{n+1}} \rho_{n+1} v_{i,n+1} d\Omega - \int_{\Omega_n} \rho_n v_{i,n} d\Omega, \end{aligned} \quad (161)$$

where  $v_i = \mathbf{v} \cdot \mathbf{e}_i$ . This is analogous to contracting the entries of vector equation (117) corresponding to the  $i$ th component against the vector  $\mathbf{1}$ :

$$\mathbf{1}^T [\mathbf{M}_{i,v}] (\mathbf{v}_{i,n+1} - \mathbf{v}_{i,n}) = \mathbf{0}, \quad (162)$$

where  $[\mathbf{M}_{i,v}]$  is the diagonal block of  $[\mathbf{M}_v]$  corresponding to the degrees-of-freedom  $\mathbf{v}_i$  associated with the  $i$ th direction. Under appropriate boundary conditions, an algorithmic form of the total angular momentum is also conserved (see [39] for a detailed discussion).

### 5.2.3. Conservation of total energy

We assume again homogenous Neumann boundary conditions, for which it is possible to test (117) with  $\psi^h = \mathbf{v}_{n+1/2}$ . With this choice as a test function, the kinetic energy balance for the system is obtained:

$$\begin{aligned} \frac{1}{2} \int_{\Omega_{n+1}} \rho_{n+1} (\mathbf{v} \cdot \mathbf{v})_{n+1} d\Omega - \frac{1}{2} \int_{\Omega_n} \rho_n (\mathbf{v} \cdot \mathbf{v})_n d\Omega \\ = -\Delta t \int_{\Omega_{n+1/2}} (\nabla_x \mathbf{v})_{n+1/2} : \tilde{\sigma}_{n+1/2} d\Omega, \end{aligned} \quad (163)$$

or, applying mass lumping and using vector notation,

$$\frac{1}{2} \mathbf{v}_{n+1}^T [\mathbf{M}_v] \mathbf{v}_{n+1} - \frac{1}{2} \mathbf{v}_n^T [\mathbf{M}_v] \mathbf{v}_n = -\Delta t \mathbf{v}_{n+1/2}^T \mathbf{F}_{n+1/2}. \quad (164)$$

The previous equations are derived using the following identity

$$\begin{aligned} \int_{\Omega_0} \rho_0 \mathbf{v}_{n+1/2} \cdot (\mathbf{v}_{n+1} - \mathbf{v}_n) d\Omega_0 \\ = \int_{\Omega_0} \frac{\rho_0}{2} ((\mathbf{v} \cdot \mathbf{v})_{n+1} - (\mathbf{v} \cdot \mathbf{v})_n) d\Omega_0 \\ = \int_{\Omega_{n+1}} \frac{\rho_{n+1}}{2} (\mathbf{v} \cdot \mathbf{v})_{n+1} d\Omega - \int_{\Omega_n} \frac{\rho_n}{2} (\mathbf{v} \cdot \mathbf{v})_n d\Omega, \end{aligned} \quad (165)$$

or, equivalently (recall  $[\mathbf{M}_v]$  is diagonal, therefore symmetric),

$$\begin{aligned} \frac{1}{2} \mathbf{v}_{n+1/2}^T [\mathbf{M}_v] (\mathbf{v}_{n+1} - \mathbf{v}_n) &= \frac{1}{2} (\mathbf{v}_{n+1}^T + \mathbf{v}_n^T) [\mathbf{M}_v] (\mathbf{v}_{n+1} - \mathbf{v}_n) \\ &= \frac{1}{2} \mathbf{v}_{n+1}^T [\mathbf{M}_v] \mathbf{v}_{n+1} - \frac{1}{2} \mathbf{v}_n^T [\mathbf{M}_v] \mathbf{v}_n. \end{aligned} \quad (166)$$

Testing (123) with a shape function equal to unity over the entire domain (i.e.,  $\psi_\gamma^h|_{\Omega_0} = 1$ ) yields

$$\begin{aligned} \int_{\Omega_{n+1}} (\rho \epsilon)_{n+1} d\Omega - \int_{\Omega_n} (\rho \epsilon)_n d\Omega \\ = \int_{\Omega_0} \rho_0 (\epsilon_{n+1} - \epsilon_n) d\Omega_0 \\ = \Delta t \int_{\Omega_{n+1/2}} (\nabla_x \mathbf{v})_{n+1/2} : \tilde{\sigma}_{n+1/2} d\Omega. \end{aligned} \quad (167)$$

or, equivalently,

$$\mathbf{1}^T [\mathbf{M}_\epsilon] (\epsilon_{n+1} - \epsilon_n) = -\Delta t \mathbf{1}^T \mathbf{W}_{n+1/2}. \quad (168)$$

In particular, recalling  $\sum_{A=1}^{n_{np}} N_A = 1$ ,

$$\begin{aligned} \mathbf{1}^T \mathbf{W}_{n+1/2} &= -\mathbf{1}^T \left\{ - \int_{\Omega_{n+1/2}} N_A (\nabla_x \mathbf{v})_{n+1/2} : \tilde{\sigma}_{n+1/2} d\Omega \right\} \\ &\quad + \mathbf{1}^T \left\{ \int_{\Omega_{n+1/2}} (\nabla_x N_A) \cdot \tilde{\mathbf{q}}_{n+1/2} d\Omega \right\} \\ &= - \int_{\Omega_{n+1/2}} \left( \sum_{A=1}^{n_{np}} N_A \right) (\nabla_x \mathbf{v})_{n+1/2} : \tilde{\sigma}_{n+1/2} d\Omega \\ &\quad + \int_{\Omega_{n+1/2}} \nabla_x \left( \sum_{A=1}^{n_{np}} N_A \right) \cdot \tilde{\mathbf{q}}_{n+1/2} d\Omega \\ &= - \int_{\Omega_{n+1/2}} (\nabla_x \mathbf{v})_{n+1/2} : \tilde{\sigma}_{n+1/2} d\Omega \\ &\quad + \int_{\Omega_{n+1/2}} \nabla_x (1) \cdot \tilde{\mathbf{q}}_{n+1/2} d\Omega \\ &= - \int_{\Omega_{n+1/2}} (\nabla_x \mathbf{v})_{n+1/2} : \tilde{\sigma}_{n+1/2} d\Omega. \end{aligned} \quad (169)$$

Comparing (121)–(122) with (125)–(126), and taking into account (169),

$$\mathbf{v}_{n+1/2}^T \mathbf{F}_{n+1/2} = -\mathbf{1}^T \mathbf{W}_{n+1/2}. \quad (170)$$

Summing (164) and (168), we derive a statement of conservation for an algorithmic total energy:

$$\frac{1}{2} \mathbf{v}_{n+1}^T [\mathbf{M}_v] \mathbf{v}_{n+1} + \mathbf{1}^T [\mathbf{M}_\epsilon] \epsilon_{n+1} = \frac{1}{2} \mathbf{v}_n^T [\mathbf{M}_v] \mathbf{v}_n + \mathbf{1}^T [\mathbf{M}_\epsilon] \epsilon_n. \quad (171)$$

**Remark13.** The approach followed in the proof of global conservation properties, is very similar to the one presented in [56], with the exception of the treatment of the term containing  $\tilde{\mathbf{q}}$ .

### 5.3. Conservation for the predictor/multi-corrector approach

The proposed predictor/multi-corrector approach maintains all the conservation properties of the base mid-point algorithm. The proofs are straightforward for mass and linear momentum conservation, but require special care in the case of total energy. In fact, the work vector  $\mathbf{W}_{n+1/2}^{(i,i+1)}$  (see Table 1) is computed holding the geometry and all the terms in the integral (140) at iterate ( $i$ ), while the velocity  $\mathbf{v}_{n+1/2}$  is evaluated using iterate ( $i+1$ ). This new iterate is readily available after the momentum equation is integrated in time (the predictor/multi-corrector mimics a Gauss-Seidel solution strategy). Using arguments virtually identical to the ones presented in Section 5.2, it is easy to realize that the identity

$$(\mathbf{v}_{n+1/2}^{(i+1)})^T \mathbf{F}_{n+1/2}^i = -\mathbf{1}^T \mathbf{W}_{n+1/2}^{(i,i+1)} \quad (172)$$

guarantees that total energy is conserved at *each iterate* of the predictor/multi-corrector algorithm, namely,

$$\frac{1}{2} (\mathbf{v}_{n+1}^{(i+1)})^T [\mathbf{M}_v] \mathbf{v}_{n+1}^{(i+1)} + \mathbf{1}^T [\mathbf{M}_\epsilon] \epsilon_{n+1}^{(i+1)} = \frac{1}{2} \mathbf{v}_n^T [\mathbf{M}_v] \mathbf{v}_n + \mathbf{1}^T [\mathbf{M}_\epsilon] \epsilon_n. \quad (173)$$

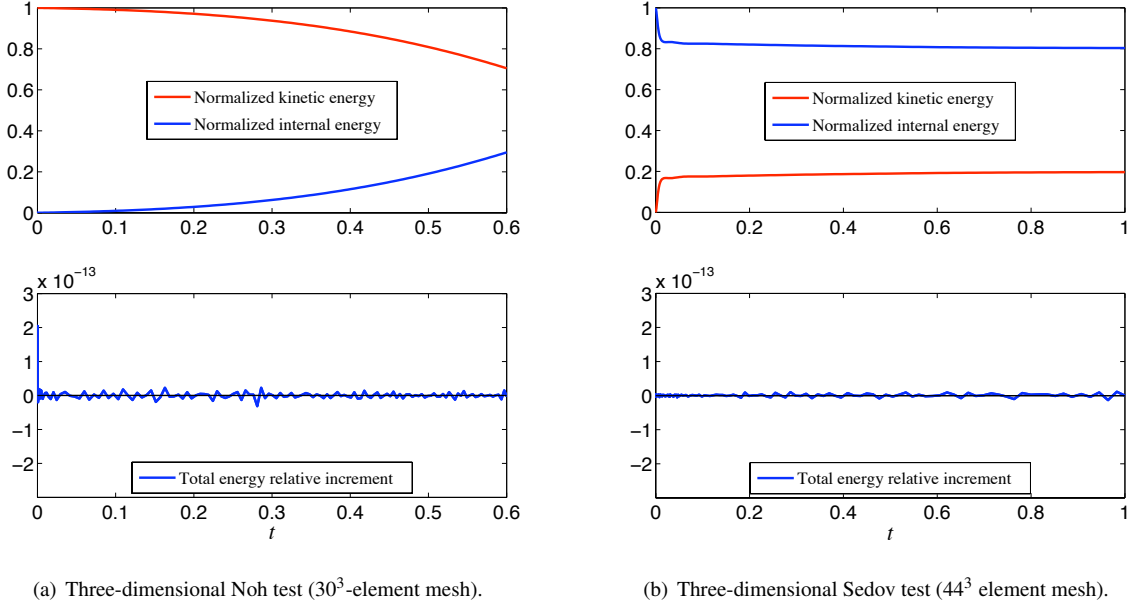


Figure 3: Energy history for a three-dimensional Noh test (3(a)), and a three-dimensional Sedov test (3(b)). The plots on the upper row show the change in the internal (blue line) and kinetic (red line) energies, normalized with the total energy. The plots on the lower row show the total energy ( $\mathcal{E}^{tot}$ ) relative increment between time  $t_n$ , and  $t_{n+1}$ , namely  $(\mathcal{E}_{n+1}^{tot} - \mathcal{E}_n^{tot})/\mathcal{E}_n^{tot}$ . Note the scale of the vertical axis is  $10^{-13}$  in the lower plots.

The time histories of the kinetic, internal and total energies presented in Figure 3 confirm, within machine precision, the conservation properties of the proposed algorithm in the case of a three-dimensional Noh test (Fig. 3(a)), and a three-dimensional Sedov test (Fig. 3(b)). The reader can refer to Section 7 for more details on the setup of these tests.

**Remark14.** It is important to realize that the proposed variational multi-scale approach is not limited in scope to the peculiar time integrator described here. In particular, it would be possible to implement a similar approach using Runge-Kutta integrators. In order to preserve global conservation of total energy (proofs of mass and momentum conservation do not usually require much effort), it is fundamental to verify that an identity analogous to (172) takes place, and to ensure that the overall algorithmic definitions of kinetic and total energy retain physical significance.

## 6. Algorithmic spectral analysis

This section is fundamental for the design of the overall algorithm, since it correlates the choice of the stabilization parameter  $c_\tau$  with the fundamental algorithmic properties in terms of stability, accuracy, dispersion and dissipation. The analysis is restricted to the one-dimensional periodic case, for the linearized system of equations. Diffusive effects due to the artificial viscosity operators are also accounted for, leading to stable time-step estimates that work in the nonlinear case with shocks.

The reader not interested in the details of derivations can skip this section in a first reading, and retain the main results summarized below:

1. The method is stable for all iterates of the predictor/multi-corrector, with (200) as Courant-Friedrichs-Lewy stability condition.
2. Very good dispersion and high-wavenumber dissipation properties are obtained with three iterations of the predictor/multi-corrector, when  $c_\tau = 2$  and the Courant-Friedrichs-Lewy factor is 0.8.
3. The results of the linearized analysis are also confirmed in a large number of nonlinear numerical computations, in part included in the present article.

These conclusions are obtained by performing the von Neumann analysis of dissipation and dispersion properties for the stabilized algorithm obtained from the discretization of (67)–(68). More precisely, equations (67)–(68) are augmented by diffusive operators derived from the linearization of the discontinuity capturing operators (148)–(149), and integrated in time using the predictor/multi-corrector algorithm described in Section 4.2. The interested reader can find the detailed derivations in Appendix A.

### 6.1. Stability

Consider a one-dimensional, periodic domain, and the proposed stabilized method on a uniform grid. Appendix A shows that, applying the Discrete Fourier Transform (DFT) to the degrees-of-freedom of the discrete solution, the evolution of the  $k$ th velocity/pressure Fourier modal pair relative to the  $n$ th time step and the  $i$ th iterate, namely

$$\hat{\mathbf{Z}}_{k,n}^{(i)} = \begin{Bmatrix} \hat{\mathbf{V}}_{k,n}^{(i)} \\ \hat{\mathbf{P}}_{k,n}^{(i)} \end{Bmatrix}, \quad (174)$$



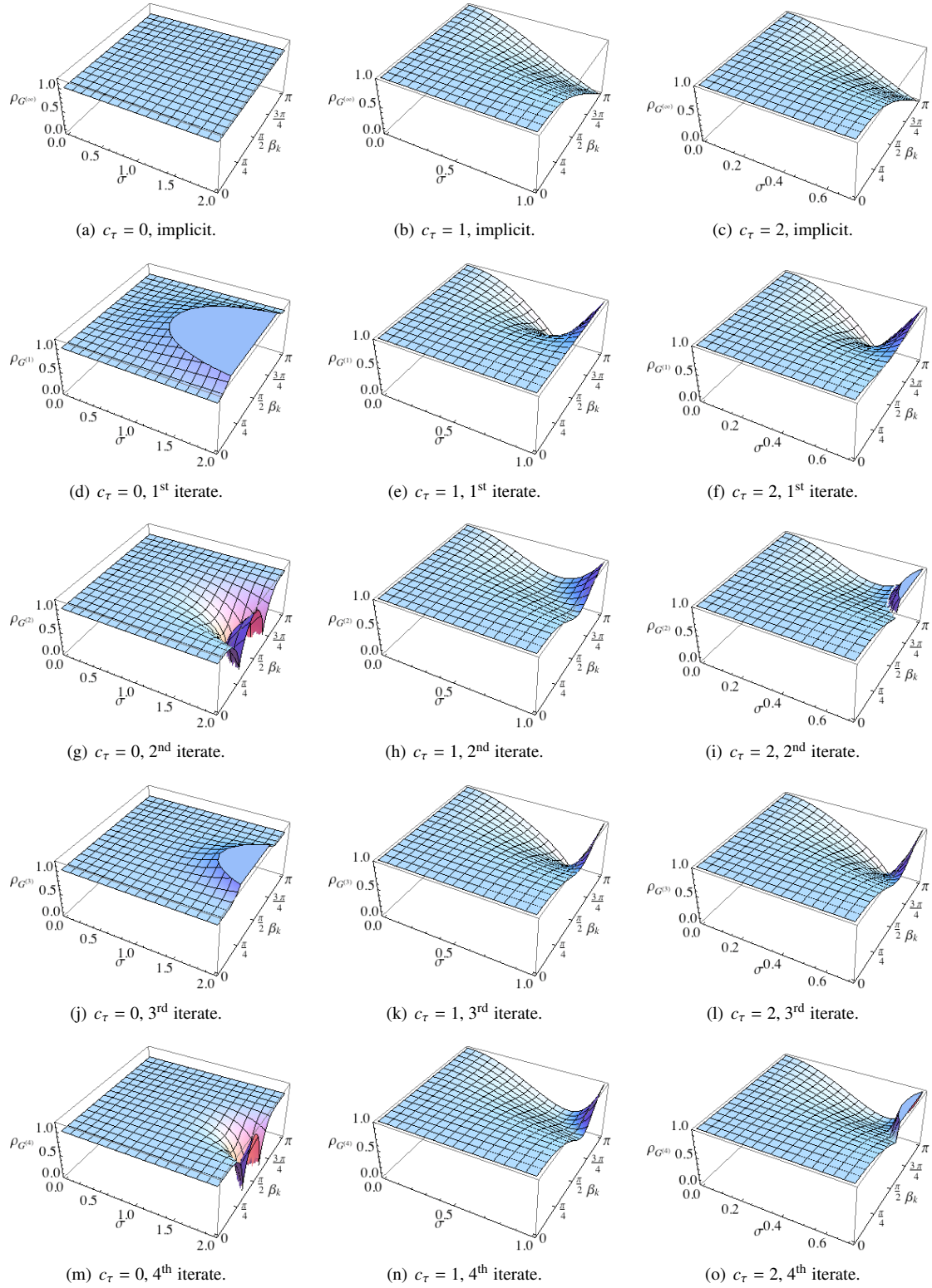


Figure 4: Elevation plots of the spectral radii  $\rho_{G^{(i)}}(\sigma, \beta_k)$ , for  $\kappa = 0$ ,  $c_\tau = 0, 1, 2$ , and various iterates of the predictor/multi-corrector algorithm. In the top row, the implicit mid-point time integrator detailed in (176). In the subsequent rows, the iterates from one to four. For the case  $c_\tau = 0$ ,  $c_\tau = 1$ , and  $c_\tau = 2$ , the plots are in the range  $\sigma \in [0, 2]$ ,  $\sigma \in [0, 1]$ , and  $\sigma \in [0, \sqrt{2}/2]$ , respectively. Also, note that Figures 4(a), 4(d), 4(g), 4(j), 4(m) have a vertical range  $[0, 1.2]$ , while all other Figures are in the range  $[0, 1]$ .



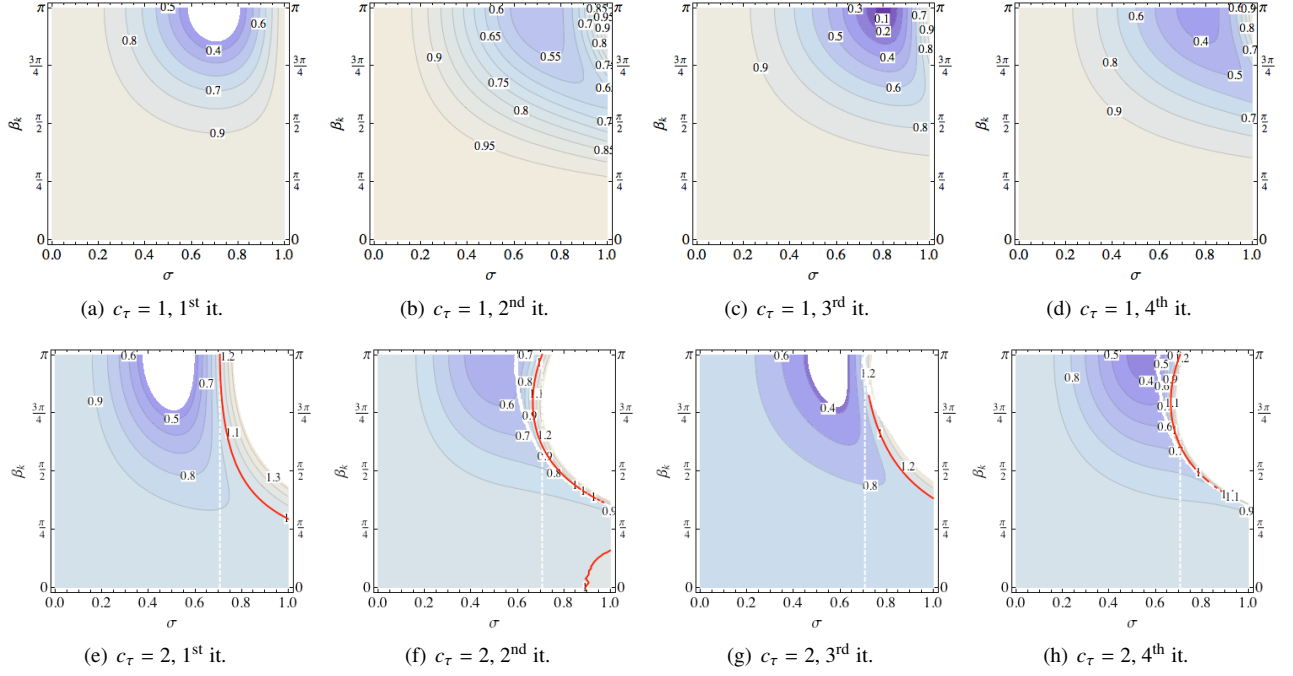


Figure 5: Contour plots of the spectral radii of various iterates of the predictor/multi-corrector algorithm for  $\kappa = 0$ . Figures 5(a)–5(d):  $c_\tau = 1$ . Figures 5(e)–5(h):  $c_\tau = 2$ . The red continuous line is the contour line relative to a unit spectral radius, the white dashed line in Figures 5(e)–5(h) indicates the value  $\sigma = \sqrt{2}/2$ .

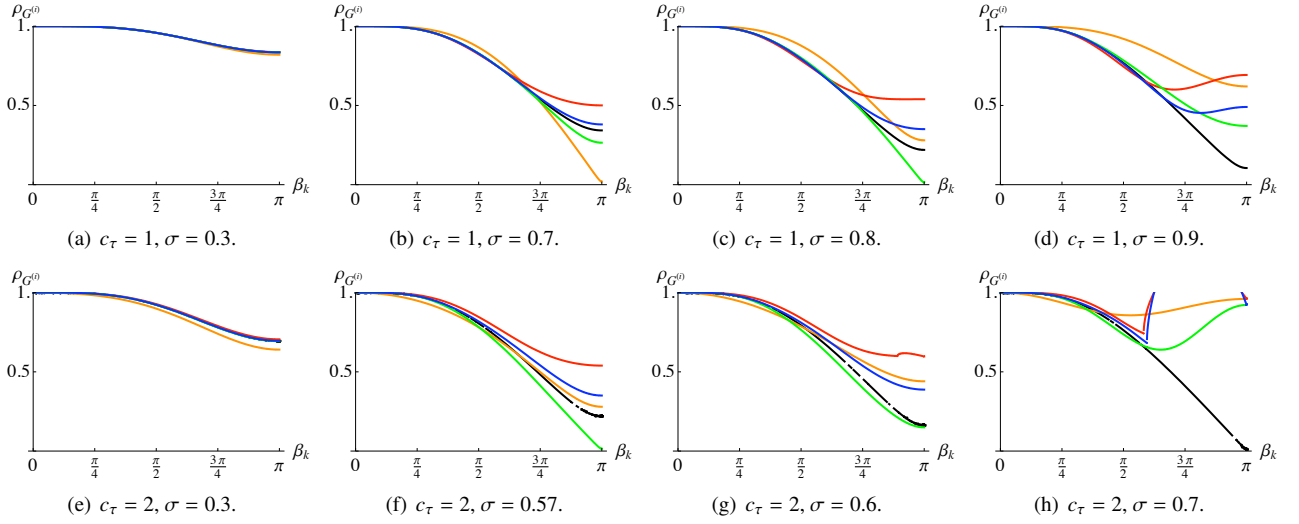


Figure 6: Spectral radii for the stabilized predictor/multi-corrector algorithm in the case  $\kappa = 0$ , for various values of the acoustic Courant number  $\sigma$  and stabilization parameter. Black: Implicit time integrator. Orange, red, green and blue are used for the first, second, third, and fourth iterates, respectively.

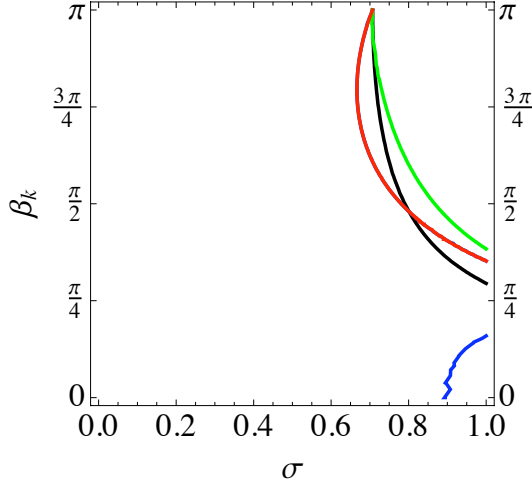


Figure 8: Contours of unit spectral radii (stability limit) for the case  $c_\tau = 2$ . The color scheme is as follows: First iterate in black, second iterate in blue, third iterate in green, fourth iterate in red. Part of the curve relative to the second iterate is not visible, as it overlaps with the one relative to the fourth iterate.

can be characterized in terms of an amplification matrix  $\mathbf{G}^{(i)}$ . In general,  $\mathbf{G}^{(i)}$  is a function of the acoustic Courant number  $\sigma = \frac{c_s \Delta t}{h}$ , the dissipative Courant number  $\kappa = \frac{\nu \Delta t}{h^2}$  and  $\beta_k = \frac{2\pi k}{N}$  (i.e., the angularly normalized wave number  $k$ , such that  $0 \leq \beta_k \leq \pi$ ). Specifically, we have the relation (see again Appendix A)

$$\hat{\mathbf{Z}}_{k,n+1}^{(i)} = \mathbf{G}^{(i)} \hat{\mathbf{Z}}_{k,n}, \quad (175)$$

where  $\hat{\mathbf{Z}}_{k,n}$  represents the velocity/pressure modal pair at the previous time-step. In the limit for an infinite number of iterations, we obtain the amplification matrix for the original implicit mid-point algorithm from which the predictor/corrector time integrator is derived (see, for details, Appendix A):

$$\hat{\mathbf{Z}}_{k,n+1} = \mathbf{G}^{(\infty)} \hat{\mathbf{Z}}_{k,n}. \quad (176)$$

Stability properties are evaluated by analyzing how  $\mathbf{G}^{(i)}$  evolves in time an initial condition. Recalling that in a finite-dimensional space all norms are equivalent, the stability of the numerical discretization is ensured if it is possible to find a vector norm  $\|\cdot\|$  for which

$$\|\mathbf{G}^{(i)}\| = \max_{\mathbf{s} \in \mathbb{R}^2 \setminus \mathbf{0}} \frac{\|\mathbf{G}^{(i)} \mathbf{s}\|}{\|\mathbf{s}\|} \leq 1. \quad (177)$$

This is equivalent to say that the matrix  $\mathbf{G}^{(i)}$  will not amplify an initial condition vector. The spectral radius of  $\mathbf{G}^{(i)}$  is

$$\rho(\mathbf{G}^{(i)}) = \max\{|\lambda(\mathbf{G}^{(i)})|\} \leq \|\mathbf{G}^{(i)}\|, \quad (178)$$

where  $\lambda(\mathbf{G}^{(i)})$  is a (generally complex) eigenvalue of  $\mathbf{G}^{(i)}$ . The spectral radius can be used to derive conditions for stability more manageable than (177). To this purpose, we recall a fundamental theorem of linear algebra:

**Theorem 1** (cf. [24], p. 297). *Let  $\mathbf{A} \in \mathbb{C}^{m \times m}$ , where  $\mathbb{C}$  is the complex field. Given  $\epsilon > 0$ , there exist a matrix norm  $\|\cdot\|$  such that  $\rho(\mathbf{A}) \leq \|\mathbf{A}\| \leq \rho(\mathbf{A}) + \epsilon$ .*

This immediately implies:

$$\rho(\mathbf{G}^{(i)}) < 1 \Rightarrow \|\mathbf{G}^{(i)}\| < 1 \Rightarrow \text{stability}, \quad (179)$$

$$\rho(\mathbf{G}^{(i)}) > 1 \Rightarrow \|\mathbf{G}^{(i)}\| > 1 \Rightarrow \text{instability}. \quad (180)$$

Conditions (179) and (180) can also be interpreted in light of the following theorem:

**Theorem 2** (cf. [24], p. 298). *Let  $\mathbf{A} \in \mathbb{C}^{m \times m}$ , where  $\mathbb{C}$  is the complex field. Then:  $\lim_{n \rightarrow \infty} \mathbf{A}^n = \mathbf{0}$  if and only if  $\rho(\mathbf{A}) < 1$ .*

Hence, if  $\rho(\mathbf{G}^{(i)}) < 1$ , Theorem 2 implies that the solution decays to zero after an infinite number of time steps, while if  $\rho(\mathbf{G}^{(i)}) > 1$ , one can consider, as initial condition vector  $\hat{\mathbf{Z}}_0$ , the eigenvector relative to an eigenvalue  $\lambda_0$  with  $|\lambda_0| > 1$ . Using the properties of vector norms, it is easy to see that  $\lim_{n \rightarrow \infty} \|\hat{\mathbf{Z}}_n\| = \lim_{n \rightarrow \infty} \|(\mathbf{G}^{(i)})^n \hat{\mathbf{Z}}_0\| = \lim_{n \rightarrow \infty} |\lambda_0|^n \|\hat{\mathbf{Z}}_0\| = \infty$ , and we have unbounded growth.

The more delicate situation is when  $\rho(\mathbf{G}^{(i)}) = 1$ , which, in the general case, makes the von Neumann analysis of stability impractical. Particularly, the von Neumann stability analysis cannot be applied to *general* non-normal matrices [37, 61]. An example is the mid-point implicit time integrator for  $c_\tau = 0$  (see Fig. 4(a)). Then  $\rho(\mathbf{G}^{(i)}) = 1$ , for every  $\sigma$  and  $\beta_k$ , and the stability analysis should be approached with energy methods.

However, when  $c_\tau > 0$ , the matrices  $\rho(\mathbf{G}^{(i)})$  generated by the proposed method are treatable, due to their specific structure. In fact, when  $c_\tau > 0$ ,  $\rho(\mathbf{G}^{(i)}) = 1$  occurs only in three specific situations (see, e.g., Figure 4):

1.  $\sigma = 0 \Leftrightarrow \Delta t = 0$ , a trivial case corresponding of no time evolution. In this case, the amplification matrix  $\mathbf{G}^{(i)}$  must be the identity, and  $\|\mathbf{G}^{(i)}\| = 1$ .
2.  $\beta_k = 0$ , corresponding to the evolution in time of a constant mode. In this case, it is trivial to prove that for numerical consistency reasons,  $\mathbf{G}^{(i)}$  must be the identity, with  $\|\mathbf{G}^{(i)}\| = 1$ .
3. The time-step stability limit, which corresponds to the frontier between the regions in which  $\rho(\mathbf{G}^{(i)}) < 1$  and  $\rho(\mathbf{G}^{(i)}) > 1$  (a curve in a two-dimensional space, as depicted in Figures 5 and 8, and a surface in a three-dimensional space, as depicted in Figure 11). Since it is not advisable to run nonlinear computations too close to the boundary of the stability region, this case does not require additional analysis.

## 6.2. Behavior of the highest modes

Stability of the highest modes in a computation is a necessary *but not sufficient* condition for overall stability. However, an understanding of the dynamics of high wave number modes can shed light on the overall behavior of the algorithm, and, most importantly, provide time-step control estimates of practical use in computations. Detailed derivations are presented in Appendix B. Suffices to say that the following estimate of the stable time-step size for the highest wave numbers can be derived:

$$\Delta t \leq \frac{h^2}{\nu + \sqrt{\nu^2 + c_\tau c_s^2 h^2}}. \quad (181)$$

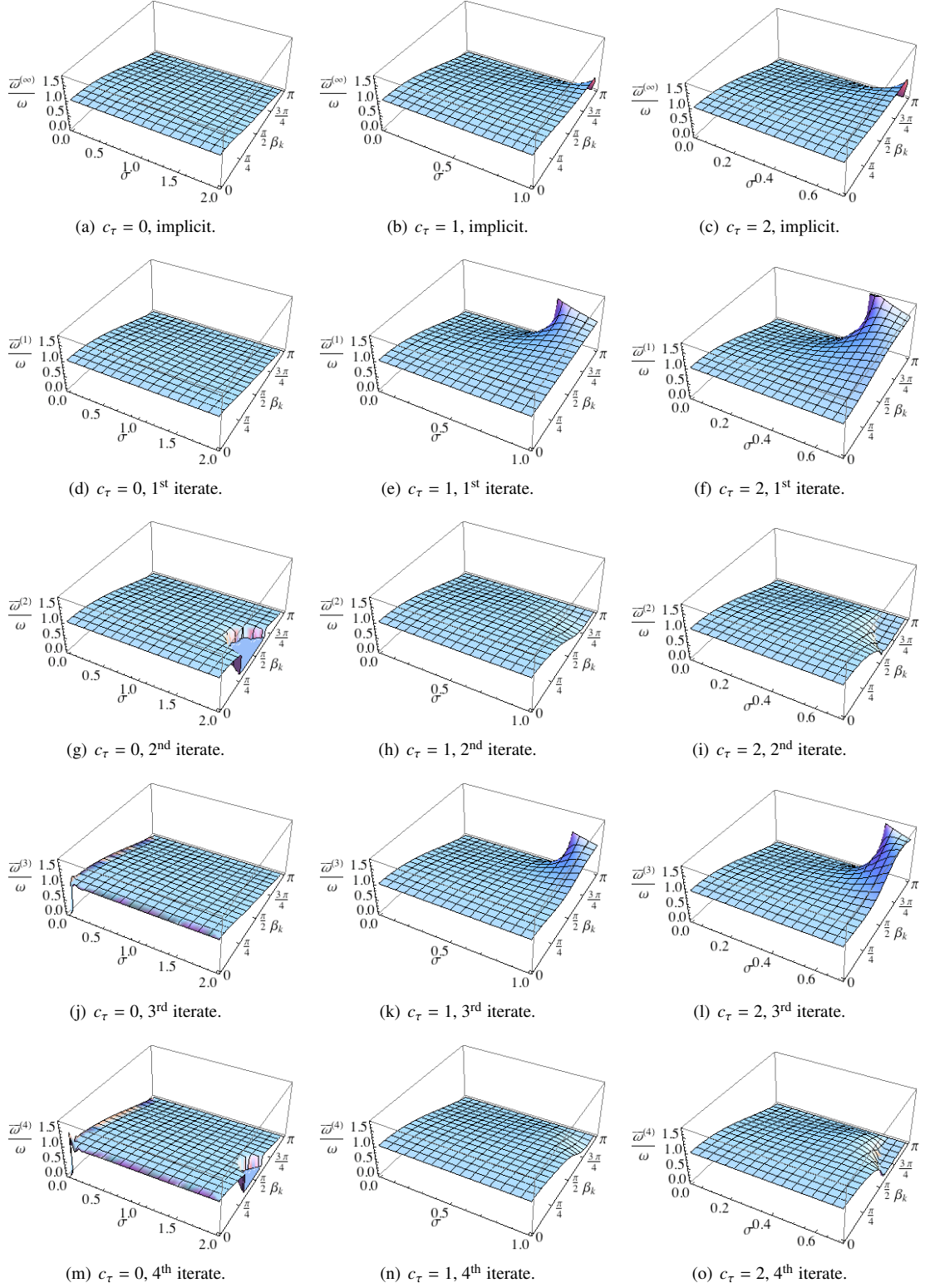


Figure 7: Elevation plots of the ratio  $\bar{\omega}/\omega$ , for  $\kappa = 0$ . Plots are for  $c_\tau = 0, 1, 2$ , and various iterates of the predictor/multi-corrector algorithm. In the top row, the implicit mid-point time integrator (see (176)). In the subsequent rows, the iterates from one to four. Note that for the case  $c_\tau = 0$ ,  $c_\tau = 1$ , and  $c_\tau = 2$ , the plots are in the range  $\sigma \in [0, 2]$ ,  $\sigma \in [0, 1]$ , and  $\sigma \in [0, \sqrt{2}/2]$ , respectively.

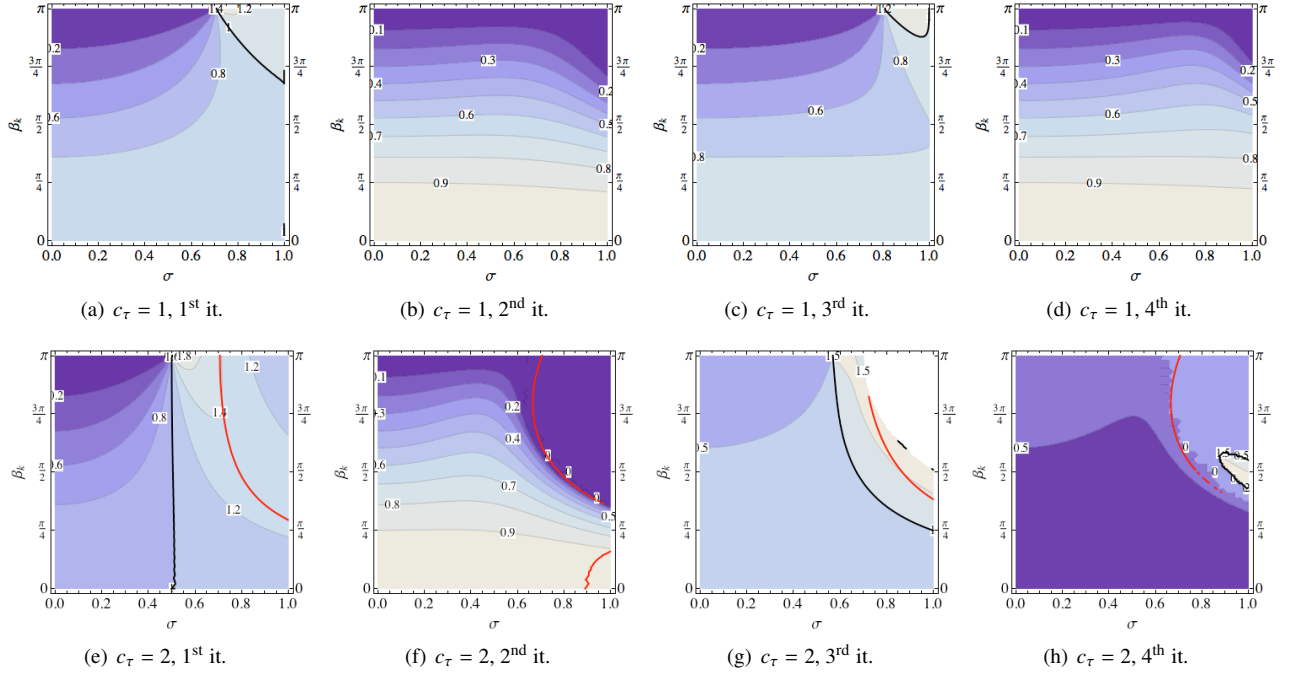


Figure 9: Contour plots of the ratio  $\bar{\omega}/\omega$ , for  $\kappa = 0$ . Plots are for  $c_\tau = 1, 2$ , and various iterates of the predictor/multi-corrector algorithm. Figures 9(a)–9(d):  $c_\tau = 1$ . Figures 9(e)–9(h):  $c_\tau = 2$ . The red continuous line is the locus of a unit spectral radius. The black continuous line indicates the locus  $\bar{\omega}/\omega = 1$  (no phase error).

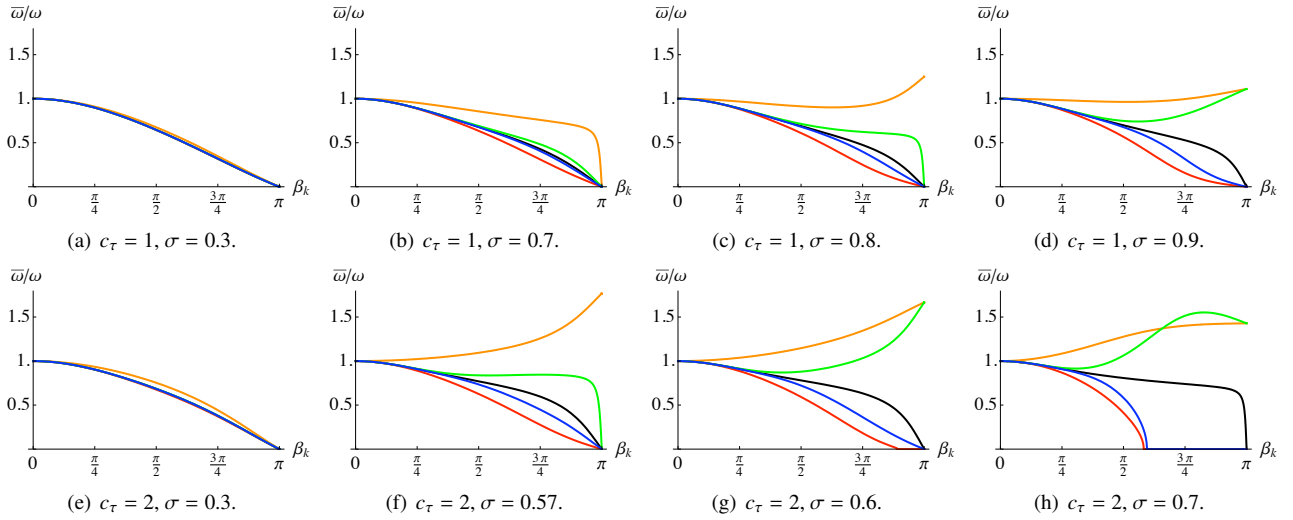


Figure 10: Plot of the ratio  $\bar{\omega}/\omega$ , for  $\kappa = 0$ , for various values of the acoustic Courant number  $\sigma$ . Figures 10(a)–10(d):  $c_\tau = 1$ . Figures 10(e)–10(h):  $c_\tau = 2$ . Color scheme is as follows. Black: Implicit time integrator. Orange, red, green and blue are used for the first, second, third, and fourth iterate, respectively.

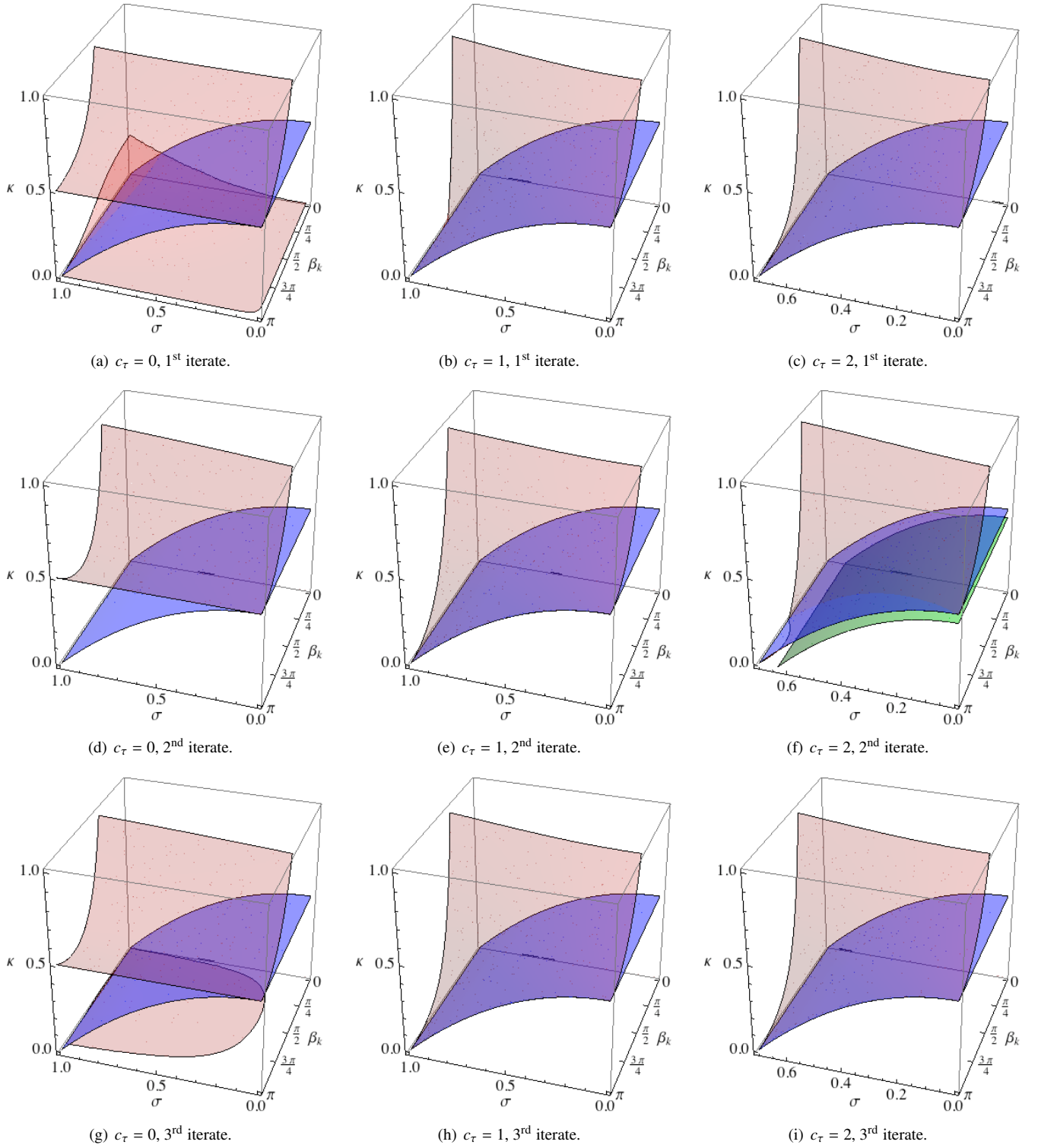


Figure 11: Three-dimensional surfaces representing the loci of the spectral radii equal to unity for the first, second, and third iterate of the proposed time integrator, in the case of no stabilization,  $c_\tau = 0$ , and for values of the stabilization parameter equal to  $c_\tau = 1$  and  $c_\tau = 2$ , respectively. The blue surface represents the stability limit given by (244) (or, equivalently, (181)), the green surface represents the “mitigated” stability condition given in (199). Note that there are no additional intersections between the red and blue surface in Figure 11(b), other than the one that occurs for  $\beta_k = \pi$ . The very rapid change in slope near  $[\sigma, \beta_k] = [1, \pi/2]$  seems to create a graphical artifact, which was not possible to resolve increasing the plotting mesh resolution.

**Remark15.** In the limit of a vanishing artificial viscosity, a modified advective Courant-Friedrichs-Lewy condition is obtained, namely

$$\Delta t \leq \frac{h}{\sqrt{c_\tau} c_s}, \quad \text{or}, \quad \sigma \leq \frac{1}{\sqrt{c_\tau}}. \quad (182)$$

This implies that the variational multiscale stabilization is reducing the stability limit for  $c_\tau > 1$  and increasing the stability limit if  $c_\tau < 1$  (at least for the highest wave numbers). For  $c_\tau = 1$ , the standard acoustic Courant-Friedrichs-Lewy stability condition is recovered.

**Remark16.** In the limit of a vanishing speed of sound, the stability limit is uniquely dependent on the artificial viscosity  $\nu$  and takes the classical form of the dissipative Courant-Friedrichs-Lewy condition:

$$\Delta t \leq \frac{h^2}{2\nu}, \quad \text{or}, \quad \kappa \leq \frac{1}{2}. \quad (183)$$

### 6.3. Accuracy, dissipation, and dispersion

A complex eigenvalue of  $\mathbf{G}^{(i)}$  can be expressed as:

$$\lambda(\mathbf{G}^{(i)}) = |\lambda(\mathbf{G}^{(i)})| e^{i\bar{\omega}\Delta t}, \quad (184)$$

where  $\bar{\omega}\Delta t = \arg(\lambda(\mathbf{G}^{(i)}))$ , and  $\bar{\omega} \in \mathbb{R}$  is the phase. This decomposition is important for the study of the dispersion properties of the proposed time integration approach, as shown in Section 6.4. An alternative expression for (184) is

$$\lambda(\mathbf{G}^{(i)}) = e^{(-\bar{\xi} + i\bar{\omega})\Delta t}, \quad (185)$$

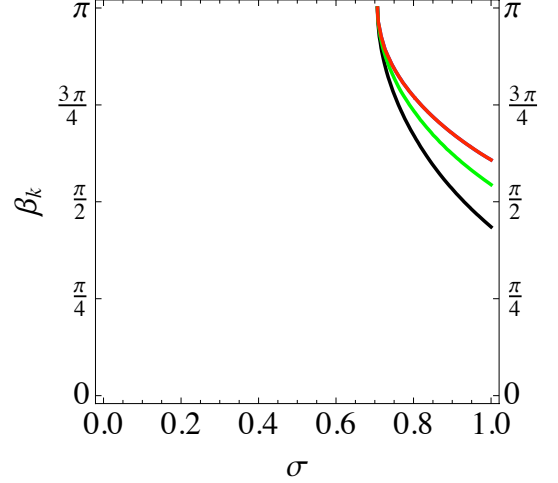
where

$$|\lambda(\mathbf{G}^{(i)})| = e^{-\bar{\xi}\Delta t}, \quad \text{or}, \quad \bar{\xi} = -\frac{\log(|\lambda(\mathbf{G}^{(i)})|)}{\Delta t}. \quad (186)$$

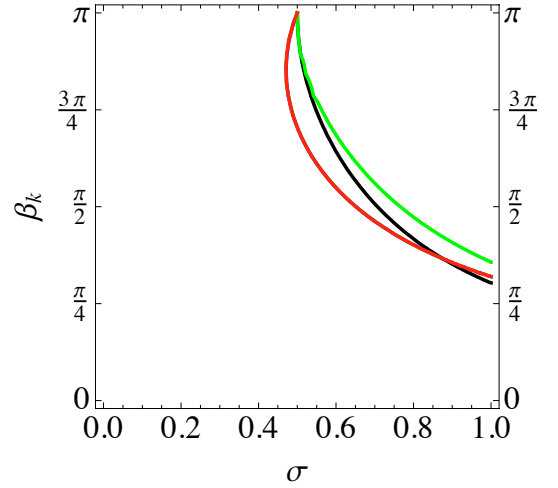
By performing a Taylor expansion of  $\bar{\xi}$  and  $\bar{\omega}$  in the limit of vanishing time step  $\Delta t$  and mesh size  $h$ , it is possible to recover the truncation error and the formal order of accuracy of the various iterates of the method, as shown in Section 6.4.3. Due to the complexity of the algebra involved, we are not including the calculations and explicit expressions of the eigenvalues of the  $\mathbf{G}^{(i)}$  matrices. We present the fundamental results by appropriate plots in Section 6.4 and Section 6.5. All algebraic symbolic manipulations were performed using the MATHEMATICA<sup>®</sup>™ software [1, 67].

### 6.4. The case of vanishing viscosity

In shock hydrodynamics computations, the artificial viscosity is usually present only in shock layers, and is absent in expansion regions. Therefore, it is very important to study the proposed time integrator in the limit of a vanishing viscosity, as most part of the flow domain is subject to this condition.



(a)  $c_\tau = 1$ , all iterates.



(b)  $c_\tau = 2$ , all iterates.

Figure 12: Contour plots of the loci of the spectral radii equal to unity for the case  $\kappa = 1/4$ , with  $c_\tau = 1$  (Fig. 12(a)) and  $c_\tau = 2$  (Fig. 12(b)). The color scheme is as follows. First iterate in black, second iterate in blue, third iterate in green, fourth iterate in red. The curves relative to the second iterate are not visible as they overlap with the ones relative to the fourth iterate.

#### 6.4.1. Amplification factor

Figure 4 shows the spectral radii of the matrices  $\mathbf{G}^{(i)}$  for  $i \rightarrow \infty$  (implicit scheme) and  $i = 1, 2, 3, 4$ , with stabilization parameter  $c_\tau = 0, 1, 2$ . First, note that the implicit algorithm detailed in (176) is neutrally stable in the case of no stabilization, fact that can be derived using classical energy arguments (note that the spectral radius of the amplification matrix is equal to unity over the entire plane  $[\sigma, \beta]$  (Fig. 4(a))). Without stabilization, only the *even* iterates are stable in the predictor/multi-corrector version, as detailed in Figures 4(g) and 4(m). As shown in Figures 4(d) and 4(j) (note in particular that these vertical range of the plot is  $[0, 1.2]$ ), when stabilization is absent, the first and third iterates of the proposed algorithm are *unconditionally unstable*. This somewhat surprising phenomenon can be explained by realizing that the spectral radii for the predictor/multi-corrector scheme exhibit a *non-*



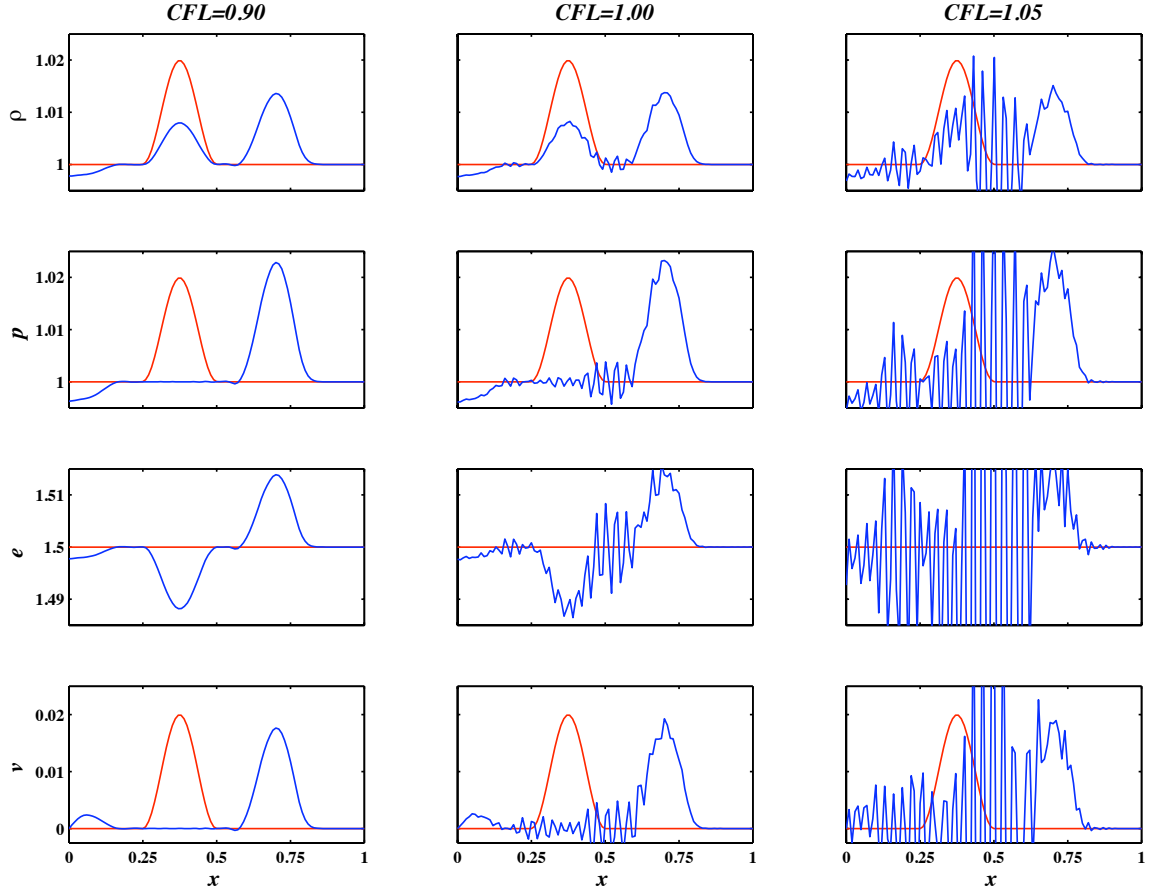


Figure 13: Plots of density, pressure, internal energy, and velocity versus the spatial position for the propagation of an acoustic pulse at time  $t = 0.5$ , and various CFL numbers. Two iterations of the conservative predictor/multi-corrector approach. The red lines indicate the initial condition.

*monotonic* convergence to unity as  $(i) \rightarrow \infty$ .

The implicit case in Fig. 4(b) is stable, and the stability range for the predictor/multi-corrector is  $\sigma \in [0, 1]$  for  $c_\tau = 1$  (Fig. 4(e), 4(h), 4(k), and 4(n)), as predicted in Section 6.1. As seen in Figure 8 for the case  $c_\tau = 2$ , the stability region of some of the iterates does not completely extend to  $\sigma = 1/\sqrt{2}$  (i.e., the stability limit for the highest wave numbers, derived in Section 6.1). This feature is the result of the increased value of the stabilization constant, which causes some of the lower modes to go unstable before the highest. Observe that, in this case, the range of stability is a function of the number of iterations of the predictor/multi-corrector. In fact, the first and third iterates (Figs. 5(e) and 5(g)) are stable over the entire range  $\sigma \in [0, 1/\sqrt{2}]$ . Referring to Figure 8, it is easy to realize a safety factor 0.9 is sufficient in recovering a stability range for all iterates, namely  $\sigma \in [0, 0.9/\sqrt{2}]$ . Additional information can be gained by plotting sections of the spectral radius elevation plots of the various amplification matrices for different values of the acoustic Courant number  $\sigma$ , as shown in Figure 6. Figures 6(a)–6(d) show the results for  $c_\tau = 1$ , Figures 6(e)–6(h) show results for  $c_\tau = 2$ .

Observe that high wave number damping increases as the

value of  $c_\tau$  increases. The convergence of the spectral radii of the iterates (color lines) to the spectral radii of the corresponding implicit schemes (black lines) is easily appreciated. In Figure 6(g), the onset of a bifurcation point for the amplification matrix of the second iterate is visible (the kink in the red curve near  $\beta_k = 7\pi/8$ ). This phenomenon is more clearly visible in Figure 6(h), a section of the spectral radii *past* the stability limit  $0.9/\sqrt{2} \approx 0.64$ , for the second and fourth iterates (the red and blue curves in proximity of  $\beta_k = 5\pi/8$ ). Past a bifurcation point, the eigenvalues of the corresponding amplification matrix cease to be complex conjugate, as evident in Figures 10(g) and 10(h), by the absence of a phase in the eigenvalues. This is not a desirable property in discretized wave propagation problems which should behave as systems of harmonic oscillators. The best numerical results in terms of accuracy and robustness (low mesh distortion) were obtained with three iterates of the algorithm,  $c_\tau = 2$  and a safety factor 0.8 (i.e.,  $\sigma = 0.8/\sqrt{2} \approx 0.57$ ). This choices correspond to the green curve in Figure 6(f): The high wave number damping, the moderate low wave number error, and the absence of an eigenvalue bifurcation explain these findings.

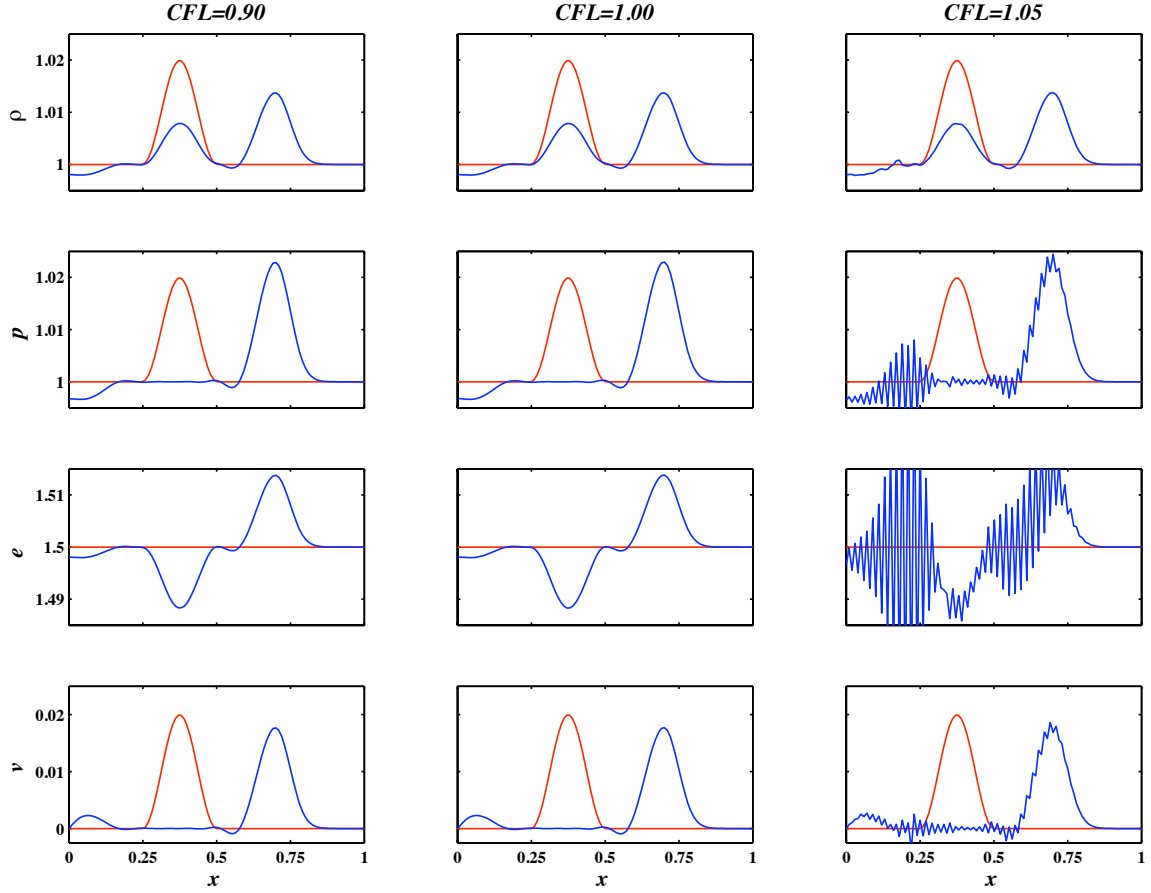


Figure 14: Plots of density, pressure, internal energy, and velocity versus the spatial position for the propagation of an acoustic pulse at time  $t = 0.5$ , and various CFL numbers. Three iterations of the conservative predictor/multi-corrector approach. The red lines indicate the initial condition.

#### 6.4.2. Dispersion error

When no viscosity is present, it is very insightful to evaluate the extent of the dispersion error in computations. For this purpose, observe that the classical dispersion relationship for a linear wave is given by  $\omega = 2\pi k c_s / |\mathbb{T}|$ . Recalling that  $|\mathbb{T}| = hN$  is the measure of the periodic one-dimensional domain, it is easily derived

$$\omega \Delta t = \sigma \beta_k. \quad (187)$$

A typical measure of the dispersion error is given by the ratio

$$\frac{\bar{\omega}}{\omega} = \frac{\arg(\lambda(\sigma, \beta_k))}{\sigma \beta_k}. \quad (188)$$

When  $\bar{\omega}/\omega = 1$ , no dispersion error is present for a certain wave number  $\beta_k$  at a certain value of  $\sigma$ . Figure 7 shows elevation plots of the ratio  $\bar{\omega}/\omega$ . It is noticeable in Figures 7(g) and 7(m) that eigenvalue bifurcation takes place for values of  $[\sigma, \beta_k] \approx [2, \pi/2]$ , when no stabilization is applied. Although less notably, this also occurs for the case  $c_\tau = 2$  (Figs. 7(i), and 7(o)), for  $[\sigma, \beta_k]$  near  $[1, \pi/2]$ , as already mentioned in Section 6.4.1. Contour plots of the dispersion ratio are presented in Figure 9. The black thick lines indicate the loci where the

dispersion ratio equals unity. The red thick lines indicate the locus of the amplification factor equal to unity (i.e., the stability limit). Note that the predictor/multi-corrector iterates show degradation of the phase error in proximity of the stability limits, with respect to the corresponding implicit algorithms (see also Fig. 7). The noticeable “distortion” in the contour lines near the stability boundary indicates a significant growth in the phase errors. However, the third iterate for the stabilized case for  $c_\tau = 1$  and  $c_\tau = 2$  shows fairly moderate phase error for  $\sigma \in [0.8, 0.9]$  and  $\sigma = 0.57$ , respectively, as seen in Figure 10.

**Remark17.** Computations using  $c_\tau = 2$  were most often performed at  $\sigma = 0.8/\sqrt{c_\tau} \approx 0.57$  with three iterates of the predictor/multi-corrector. This choice corresponds to high wave number damping and small overall phase error (see also Fig. 6(f)), and was found to reduce mesh distortion in blast tests of Sedov type [58].

**Remark18.** The fact that the variational multiscale stabilization with  $c_\tau = 2$  reduces by a factor  $1/\sqrt{2}$  the stability limit should not be considered as an indication that the variational multiscale shock hydrodynamics method would require 30% more time steps than a standard hydrocode computation. In



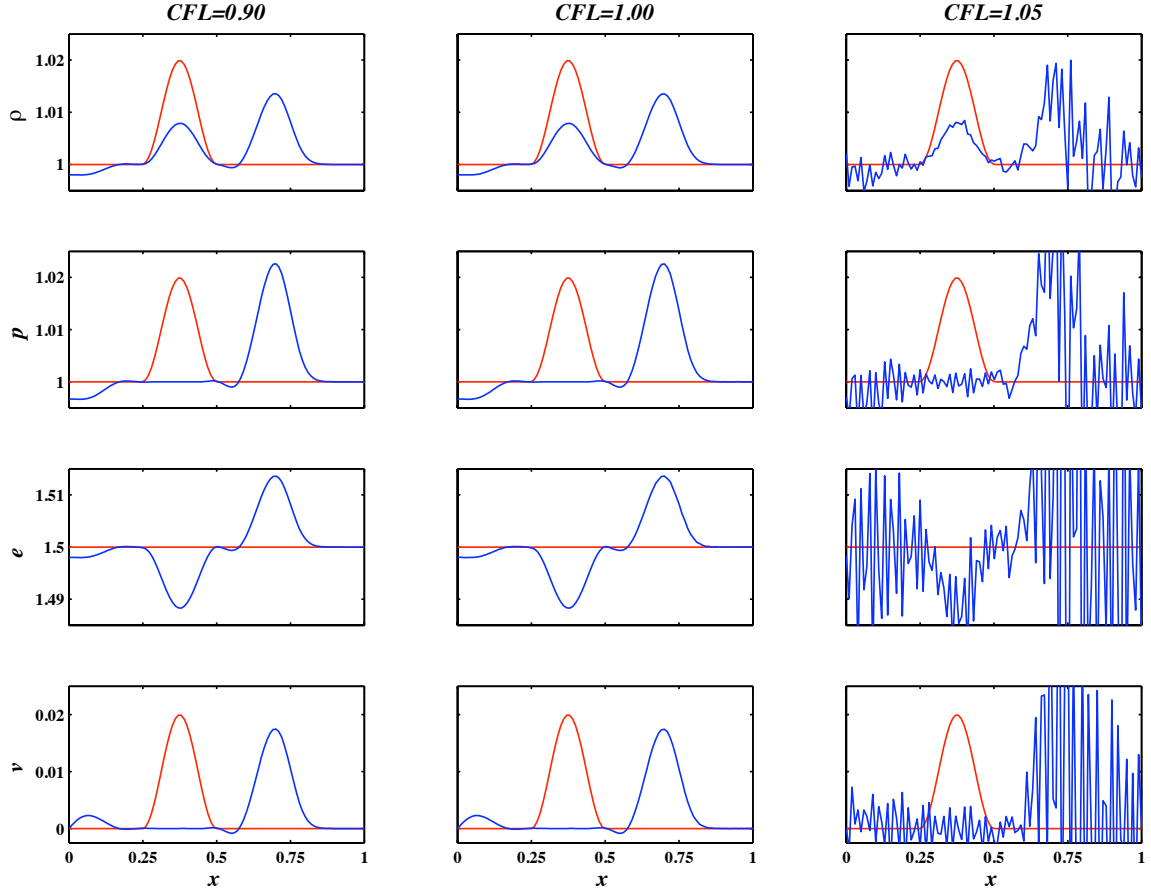


Figure 15: Plots of density, pressure, internal energy, and velocity versus the spatial position for the propagation of an acoustic pulse at time  $t = 0.5$ , and various  $CFL$  numbers. Four iterations of the conservative predictor/multi-corrector approach. The red lines indicate the initial condition.

fact, the opposite can be said: A comparison on multidimensional tests showed that the variational multiscale method required on average 20-30% fewer time steps than the more standard constant pressure finite element implementation in [56]. This is due to the fact that the proposed approach provides considerable reduction in mesh distortion with respect to a standard hydrocode implementation, with very positive effects also on the overall time advancement constraint.

Figures 7 and 9 show the noticeable difference in behavior between the odd and even iterates of the method. Restricting our analysis to the stabilized case, we see that odd iterates overshoot the frequency  $\omega$  for high values of  $\beta_k$  and  $\sigma$ , while even iterates undershoot the frequency in the same range of values for  $\beta_k$  and  $\sigma$ . This is most clearly appreciated in Figure 10.

#### 6.4.3. Low wave number limit and truncation error

A Taylor series expansion of  $\bar{\xi}$  and  $\bar{\omega}$  in powers of the time step  $\Delta t$  and mesh spacing  $h$  can be used to estimate the order of

accuracy of the method. When  $c_\tau = 1$  we obtain

$$\bar{\xi}(\mathbf{G}_{c_\tau=1}^{(1)}) = \frac{c_s^2 \tilde{k}^4}{8} h^2 \Delta t - \frac{c_s^4 \tilde{k}^4}{8} \Delta t^3 + O(h^4 \Delta t, \Delta t^3 h^2), \quad (189)$$

$$\bar{\xi}(\mathbf{G}_{c_\tau=1}^{(2,3,4,\dots,\infty)}) = \frac{c_s^2 \tilde{k}^4}{8} h^2 \Delta t + O(\Delta t h^4, \Delta t^3 h^2), \quad (190)$$

and

$$\bar{\omega}(\mathbf{G}_{c_\tau=1}^{(1)}) = \omega - \frac{c_s \tilde{k}^3}{6} h^2 + \frac{c_s^3 \tilde{k}^3}{6} \Delta t^2 + O(\Delta t^4, \Delta t^2 h^2, h^4), \quad (191)$$

$$\bar{\omega}(\mathbf{G}_{c_\tau=1}^{(2,3,4,\dots,\infty)}) = \omega - \frac{c_s \tilde{k}^3}{6} h^2 - \frac{c_s^3 \tilde{k}^3}{12} \Delta t^2 + O(\Delta t^4, \Delta t^2 h^2, h^4), \quad (192)$$

where  $\tilde{k} = 2\pi k / |\mathbb{T}|$ , so that  $\omega = \tilde{k} c_s$ . We conclude that the formal order of accuracy of all the iterates of the method is third order with regard to dissipation and second order with regard to dispersion, when  $\Delta t$  and  $h$  are balanced by a  $CFL$  condition. In

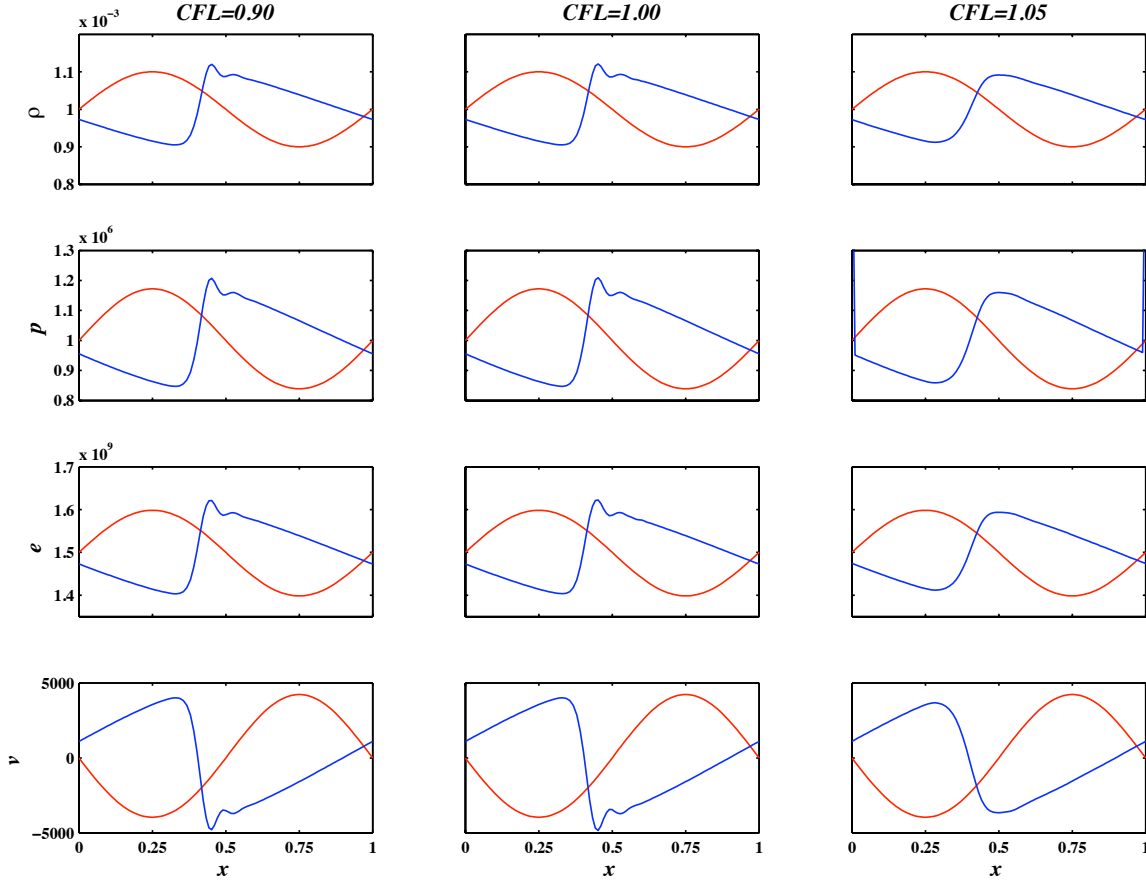


Figure 16: Plots of density, pressure, internal energy, and velocity versus the spatial position for the periodic breaking wave test at time  $t = 0.0004$ , and various  $CFL$  numbers. Three iterations of the conservative predictor/multi-corrector approach. The red lines indicate the initial condition.

the case  $c_\tau = 2$ , we obtain

$$\bar{\xi}(\mathbf{G}_{c_\tau=2}^{(1)}) = \frac{c_s^2 \tilde{k}^2}{4} \Delta t + O(h^2 \Delta t, \Delta t^3), \quad (193)$$

$$\begin{aligned} \bar{\xi}(\mathbf{G}_{c_\tau=2}^{(2)}) &= \frac{c_s^2 \tilde{k}^4}{4} h^2 \Delta t - \frac{5c_s^2 \tilde{k}^4}{16} \Delta t^3 \\ &\quad + O(\Delta t h^4, \Delta t^3 h^2), \end{aligned} \quad (194)$$

$$\bar{\xi}(\mathbf{G}_{c_\tau=2}^{(3,4,\dots,\infty)}) = \frac{c_s^2 \tilde{k}^4}{4} h^2 \Delta t + O(\Delta t h^4, \Delta t^3 h^2), \quad (195)$$

as well as

$$\begin{aligned} \bar{\omega}(\mathbf{G}_{c_\tau=2}^{(1)}) &= \omega - \frac{c_s \tilde{k}^3}{6} h^2 + \frac{61c_s^3 \tilde{k}^3}{96} \Delta t^2 \\ &\quad + O(\Delta t^4, \Delta t^2 h^2, h^4), \end{aligned} \quad (196)$$

and

$$\begin{aligned} \bar{\omega}(\mathbf{G}_{c_\tau=2}^{(2,3,4,\dots,\infty)}) &= \omega - \frac{c_s \tilde{k}^3}{6} h^2 - \frac{c_s^3 \tilde{k}^3}{12} \Delta t^2 \\ &\quad + O(\Delta t^4, \Delta t^2 h^2, h^4). \end{aligned} \quad (197)$$

Under the assumption that the time step  $\Delta t$  and mesh spacing  $h$  are balanced by a  $CFL$  condition, the previous derivations

imply that the dissipation error is first order for the first iterate and third order for all other iterates, while the dispersion error is second order for all iterates. Overall, the proposed stabilized method is formally second-order accurate, for two or more iterations of the predictor/multi-corrector procedure. Also note, for  $c_\tau = 2$ , the presence of an additional term in  $\Delta t^3$  in equation (194), relative to the second iterate, with respect to (195), relative to higher iterates. This indicates that at least three iterations are required to exactly retain the properties of the implicit limit algorithm in the low wave number regime.

### 6.5. The case of non-vanishing viscosity

Artificial viscosity operators are usually added in shock hydrodynamics computations to enhance robustness under severe shock wave conditions. Viscosity operators usually are modeled as Laplace diffusive operators, and may pose additional constraints on stability, further limiting the time step. It is therefore important to present a thorough analysis and time-step control estimate, when dissipation is present. In this case, because of the parabolic nature of the problem, the dispersion error analysis is less relevant and will be omitted.

Recalling that by definition and the developments in Section 6.1,  $0 \leq \sigma \leq 1/\sqrt{c_\tau}$ , and  $0 \leq \kappa \leq 1/2$ , a rearrangement of (244)

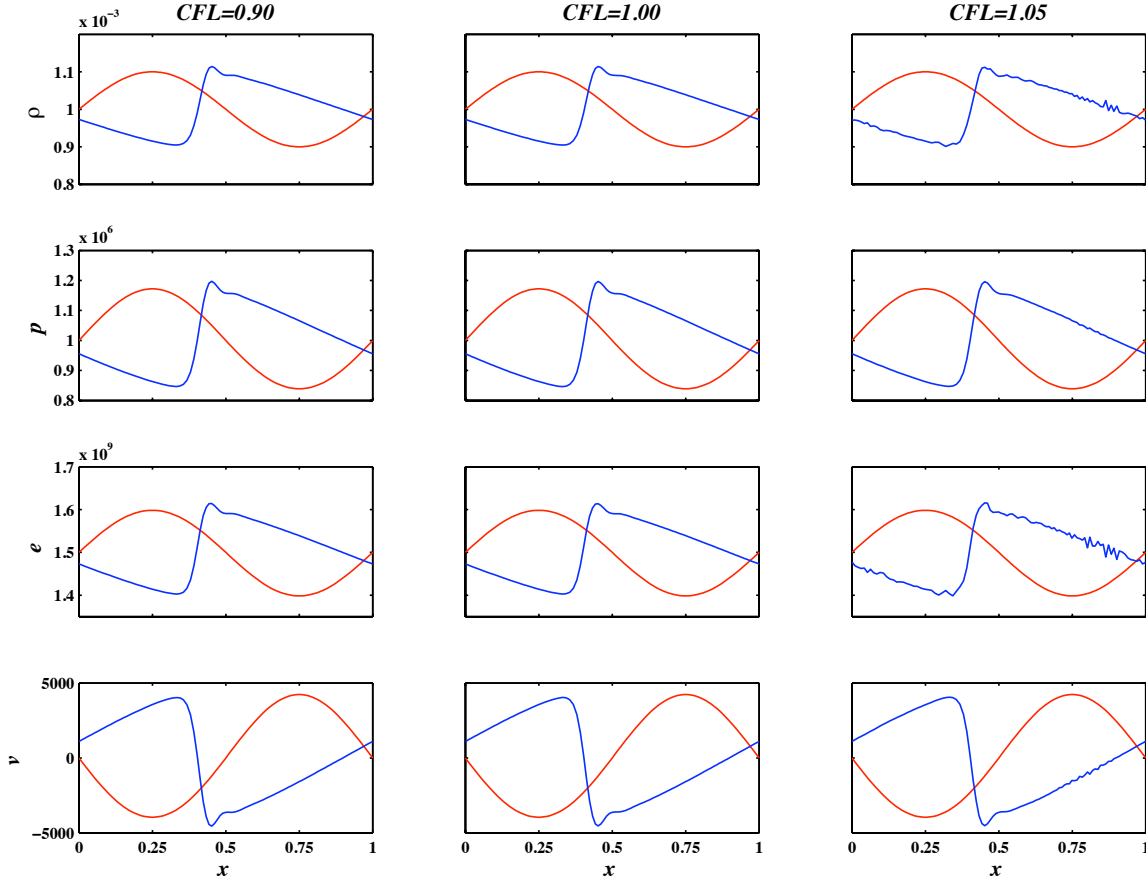


Figure 17: Plots of density, pressure, internal energy, and velocity versus the spatial position for the periodic breaking wave test at time  $t = 0.0004$ , and various  $CFL$  numbers. Four iterations of the conservative predictor/multi-corrector approach. The red lines indicate the initial condition.

yields the stability condition:

$$\sigma \leq \sqrt{\frac{1 - 2\kappa}{c_\tau}}, \quad (198)$$

from which, when  $\kappa = 1/4$ , we obtain  $\sigma \leq \sqrt{2}/2$  and  $\sigma \leq 1/2$  for the cases  $c_\tau = 1$  and  $c_\tau = 2$ , respectively. These results can also be verified in Figure 12, for  $\beta_k = \pi$ .

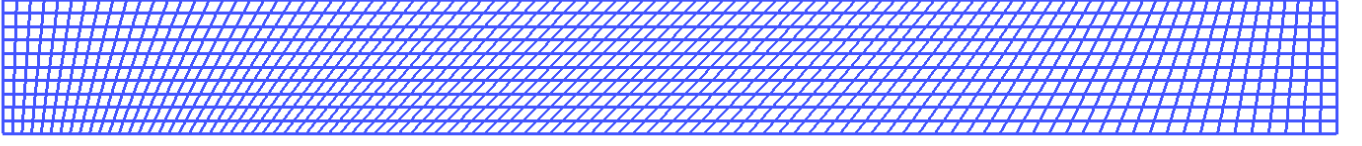
Perhaps the most important plots of the entire section are presented in Figure 11, in which red three-dimensional contour surfaces show the loci of the spectral radii equal to unity for the first, second, and third iterate of the proposed method, in the space  $[\sigma, \beta_k, \kappa]$ . Results are shown in the case of no stabilization ( $c_\tau = 0$ ) and for values of the stabilization parameter  $c_\tau = 1$  and  $c_\tau = 2$ . A blue surface represents the stability limit given by the high wave number analysis result (244) when equality holds. In addition, in Figure 11(f), a green surface is used to represent the condition,

$$1 = \frac{0.9}{\kappa + \sqrt{\kappa + c_\tau \sigma^2}}, \quad (199)$$

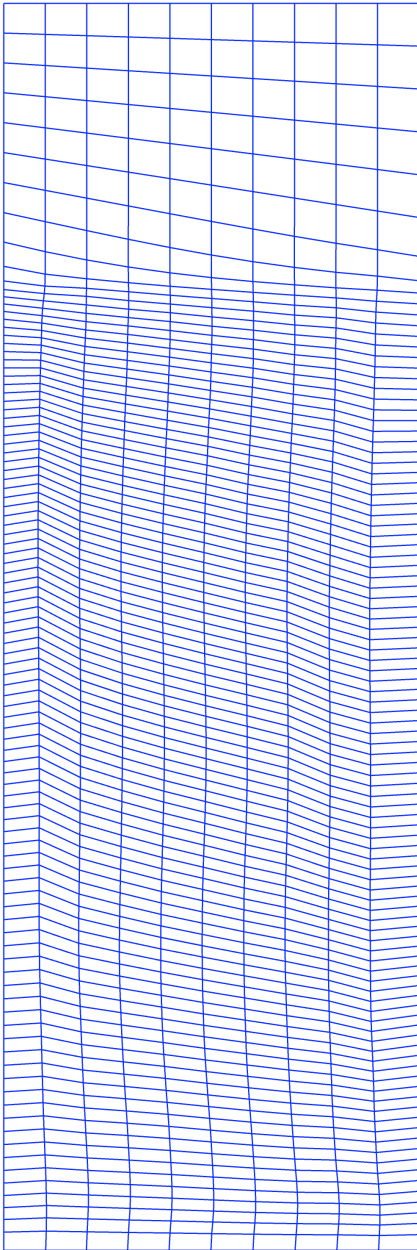
which incorporates a safety factor  $CFL = 0.9$  in the time-step stability condition (181). First of all, note that the three-dimensional stability region in Figures 11(a) and 11(g) is

bounded by the two red surfaces. The third iterate with no stabilization is unconditionally unstable, since the intersection between planes  $[\kappa = \text{const.}]$  and red surfaces always occurs in Figure 11(g). This is not the case for the first iterate, which is conditionally stable in the range  $\kappa \in [1/4, 1/2]$ . However, this result does not have practical relevance, since in the nonlinear case one can expect  $\kappa$  to cover the entire range  $[0, 1/2]$ .

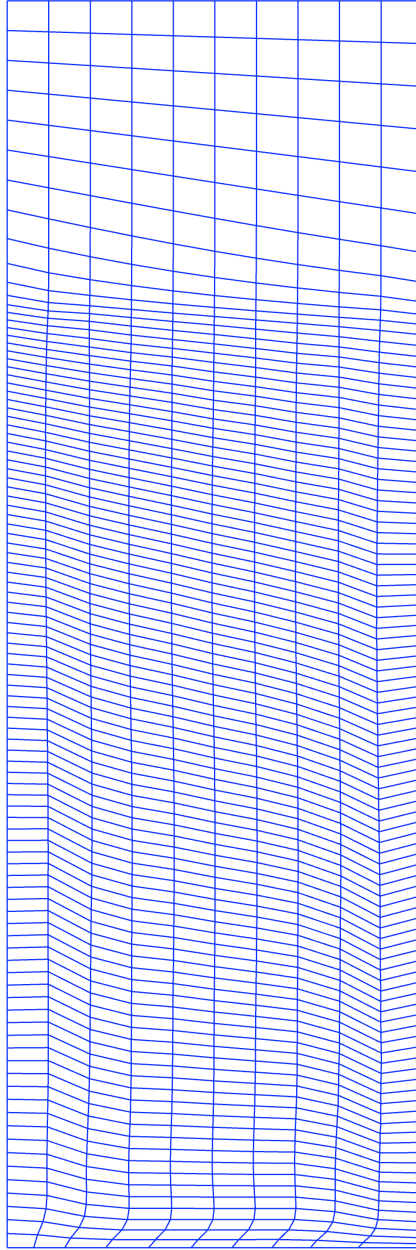
Considering Figure 11(f) for the two-iterate scheme with  $c_\tau = 2$ , it is easy to realize that the red and blue surfaces do intersect at values  $\beta_k < \pi$ , indicating that the stability condition (181) is inappropriate. Mitigating the size of the time step by a factor 0.9 (see (199)) is sufficient in preventing the predictor-corrector from becoming unstable, as indicated by the fact that (at least by visual inspection) the red and green surfaces in the same picture do not intersect. When  $c_\tau = 1$ , the estimate given by (181) (or, equivalently, (244)), yields a stable time step, at least by inspection of Figures 11(b), 11(e), and 11(h).



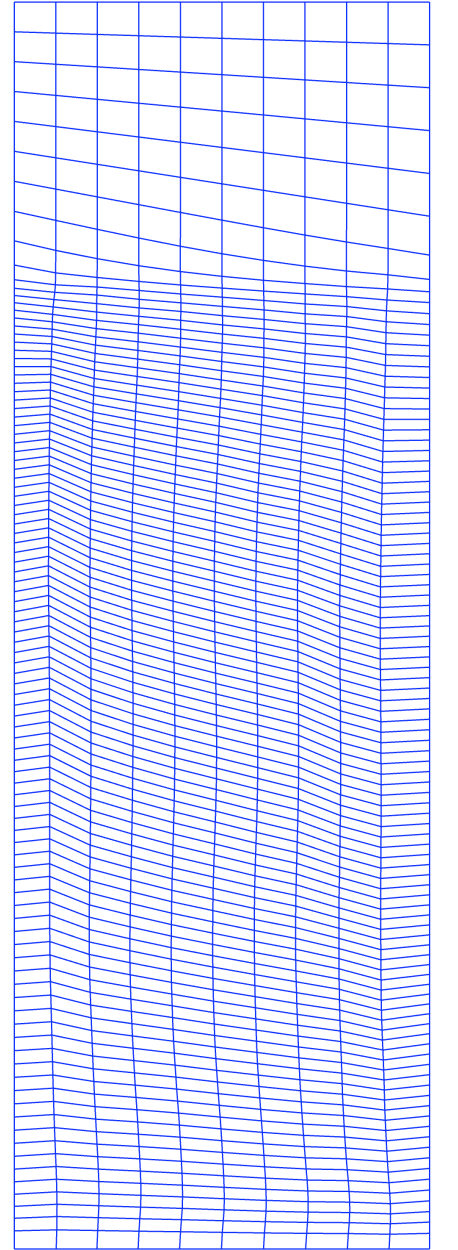
(a) Initial mesh.



(b) VMS-P0 [55, 56].



(c) VMS-C.



(d) VMS-AC [52, 53].

Figure 18: Saltzman test. Comparison of the mesh displacement results for the VMS-P0, VMS-C, VMS-AC methods. The meshes in Figures 18(b), 18(c), 18(d) are rotated by 90 degrees counter-clockwise.

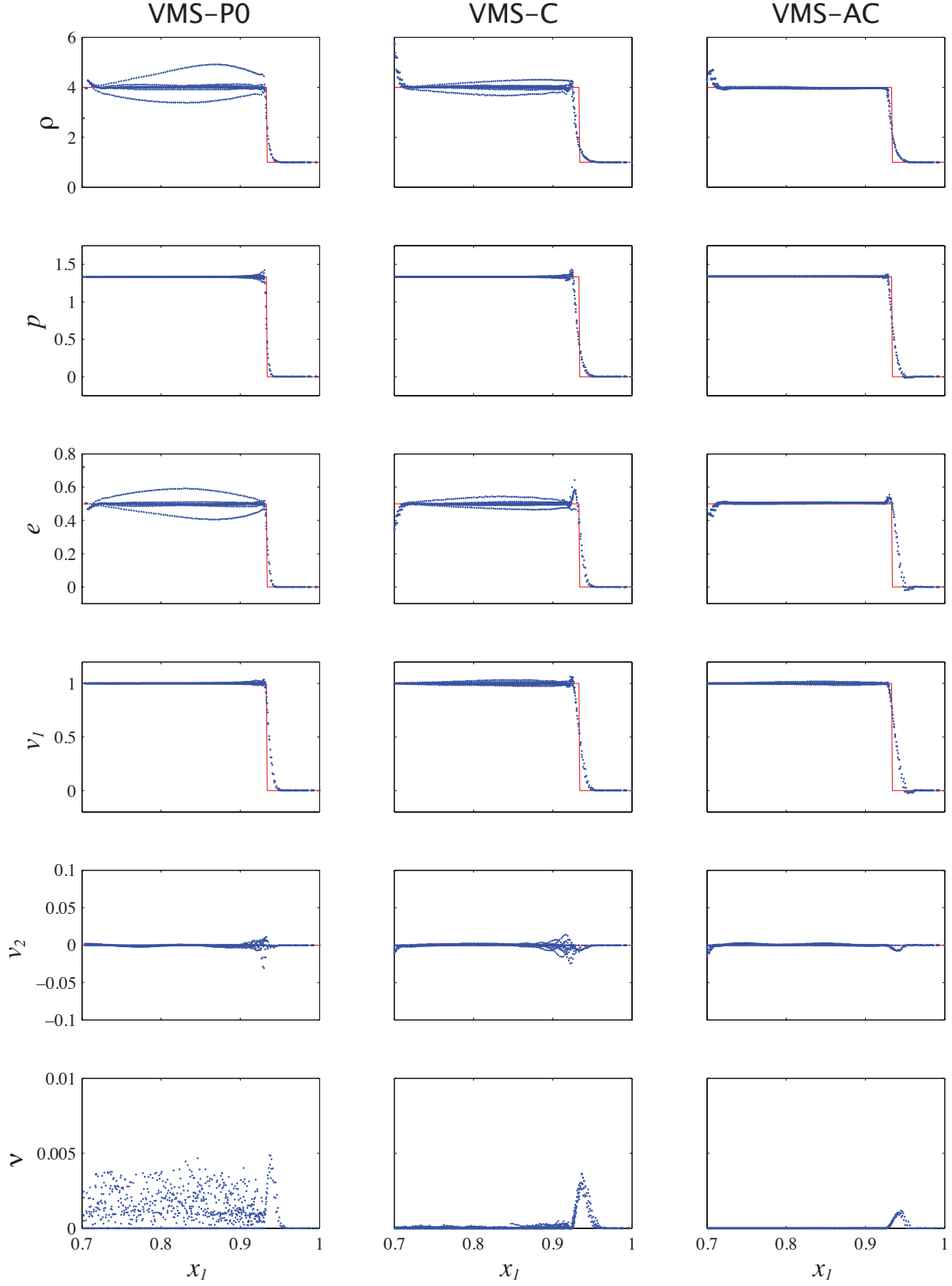


Figure 19: Saltzman test, comparison against the exact solution (in red). Left column: VMS-P0 method. Center column: VMS-C method. Right column: VMS-AC method. From the top row down: Density, pressure, internal energy, horizontal velocity  $v_1$ , vertical velocity  $v_2$ , and artificial viscosities. The solution is plotted as a function of the coordinate  $x_1$ . The exact solution is represented by the continuous line, the dots represent *the entire set of nodal values* of the numerical solution (projected along the  $x_2$ -coordinate onto a single plane).

The computations with the nonlinear algorithm were run with the following time-step control:

$$\Delta t = CFL \min_{1 \leq e \leq n_{el}} \left\{ \frac{h_e^2}{v_{art_e} + \sqrt{v_{art_e}^2 + c_\tau c_{s_e}^2 h_e^2}} \right\}. \quad (200)$$

where  $v_{art_e} = \max\{v_{art;y}, v_{art;p}\}$ . The specific bound for the safety factor  $CFL$  depends on the number of iterations: For one and three iterations stability is achieved if  $CFL < 1.0$ , and for two and four iterations stability is achieved if  $CFL < 0.9$ .

In the case when the artificial viscosity vanishes and  $c_\tau = 1.0$ , one recovers the classical condition

$$\Delta t \leq CFL \min_{1 \leq e \leq n_{el}} \left\{ \frac{h_e}{c_{s_e}} \right\}. \quad (201)$$

Conversely, in the case of a very low temperature fluid with artificial viscosity active, one recovers the CFL condition for the purely diffusive case, namely:

$$\Delta t \leq CFL \min_{1 \leq e \leq n_{el}} \left\{ \frac{h_e^2}{2v_{art_e}} \right\}. \quad (202)$$

This situation is often encountered in hypervelocity impact or piston problems (i.e., the Saltzman test in Section 7.3), in which the internal energy rises from a very low initial value as a result of the conversion of boundary work into kinetic energy.

## 7. Numerical tests

Unless otherwise stated, all computations presented in this article are run with three iterations of the predictor multi-corrector time integrator,  $c_\tau = 2$ , and  $CFL = 0.8$ , which corresponds to a very favorable condition in the linearized case, with high wave number dissipation, high accuracy in the low wave number range, and low dispersion error throughout the entire wave number spectrum (see Section 6 for a detailed justification of these claims).

The quality, accuracy and robustness of the proposed method is evaluated by comparing it to two previously developed variational multiscale methods [53, 56], and other state of the art computations [2, 42]. In particular the following notation is used to denoting the various algorithms:

**VMS-C** indicates the *variational multiscale conservative* method, that is the conservative, updated Lagrangian approach to shock hydrodynamics proposed in this study.

**VMS-AC** indicates the *variational multiscale asymptotically conservative* method, proposed in [52, 53]. This method is formulated in the pure Lagrangian framework and adopts an iterative predictor-corrector approach which is conservative only when convergence of the iterations is attained.

**VMS-P0** indicates the *variational multiscale Q1/P0* method, proposed in [55, 56]. This method is conservative, but maintains the typical structure of a standard hydrocode, in that all thermodynamic variables are approximated as piece-wise constant functions over the elements of the computational mesh.

### 7.1. Propagation of an acoustic pulse

This one-dimensional test is performed to check the sharpness and robustness of the time-step estimate provided by the von Neumann analysis, when the artificial viscosity operator is not active. This particular test tracks the propagation of an acoustic pulse represented by the initial conditions

$$v_0 = \omega, \quad (203)$$

$$\rho_0 = 1 + \omega, \quad (204)$$

$$p_0 = 1 + \omega, \quad (205)$$

$$\omega(X) = \begin{cases} \frac{1 - \cos\left(\frac{2\pi(X-X_0)}{\lambda}\right)}{100}, & 0 \leq X - X_0 \leq \lambda, \\ 0, & \text{otherwise,} \end{cases} \quad (206)$$

where  $\lambda$ , the wavelength is taken equal to one fourth of the length the domain  $\Omega_0$ , and  $X_0 = -\lambda$ . The initial condition is depicted in Figures 13, 14, and 15, by red continuous lines. This test was already presented in [53, 55, 56] in full detail. In practice, the initial condition is given by a base flow with a superposed perturbation with amplitude of about 2%. We can therefore expect the nonlinear equations of Lagrangian shock hydrodynamics to behave very similarly to their linearized limit. As time progresses three waves are generated:

1. A large amplitude acoustic wave moving from left to right, which can be seen on the right of the domain.
2. A smaller amplitude acoustic wave moving from right to left, which at the final time of the computation is about to reflect from the left boundary.
3. A standing (i.e., motionless) entropy wave, characterized by a fluctuation in density and internal energy, visible on the left of the domain.

The numerical results are presented in Figures 13, 14, and 15, in the case of two, three, and four iterations of the predictor/multi-corrector algorithm, and for values of the  $CFL$  number equal to 0.90, 1, and 1.05. It is easy to realize that in the case of two and three iterations (Figs. 13 and 14, resp.) the time-step estimate is very sharp. In fact, in the two-iteration case of Figure 13, solutions are stable for  $CFL = 0.9$  and unstable for  $CFL = 1.0$ . In the three-iteration case of Figure 14, solutions are stable up to  $CFL = 1.0$ , and become unstable for  $CFL = 1.05$ . The case of four iterations (Fig. 15) is more interesting, since it shares the same theoretical stability bound as the two iterate case, namely  $CFL = 0.9$ , but oscillations appear only for  $CFL = 1.05$ . A possible explanation is that the growth of instabilities at the stability limit is slower when four iterates are applied.

### 7.2. Periodic Breaking Wave

Another interesting numerical test for evaluating the temporal stability of the numerical scheme is represented by a periodic, nonlinear breaking wave problem similar to the one described in [17, 18]. The domain of the problem is the interval  $[0, 1]$ , subdivided into 100 elements, and with periodic boundary conditions. The material is a  $\gamma$ -law ideal gas [47] with  $\gamma = 5/3$ . The initial density has a sinusoidal variation

$$\rho(x, 0) = 0.001 (1.0 + 0.1 \sin(2\pi x)).$$



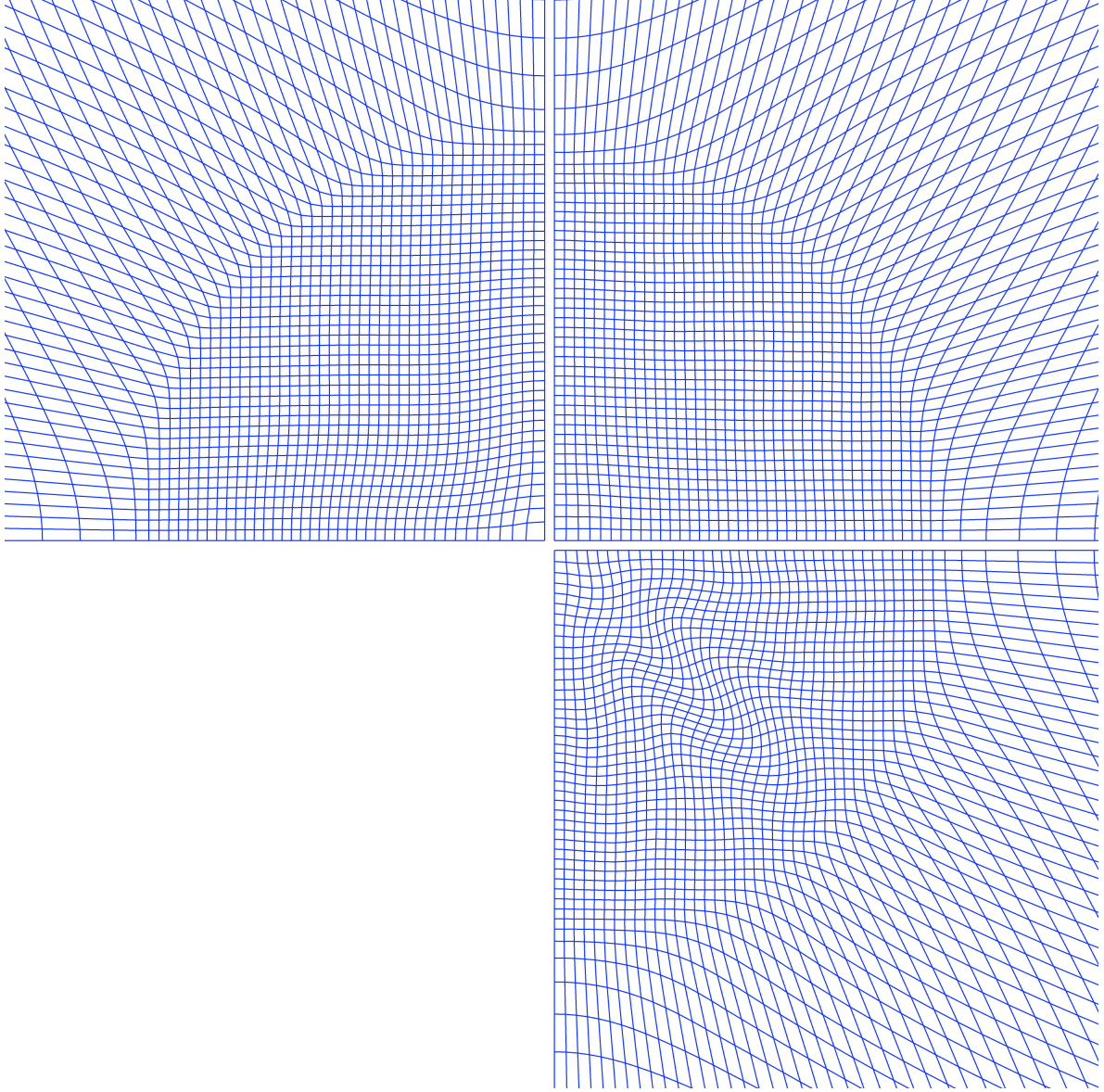


Figure 20: Two-dimensional Noh test, mesh deformation. Comparison between the VMS-P0 method (upper left corner), the VMS-C method (upper right corner), and the VMS-AC method (lower right corner).

The initial pressure is

$$p(x, 0) = 10^6 \left( \frac{\rho(x, 0)}{0.001} \right)^\gamma,$$

and the initial velocity is

$$v(x, 0) = 2 \frac{c_{s_0} - c_s}{\gamma - 1},$$

where

$$c_s = \left( \gamma \frac{p(x, 0)}{\rho(x, 0)} \right)^{1/2},$$

and

$$c_{s_0} = \left( \gamma \frac{10^6}{0.001} \right)^{1/2}.$$

The solution is smooth for a finite time  $0 < T_{\text{break}} < \infty$ , at which point the wave breaks and a shock forms [17, 18]. The numerical results are presented for  $t = 0.0004 > T_{\text{break}}$ . Because this problem involves the formation of shock waves, the artificial viscosity operators are active, and the applicability of the linearized analysis developed in previous sections is tested more severely. As already hinted in Section 6, in the case of nonlinear problems, the predictor/multi-corrector approach is equivalent to a fixed-point *nonlinear* iteration. It was observed in numerical computations that two iterations were not sufficient to ensure robustness of the solution for this test. Only results for three and four iterations are presented, in Figures 16 and 17, respectively. A reason for the need of at least three iterations may be the interplay between the artificial viscosity and the variational multiscale stabilization at the shock location.

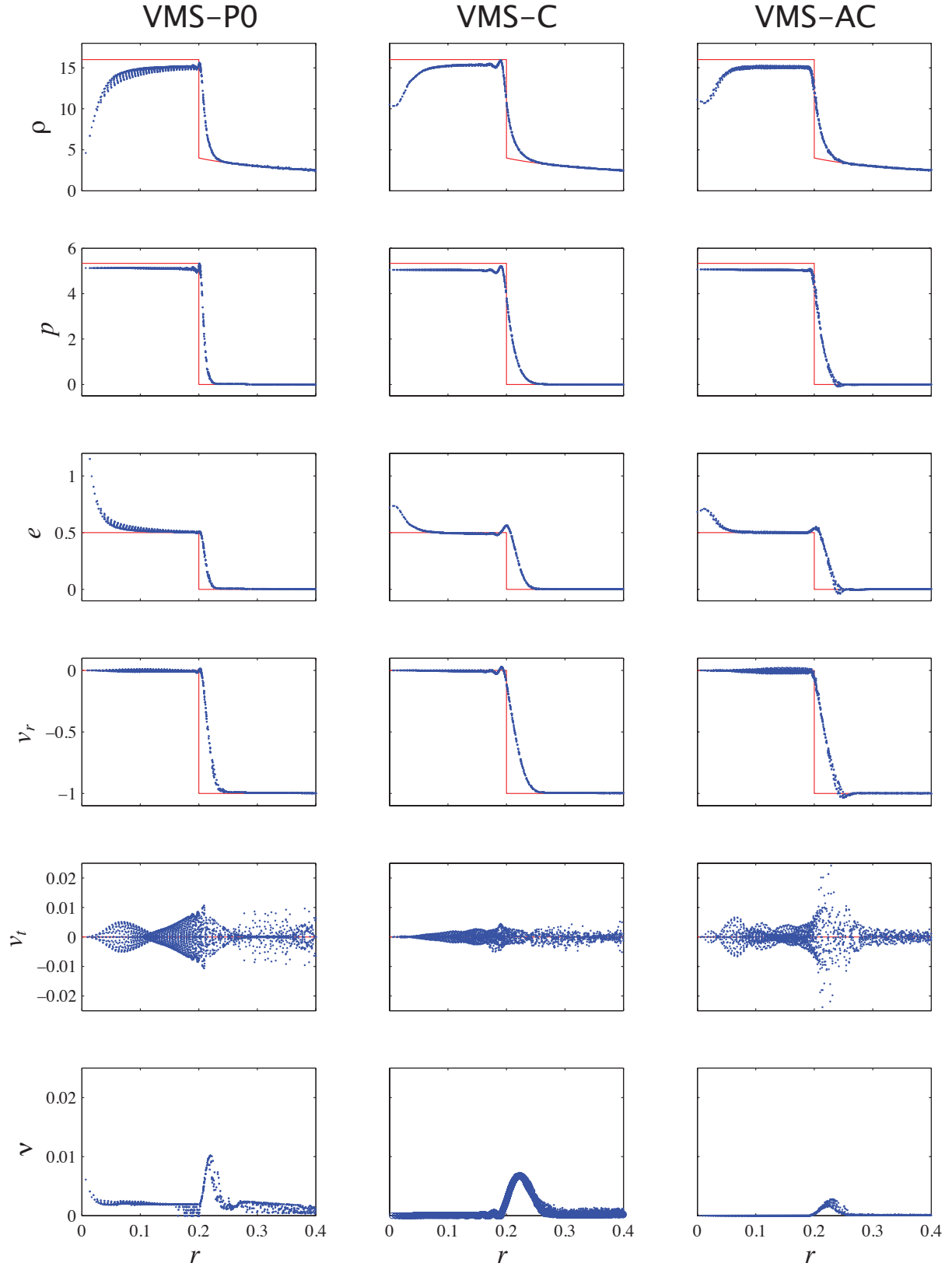


Figure 21: Two-dimensional Noh test on a Cartesian mesh: Comparison with the exact solution (in red). Left column: VMS-P0 method. Center column: VMS-C method. Right column: VMS-AC method. From the top row down: Density, pressure, internal energy, radial velocity  $v_r$ , tangential velocity  $v_t$ , and artificial viscosities. Each variable is plotted as a function of the radius  $r = \sqrt{x_1^2 + x_2^2}$ . All solution points are rotated around the origin to align on a single radial plane.



In particular, the artificial viscosity produces an “artificial” residual near the shock, which in turn increases the strength of the stabilization term. This nonlinear interaction may require more than two iterations to be captured with sufficient accuracy. In the case of three and four iterations (Fig. 16 and Fig. 17, resp.), oscillations are only visible for  $CFL = 1.05$ . This proves the effectiveness of the time-step estimate in the nonlinear case. It is also noticeable that the overshoot past the shock is reduced in the case of four iteration, with respect to the three iteration case. In the case of four iterates, instabilities should occur past  $CFL = 0.90$ , but they are not visible in the case  $CFL = 1.00$ , as in the acoustic pulse test.

**Remark19.** In the case of the periodic breaking wave test, the artificial viscosity is active and may provide a stabilizing effect by damping small oscillations in the compression region, which eventually coalesces into a shock. This fact may partially explain the results in the case of four iterates of the predictor/multi-corrector. In any case, the important point to be made is that the theoretical stability bound developed with a linearized analysis provides a safe estimate for time-step advancement also in the nonlinear case.

### 7.3. Saltzmann test

The Saltzmann test evaluates the ability of a numerical method to capture the features of a planar shock passing through a distorted mesh (see the initial mesh geometry in Fig. 18(a)). A rectangular domain of gas ( $\gamma = 5/3$ ,  $\rho_0 = 1$ ) is initially at rest, at zero temperature (i. e., for practical purposes,  $\epsilon_0 = 10^{-14}$ ). At time  $t_0^+$ , the left boundary is set in motion with unit velocity, and generates a compression shock of infinite strength (infinite Mach number), propagating from left to right through the computational domain. All other boundary conditions are of “roller” type (zero normal velocity/displacement). Given a value of the ideal gas isentropic constant  $\gamma = 5/3$ , the thermodynamic state past the shock is given by values of pressure, internal energy, and density of  $4/3$ ,  $1/2$ ,  $4$ , respectively.

Computations are performed at  $CFL = 0.8$ , and compared at the final non-dimensional time  $T = 0.7$ . Figures (Figs. 18(b), 18(c), 18(d)) show the mesh displacement results, where it can be observed that the mesh deformation pattern of VMS-C is somewhat intermediate between VMS-AC and VMS-P0. Similar conclusions are obtained by observing Figure 19, where the three methods (blue dots) are compared against the exact solution (red continuous line). The new conservative VMS-C method does not produce any negative undershoots in pressure and energy, clearly manifest for the VMS-AC method.

This is considered by the authors a considerable robustness improvement, especially for applications to more realistic materials for which equations of state are given in tabular rather than analytic form.

The VMS-AC method shows very good agreement with the plateaus of the exact solution for density and internal energy, while the VMS-P0 solution shows wide overshoots/undershoots near the lateral boundaries (the horizontal boundaries in Fig. 18(a)) of the computational domain. The VMS-C method has

less pronounced overshoots near the horizontal boundaries, although the overshoot in the internal energy plot past the shock location is more pronounced than in both the VMS-P0 and VMS-AC results.

Note that the VMS-P0 method utilizes a form of the artificial viscosity which also includes a term scaling with the speed of sound, while the artificial viscosities for the VMS-C and VMS-AC methods are purely based on the solution gradient. This is the reason for the different behavior of the artificial viscosity past the shock front, in the last row of plots in Figure 19.

It is important to analyze the typical numerical challenges involved in the Saltzmann test. The numerical error in the shock region is responsible for a spurious component of the velocity, transverse to the shock front normal. At the horizontal boundaries, the roller boundary conditions force the transverse velocity to be zero, and are responsible for an increase in the kinetic energy error in the neighboring area. The numerical error on the kinetic energy is compensated by the numerical error in the internal energy, as the total energy is globally conserved (in a certain sense, “two wrongs make a right”), and the lumped mass matrix does not allow information to be redistributed globally over the mesh. In order to explain the behavior of the various methods under consideration, a number of additional tests, not reported here for the sake of brevity, showed the following trends: The combination of mass lumping and strict enforcement of conservation seems responsible for the over/under-shoots near the boundary for the VMS-P0 and VMS-C methods. This phenomenon is somewhat expected as the lumping procedure, beneficial in the computation of shock discontinuities, effectively *localizes* the solution information. When lumping is used, the numerical forces and work associated to a particular degree-of-freedom cannot have their effect redistributed over neighboring nodes by the inversion of a diagonal lumped mass matrix, as opposed to the case of the consistent mass matrix. Instead, when the consistent mass matrix was used, the VMS-C method showed improved results near the horizontal boundaries, but produced negative undershoots of the internal energy ahead of the shock front. For this reason, this choice is not endorsed by the authors as viable.

### 7.4. Two-dimensional Noh test on a Cartesian quadrant

The Noh test [49] is an implosion test. The velocity has an initial uniform radial distribution (the velocity field points to the origin, and has unit magnitude, except at the origin, where it is forced to zero). The initial internal energy should be zero, but for practical purposes the value  $10^{-14}$  is used. The gas constant  $\gamma = 5/3$  is applied to all computations, and the initial density is set to a constant unit value. The shock speed is  $1/3$ , so that at the final time of  $0.6$  in the computation, the discontinuity is found at  $r = 0.2$ . The exact solution for the density is given by a constant value  $16.0$  past the shock, and by  $1 + t/r$  in front of the shock, where  $t$  is time and  $r = \sqrt{x_1^2 + x_2^2}$  is the radius. The values of pressure and internal energy past the shock are  $16/3$  and  $1/2$ , respectively. The initial domain of a Cartesian quadrant  $[0, 1] \times [0, 1]$  is subdivided into  $50 \times 50$  squares.

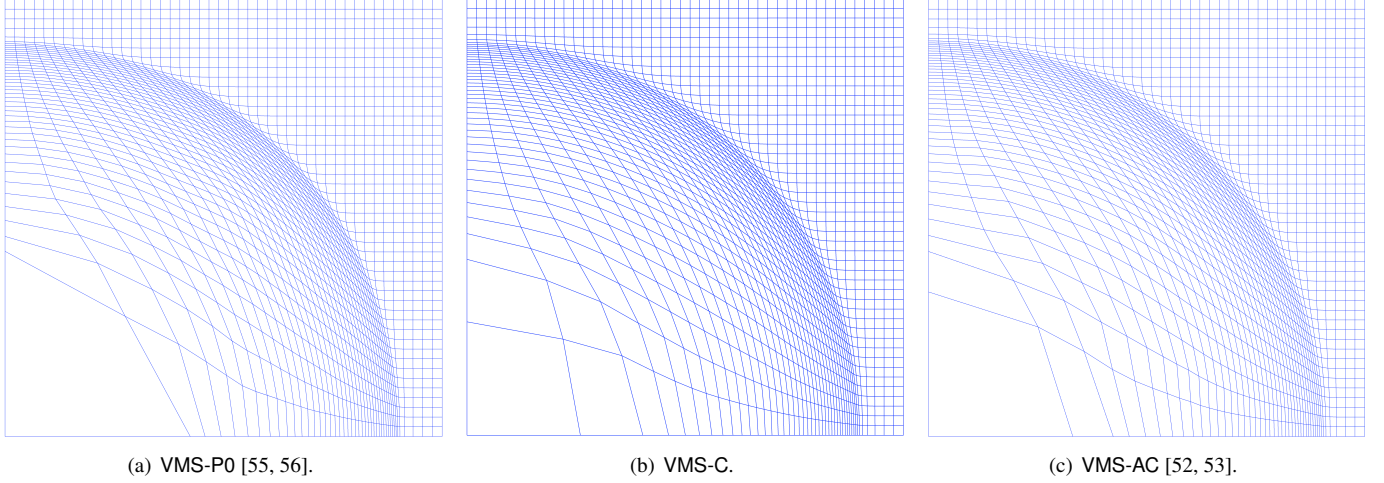


Figure 22: Two-dimensional Sedov test on a Cartesian mesh: Comparison of mesh deformation patterns.

The mesh deformation results presented in Figure 20 show that the best mesh deformation (in terms of regularity of the elements and smoothness of the mesh lines) is achieved with the VMS-C method. Overheating near the implosion corner produce element of larger area (i. e., lower density) in the case of the VMS-P0 method.

The VMS-P0 and VMS-C methods show less mesh distortion because both use a similar definition of the element mesh length in the artificial viscosity, less prone to large variations in direction from element to element than the VMS-AC method. Figure 21 shows a comparison against the exact solution. The density and internal energy plots for the VMS-P0 method are affected by a pronounced overheating error near the origin (for a full description of numerical overheating errors, see [49]). These errors are much reduced in the case of the VMS-AC and VMS-C methods, due to the specific form of the discontinuity capturing operator adopted. Again, the thermodynamic variables computed with the VMS-C method are all positive, while the VMS-AC method produces negative undershoots in internal energy and pressure. With respect to the VMS-P0 solution, the VMS-C solution presents an internal energy overshoot past the shock, but has lower transverse velocity error. In general, the numerical solutions computed with the three methods are in good agreement with the exact solution, considering the coarseness of the mesh (for extensive studies on this problem, see, e.g., [49]). In the case of the density plot, the VMS-P0 method presents a more pronounced angular dispersion of the numerical data with respect to the VMS-C method, also confirmed in the tangential velocity plots.

In general, the VMS-P0 method yields sharper shock profiles than the VMS-C method, at the expense of higher transverse/tangential velocity errors, and a more pronounced dispersion of the data around the exact, symmetric solution.

### 7.5. Two-dimensional Sedov test on a Cartesian quadrant

The Sedov test is a multi-dimensional blast test. An exact solution, which possesses cylindrical symmetry, is derived with self-similarity arguments in [58]. The proposed version of the

Sedov blast test is performed on the  $[0, 1.1] \times [0, 1.1]$  quadrant, subdivided into  $45^2$  initially identical squares, and assesses the ability of the method to respect the cylindrical symmetry.

The initial density has a uniform unit distribution,  $\gamma = 1.4$ , and the internal energy is “zero” (actually,  $10^{-14}$ ) everywhere, except the first square zone on the bottom left corner of the quadrant, near the origin, where it takes the value,  $0.9792/(4h^2) = 409.7$ , with  $h = 1.1/45$  the initial length of the side of the mesh quadrilaterals [58]. In the case of the VMS-C and VMS-AC methods, the internal energy initial condition is further projected onto the nodal finite element basis used to approximate the thermodynamic variables [53]. The mesh deformation results are shown in Figure 22. Since the exact solution is obtained by self-similarity arguments and has radial symmetry, the mesh deformation is expected to be smooth. Figure 22(b) shows a clear superiority for the VMS-C method, in terms of mesh displacements (similar deformation patterns, although more distorted, can be observed for the VMS-AC method in Fig. 22(c)). On the other hand, the results for the VMS-P0 method show a pronounced distortion in the element near the origin, possibly due to the onset of an hourglass mode, as already observed in [55, 56].

A comparison of the three approaches with respect to the exact solution is presented in Figure 23. Considering the density plots, the results indicate that the VMS-P0 method is the closest to the exact solution, followed (in terms of accuracy), by the VMS-C and VMS-AC methods. Specifically, the density peak, a good indicator of the overall quality of the computation, is at 5.35 for the VMS-C method, against 5.58 for the VMS-P0 method and only 4.84 for the VMS-AC method. The results of Figure 22 for the mesh displacements are also confirmed by the tangential velocity plots, which show that the VMS-C method has the smallest tangential velocity error.

**Remark20.** As shown in Figure 23, the values of the artificial viscosity are lower for the VMS-C and VMS-AC methods with respect to the VMS-P0 method. This reduced the number of time steps to complete the computation by about 30%.

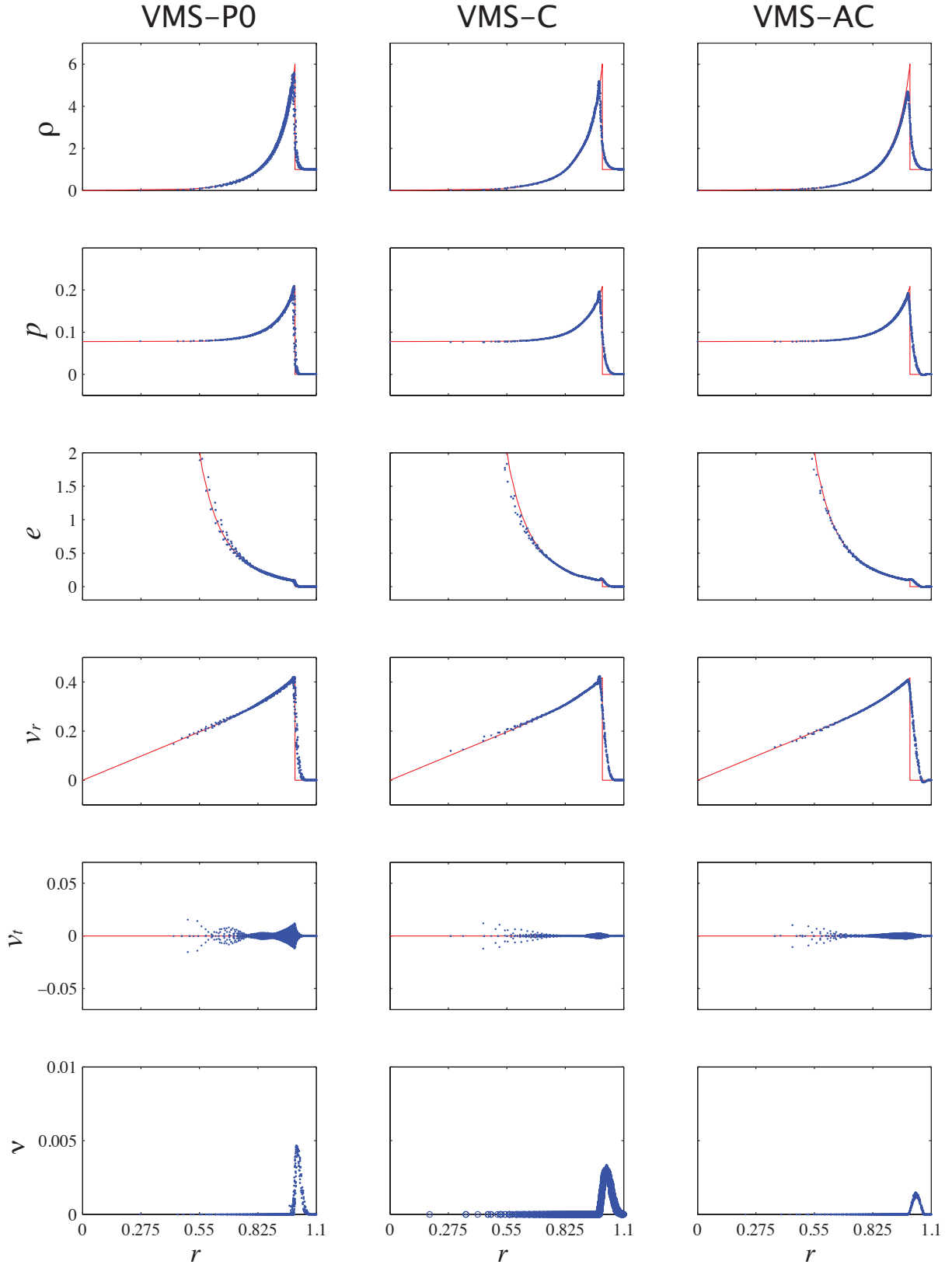
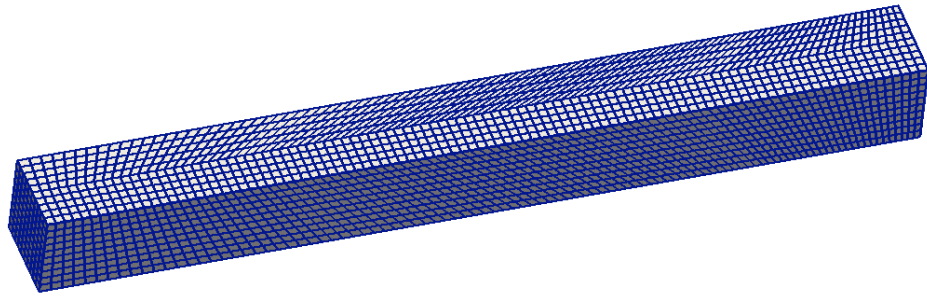
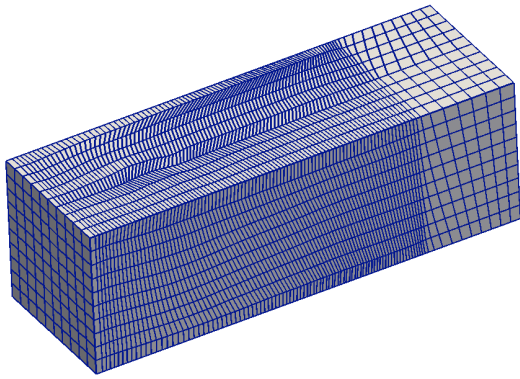


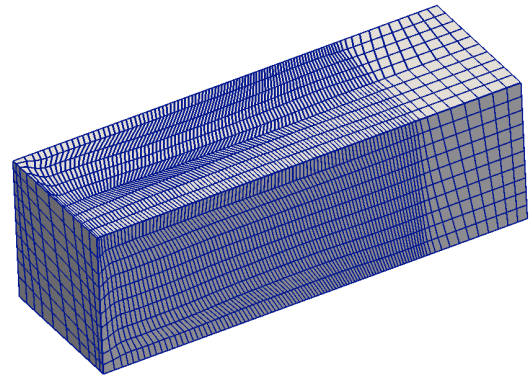
Figure 23: Two-dimensional Sedov test on a Cartesian mesh: Comparison with the exact solution (in red). Left column: VMS-P0 method. Center column: VMS-C method. Right column: VMS-AC method. From the top row down: Density, pressure, internal energy, radial velocity  $v_r$ , tangential velocity  $v_t$ , and artificial viscosities. Each variable is plotted as a function of the radius  $r = \sqrt{x_1^2 + x_2^2}$ . All solution points are rotated around the origin to align on a single radial plane.



(a) Initial mesh configuration.

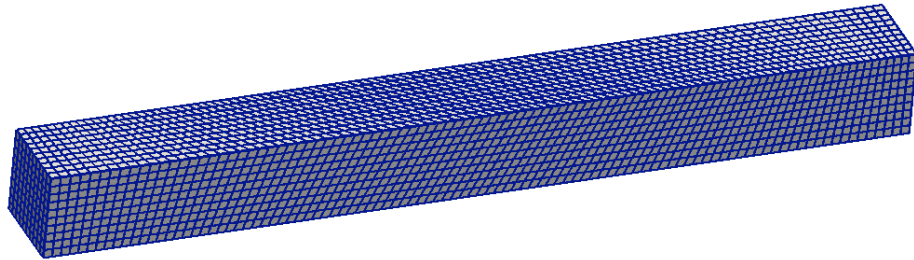


(b) VMS-P0 method at time  $T = 0.7$ .

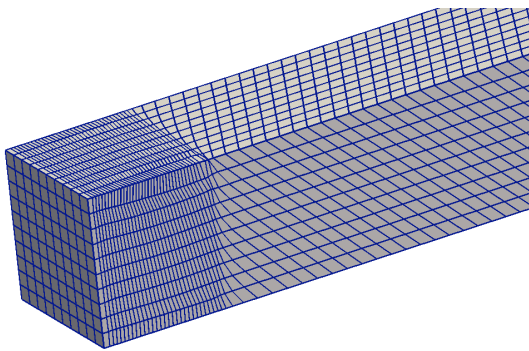


(c) VMS-C method at time  $T = 0.7$ .

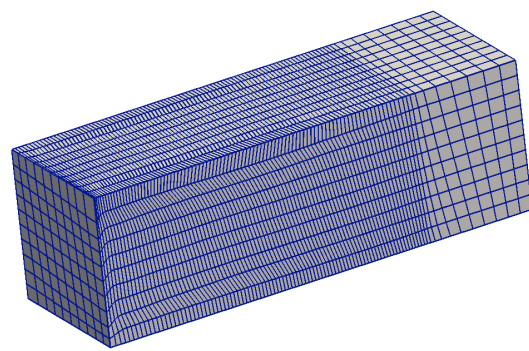
Figure 24: Three-dimensional skewed piston test, as defined in [12].



(a) Initial mesh configuration.



(b) VMS-P0 method.



(c) VMS-C method

Figure 25: Three-dimensional Saltzmann test.

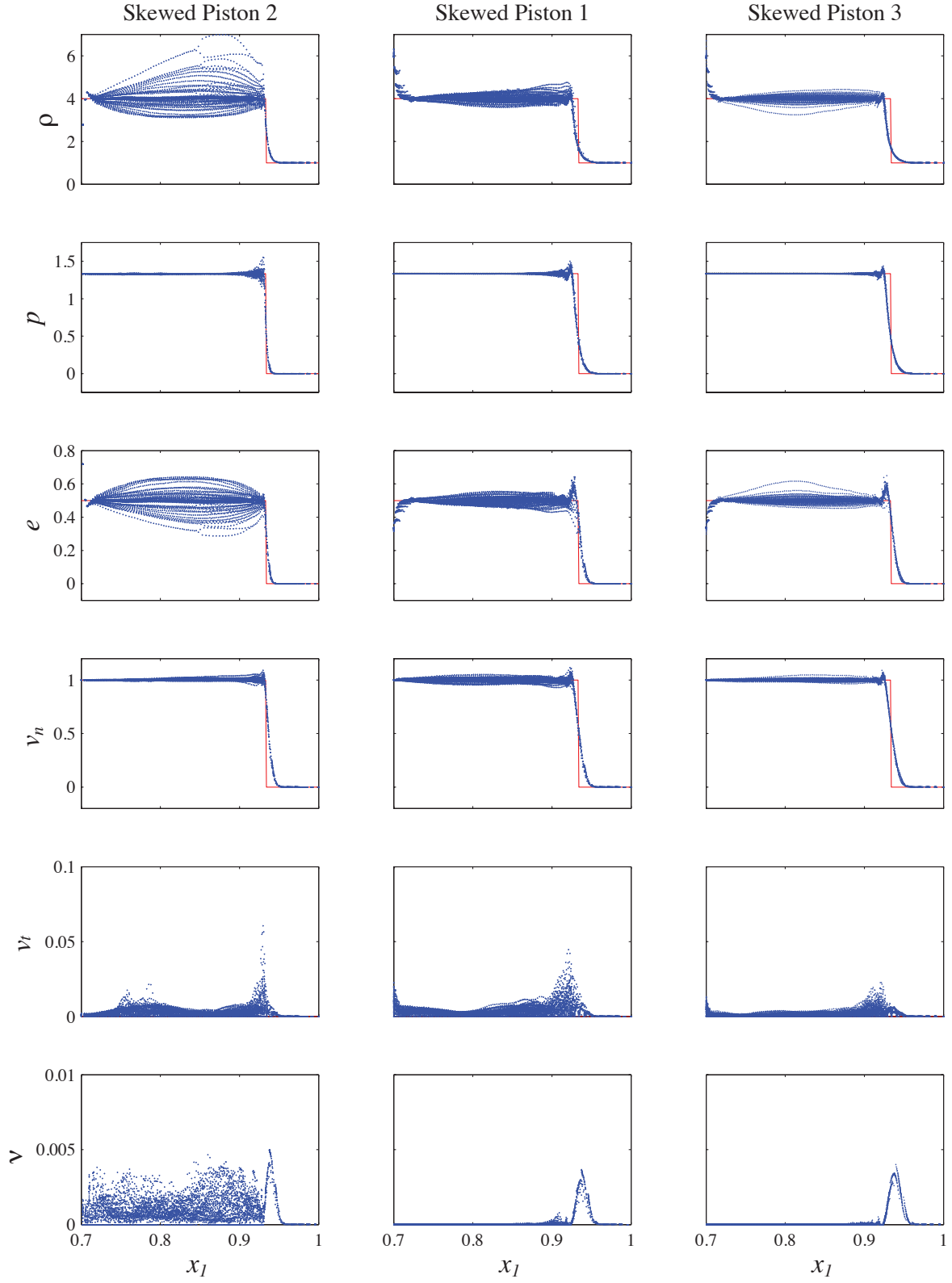


Figure 26: Three-dimensional piston-type problems: Comparison with the exact solution (in red). Left column: VMS-P0 solution for the skewed piston problem. Center column: VMS-C solution for the skewed piston problem. Right column: VMS-C solution for the three-dimensional version of the Saltzman problem. All solution points are projected along the  $x_1$ -coordinate. From the top row down: Density, pressure, internal energy, radial velocity  $v_r$ , tangential velocity  $v_t$ , and artificial viscosities. The velocity component tangential to the motion of the piston is defined as  $v_t = \sqrt{v_2^2 + v_3^2}$ .



**Remark21.** Figure 23 also shows that the VMS-C method is more accurate in capturing the solution with respect to the VMS-AC method. The different choice of artificial viscosity and stabilization are responsible for the improvement in the results.

### 7.6. Three-dimensional skewed piston and Saltzmann tests

We now present two three-dimensional extensions of the two-dimensional Saltzmann test. In the skewed piston test, initially proposed in [12], the nodes of a  $100 \times 10 \times 10$ -element mesh are disposed in a domain  $[0, 1] \times [0, 0.1] \times [0, 0.1]$  according to the following rule:

$$(x_1)_{ijk} = \Delta x_1(i-1) + \alpha_{jk} \sin(\pi \Delta x_1(i-1)), \quad (207)$$

$$(x_2)_{ijk} = \Delta x_2(j-1), \quad (208)$$

$$(x_3)_{ijk} = \Delta x_3(k-1), \quad (209)$$

with

$$\alpha_{jk} = \begin{cases} (0.1 - \Delta x_3(k-1))(1 - 20(\Delta x_2(j-1))), & y \in [0, 0.05], \\ \Delta x_3(k-1)(20(\Delta x_2(j-1)) - 1), & y \in (0.05, 0.1]. \end{cases} \quad (210)$$

This yields the initial mesh in figure 24(a), in which regions of low and high skewness of the mesh are next to each other. The setup of the test in terms of initial and boundary conditions is virtually identical to the two-dimensional Saltzmann test. The mesh deformation at time  $T = 0.7$  for the VMS-P0 and VMS-C methods is depicted in Figure 24(b) and 24(c), respectively. Near the location of the piston, the VMS-C method shows higher element distortion, which however does not seem to affect the overall quality of the solution. In fact, comparing the solutions of the VMS-P0 and VMS-C methods against the exact solution (see the plots in the first two columns of Fig. 26), the overshoots in the solution are much smaller for the VMS-C than for the VMS-P0 method. A comparison with the density plot for the same computations in the very promising work of Nkonga and Maire [42], in Figure 27, shows that the method in [42] is somewhat intermediate in performance between the VMS-P0 and the VMS-C.

An even more challenging test was performed using a mesh with the distribution of points outlined in equations (207)–(209), but this time with

$$\alpha_{jk} = 10(0.05 - \Delta x_3(k-1))(0.1 - \Delta x_2(j-1)). \quad (211)$$

This results in the mesh presented in Figure 25(a), in which a double Saltzmann pattern with reversed direction appears on the lateral faces of the parallelepiped  $[0, 1] \times [0, 0.1] \times [0, 0.1]$ . Initial and boundary conditions are as in the skewed piston test.

In this case, the VMS-P0 algorithm could not perform the computations to the final time, but stopped earlier due to the collapse of the distance between two nodes (see Fig. 25(b)). Instead, the VMS-C algorithm carries the computation through the end (see Fig. 25(c)), and the final solution matches reasonably well the exact solution (right column of Fig. 26).

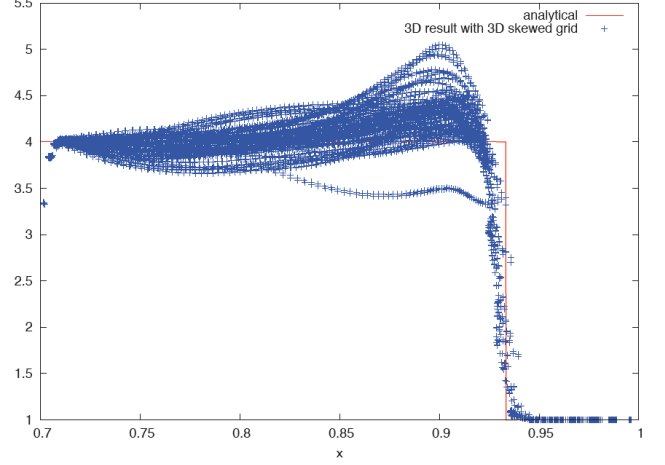


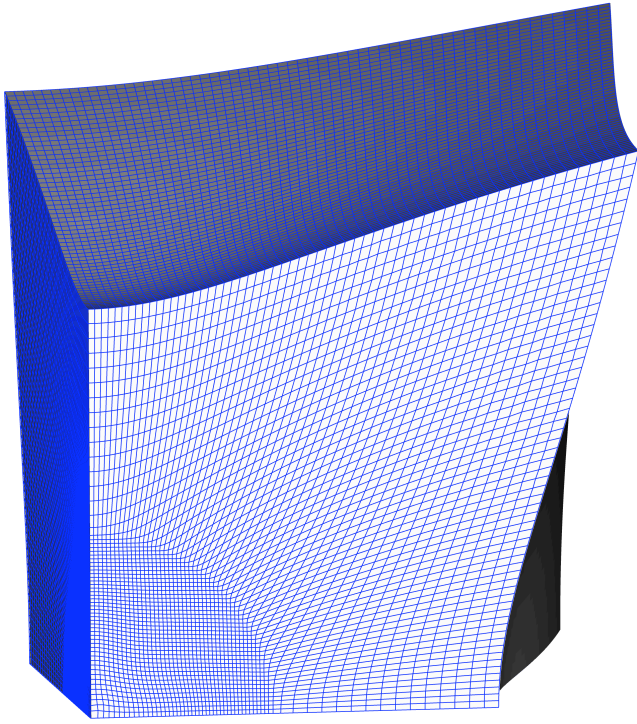
Figure 27: Three-dimensional skewed piston problem: Density plot from the computations performed in [42].

### 7.7. Three-dimensional Noh test on a Cartesian octant

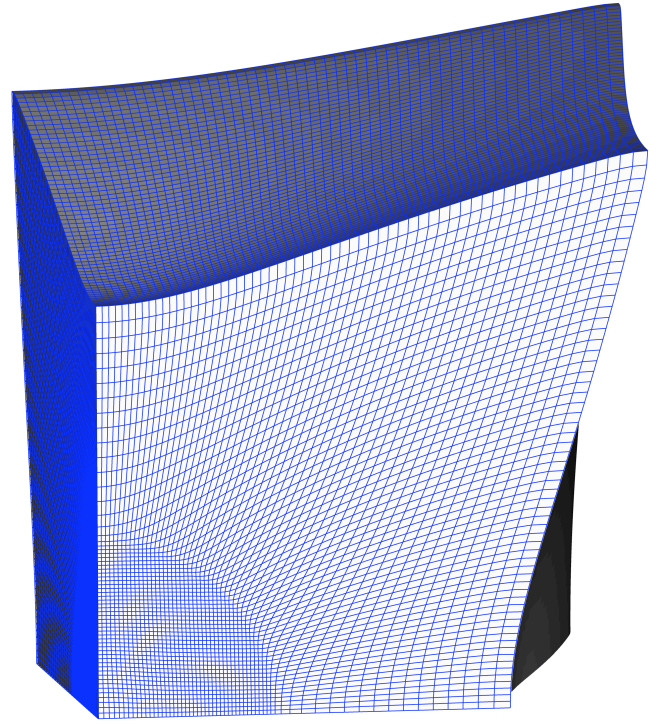
The initial conditions for the Noh test in three dimensions are identical to the two-dimensional case, but will generate a more intense, spherical shock pattern. In this case, since the shock Mach number is infinite for both the two- and three-dimensional case, the density ratio is a better indicator of the shock intensity. In the three-dimensional case, this ratio is 64, against 16 for the two-dimensional case. The domain  $[0, 1.1] \times [0, 1.1] \times [0, 1.1]$  is uniformly meshed with three meshes of resolution  $30^3 = 27,000$ ,  $60^3 = 216,000$ , and  $100^3 = 1,000,000$  cubes. A radial shock propagates with speed  $1/3$  in the computational domain, so that at the final time of 0.6 in the computation, the discontinuity is found at  $r = 0.2$ . The exact solution for the density behind the shock is 64.0 and decays as  $(1 + t/r)^2$  in front of the shock, where  $t$  is time and  $r = \sqrt{x_1^2 + x_2^2 + x_3^2}$  is the radius. Past the shock, the pressure and internal energy take the values  $64/3$  and  $1/2$ , respectively.

Similarly to what was already observed in the two-dimensional setting, also the three-dimensional results show larger distortion in the mesh near the coordinate origin for the VMS-P0 method (Fig. 28(a)), than the VMS-C method (Fig. 28(b)). Again, this is a consequence of larger overheating errors for the VMS-P0 with respect to the VMS-C method, as appreciable in the comparison with the exact solution presented in Figure 29. Because the VMS-AC method was never implemented in three dimensions, we do not present any comparisons with such approach. We would expect, however, a trend very similar to the two-dimensional case.

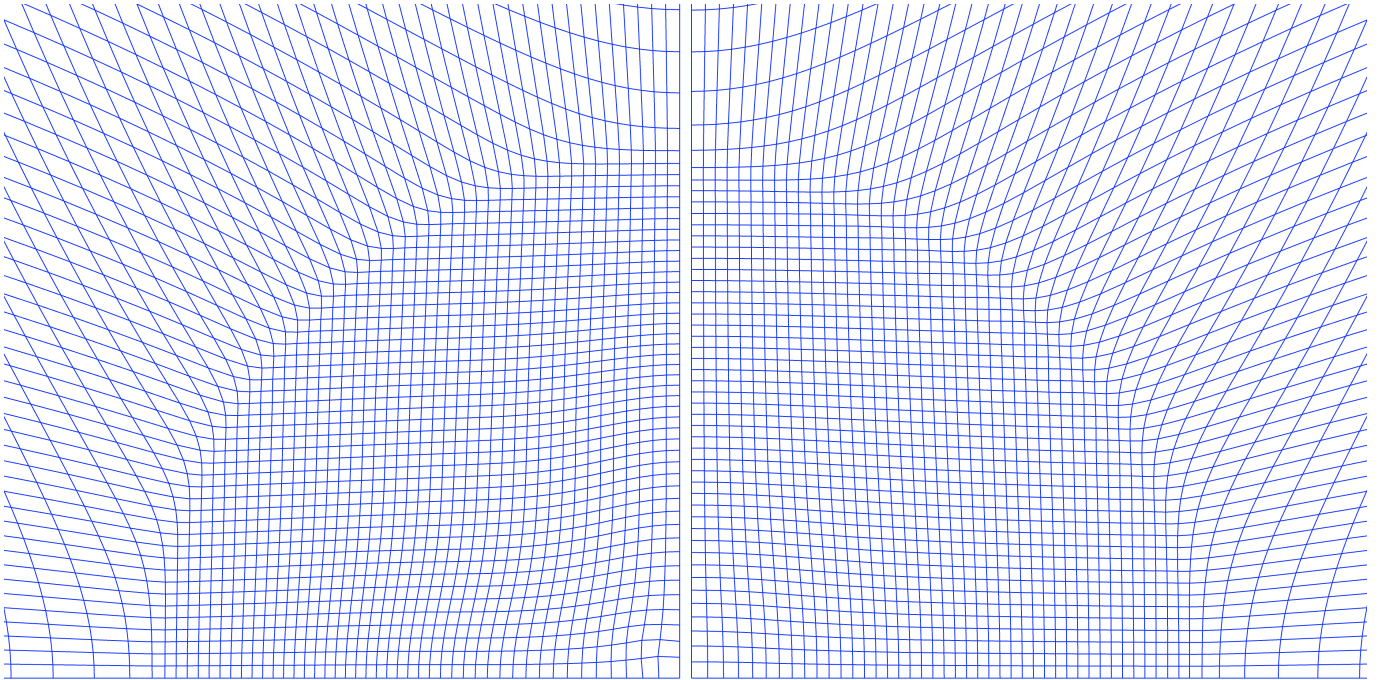
As in the two-dimensional case, the VMS-P0 method shows somewhat sharper shock profiles than the VMS-C method, at the expense of a more pronounced overshoot in the pressure, a larger internal energy overheating, a larger scattering of the data about the exact solution, and, particularly, larger errors in the tangential velocity. Both solutions converge to the exact solution as the mesh is refined, and the overall numerical errors are within the bounds of what is expected for these mesh resolutions [49].



(a) VMS-P0 method.



(b) VMS-C method



(c) Zoomed view. Left: VMS-P0 method. Right: VMS-C method,

Figure 28: Three-dimensional Noh test on a Cartesian mesh: Mesh deformation for the test performed on the  $60^3$  mesh.

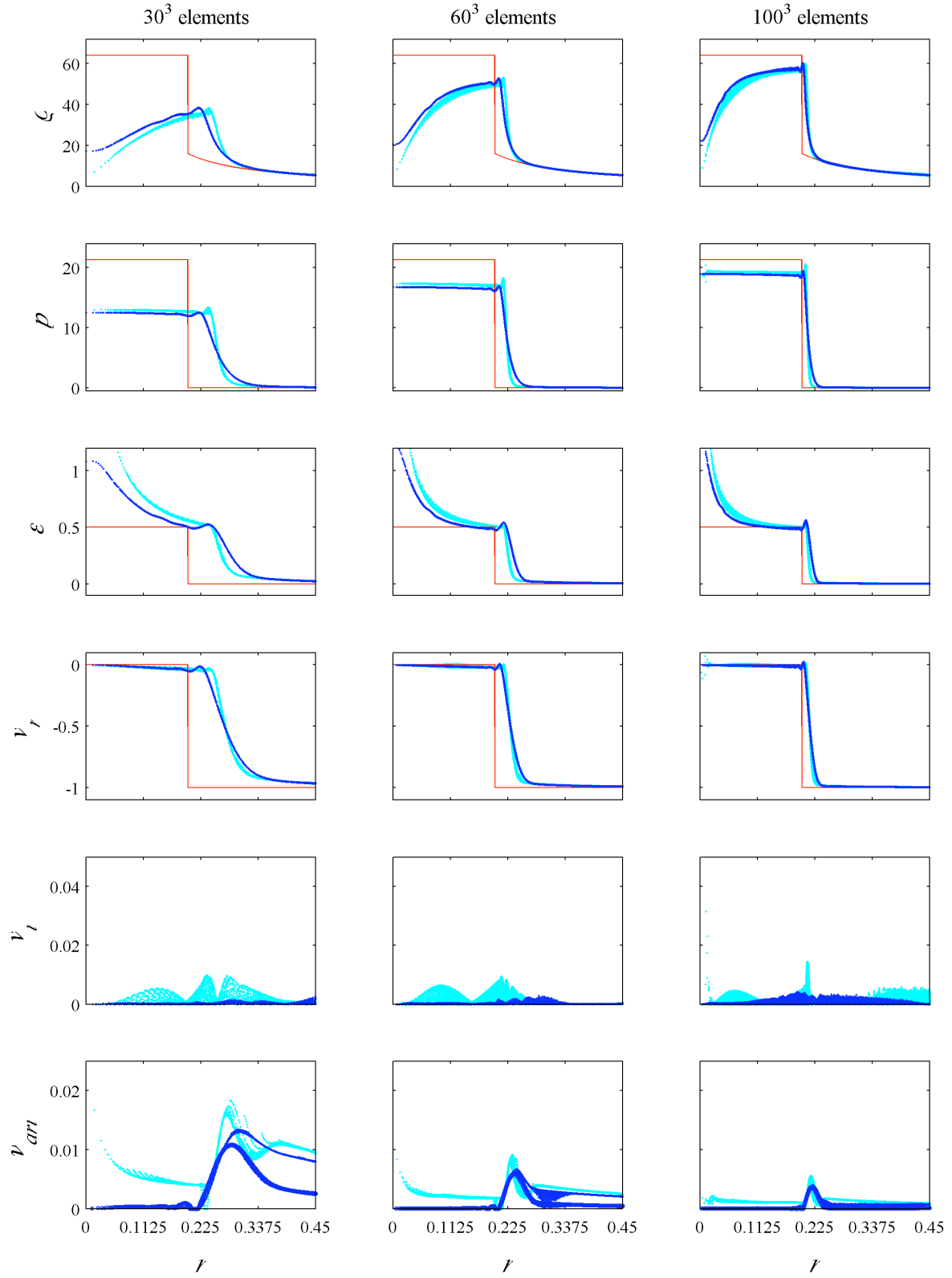
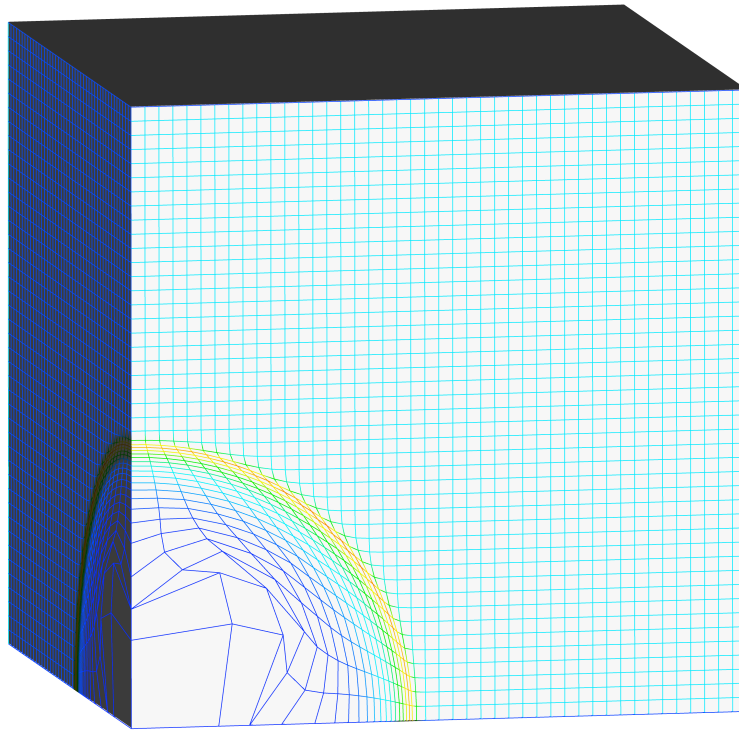
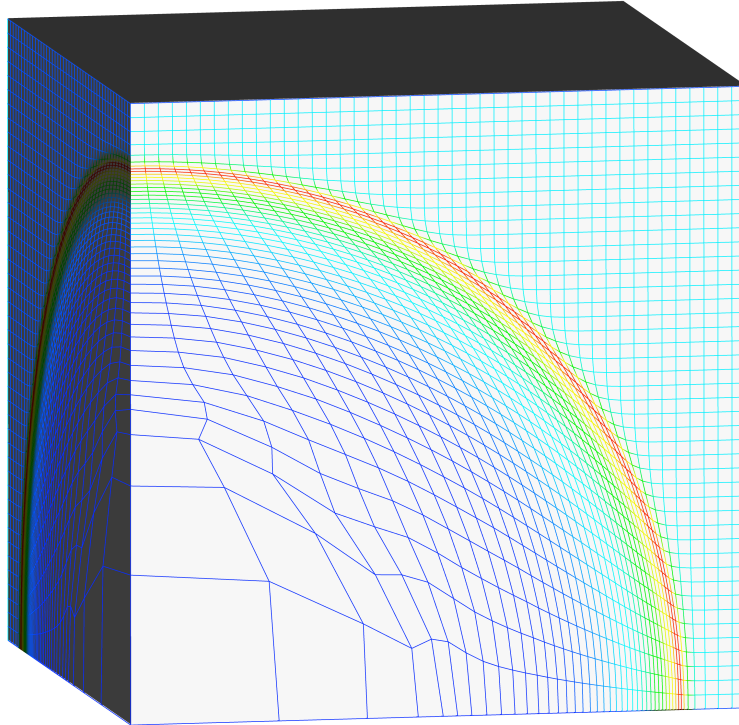


Figure 29: Three-dimensional Noh test on a Cartesian mesh: Comparison with the exact solution (in red) for the  $30^3$  (left),  $60^3$  (center), and  $100^3$  (right) meshes. In light blue (cyan), the VMS-P0 method, in dark blue the VMS-C method. From the top row down: Density, pressure, internal energy, radial velocity  $v_r$ , tangential velocity  $v_t$ , and artificial viscosities. Each variable is plotted as a function of the radius  $r = \sqrt{x_1^2 + x_2^2 + x_3^2}$ .





(a) VMS-P0 method.



(b) VMS-C method.

Figure 30: Three-dimensional Sedov test on a Cartesian mesh of  $44^3$  elements: The VMS-P0 method, could not be run to completion (Fig. 30(a)), due to an hourglass pattern developing near the coordinate origin. The VMS-C method (Fig. 30(b)) did not experience the onset of hourglass modes, and could be run successfully.

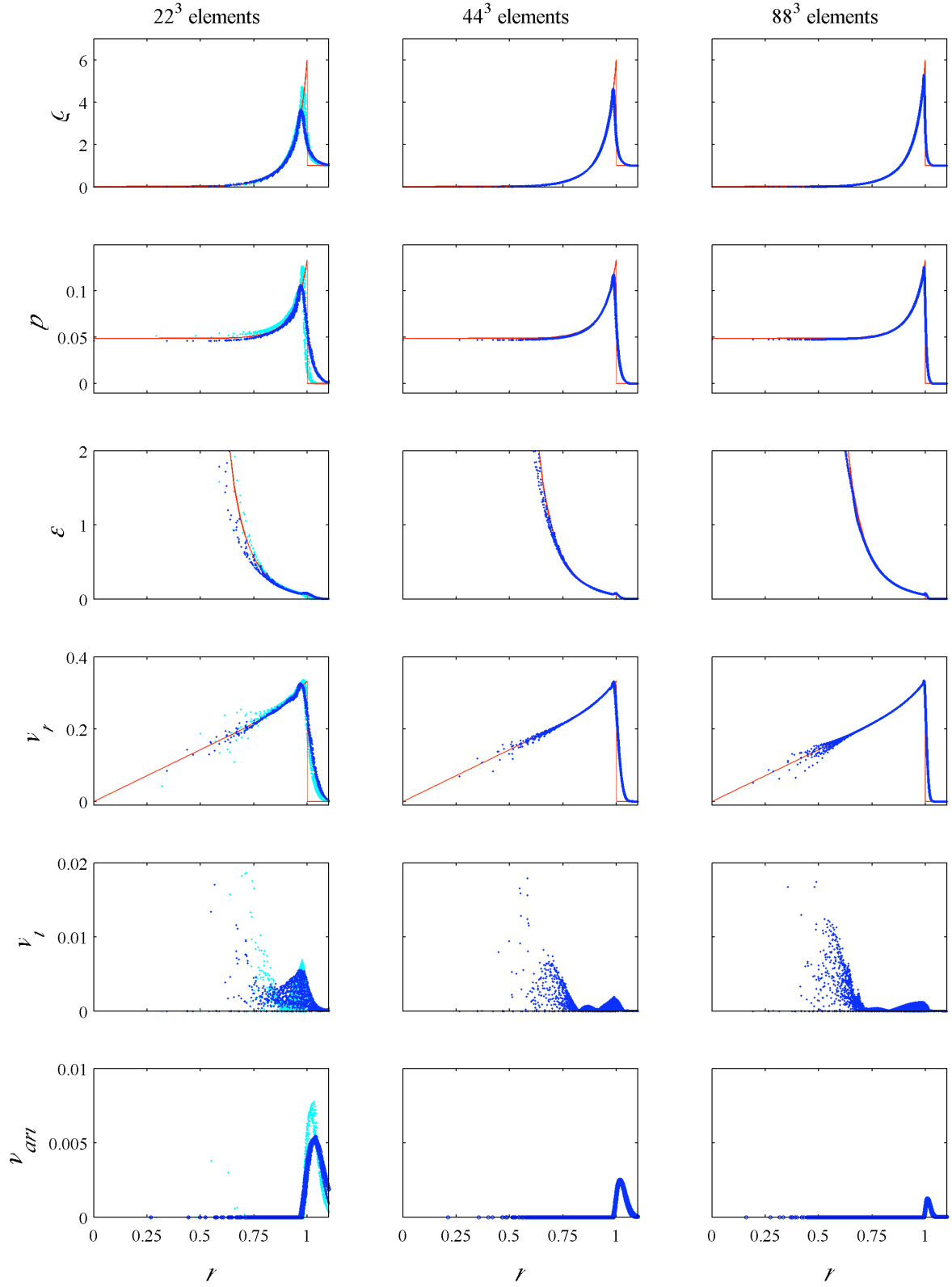


Figure 31: Three-dimensional Sedov test on a Cartesian mesh: Comparison with the exact solution (in red) of computations performed on a  $22^3$  mesh (left column),  $44^3$  mesh (center column), and  $88^3$  mesh (right column). In light blue (only on the left column) the VMS-P0 method, in dark blue the VMS-C method. From the top row down: Density, pressure, internal energy, radial velocity  $v_r$ , tangential velocity  $v_t$ , and artificial viscosities. Each variable is plotted as a function of the radius  $r = \sqrt{x_1^2 + x_2^2 + x_3^2}$ .

### 7.8. Three-dimensional Sedov test on a Cartesian octant

The proposed version of the Sedov blast test is performed on the  $[0, 1.1] \times [0, 1.1] \times [0, 1.1]$  octant, subdivided into  $22^3 = 10,648$ ,  $44^3 = 85,184$ ,  $88^3 = 681,472$  cubic elements. This refinement study is aimed at evaluating the robustness of the method, since, as the mesh-spacing is refined, the initial internal energy distribution is changed so that all the initial internal energy keeps being concentrated in the element adjacent to the coordinate origin. This amounts to setting the initial distribution of internal energy to zero, with the exception of the nearest element to the origin for which  $\epsilon_0 = 0.851/(8h^3)$ , with  $h$  the initial length of the sides of the cubic elements [58]. Note also that because the initial conditions are changed as the mesh is refined, this particular setup of the refinement study cannot be used to evaluate convergence rates. As in the two-dimensional case, the initial conditions for the thermodynamic variables were projected onto the nodal basis.

**Remark22.** The Sedov test in three dimensions is much more challenging than its two-dimensional counterpart, as it can more easily trigger hourglass-type instabilities, for two fundamental reasons: On the one hand, the spherical pattern of the flow is responsible for a higher concentration of internal energy; on the other hand, the space of hourglass modes is much larger in three than in two dimensions. In fact, while there are two hourglass modes out of eight kinematic modes for a two-dimensional quadrilateral, there are actually twelve hourglass modes out of twenty-four kinematic modes for a three dimensional hexahedron [4]. Since a Cartesian mesh is used to represent a spherical flow, it is guaranteed that all the hourglass modes are to some extent excited.

The most remarkable result is that the VMS-P0 method *does not* pass the refinement test. Using the implementation detailed in [55], it was only possible to run successfully the case on the  $22^3$  mesh. Already in the case of the  $44^3$  mesh, due to a spurious hourglass pattern, two nodes of the mesh *collapsed* to infinitesimal distance, driving the time step to zero, as evident in Figure 30(a). This, in spite of the fact that, in contrast with the two-dimensional case, even for the VMS-P0 method the initial condition on the internal energy was smoothed by first performing a nodal projection, and then re-averaging the result on each of the elements of the initial mesh (see [55]).

In this particular test, the VMS-P0 method performance should be taken as indicative of a typical finite element or finite difference method for shock hydrodynamics based on piecewise constant thermodynamic variables and shock capturing artificial viscosities. In fact, we also replaced the variational multiscale hourglass control in the VMS-P0 method with a Flanagan-Belytschko viscous hourglass control [21], and found no substantial improvement on the results. More specifically, the large values of the Flanagan-Belytschko hourglass viscosity needed to run the  $22^3$ -element test case precluded robust computations in the case of the three-dimensional Noh test (see, for more details, [55]). This is by no means a critique of the Flanagan-Belytschko hourglass control [21], originally designed to stabilize solid mechanics computations, and very

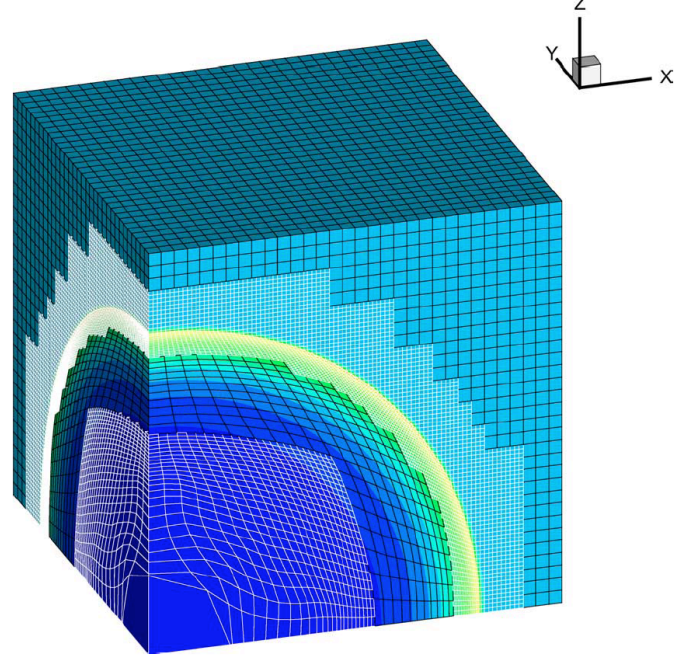


Figure 32: Three-dimensional Sedov test on a Cartesian mesh, mesh deformation and density contour plot from the computations performed in [2].

effective in this context. It is unclear if stabilization methods such as subzonal masses/pressures [13] are a viable choice for this challenging problem, as the presented three-dimensional test on Cartesian geometry has not been reported in the literature.

On the contrary, Figure 30(b) shows how the VMS-C method passes the test. The slight distortion in the mesh is due to a small acoustic pulse produced by the artificial viscosity in the initial stages of the transient, and should not be mistaken for an hourglass pattern: Extensive testing and analysis of the dynamic transient confirms this claim.

Figure 31 shows a comparison of the VMS-P0 and VMS-C methods with the exact solution. We observe that the thermodynamic variables are converging to the exact solution for the VMS-C method, while the error in the transverse velocity does not seem to converge in the  $L^\infty$ -norm (the maximum norm). This is thought to depend on the increased intensity of the spurious acoustic pulse as the mesh is refined (due to the increased localization of initial internal energy near the origin). Observe that, as the mesh is refined, the region of convergence of the radial velocity extends further and further from the shock towards the origin, meaning that there is convergence in a point-wise and  $L^1$ -/  $L^2$ -integral sense.

One important point of note is the fact that the proposed VMS-C method shows very low radial dispersion of the data (particularly, pressure and density). This may be due to the fact that the mesh distortion near the origin is very moderate in computations (compare also with Figs. 32 and 33). In summary, from the presented results, it is clear that the VMS-C method shows exceptional robustness with respect to the VMS-P0 method.

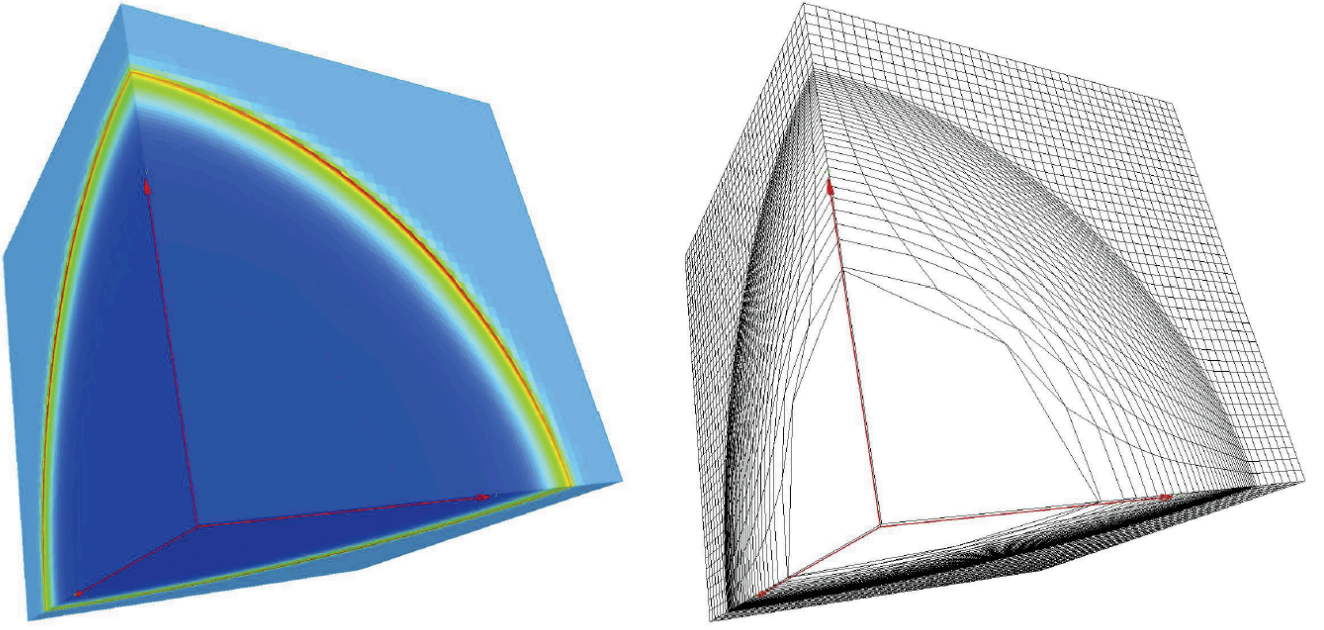


Figure 33: Three-dimensional Sedov test on a Cartesian mesh, mesh deformation and density contour plots from the computations performed in [42].

The only sources in the literature in which the proposed three-dimensional Sedov test was attempted are found in the work of Anderson *et al.* [2], in which adaptive multi-resolution (AMR) techniques in combination with a traditional finite volume/finite difference method are used, and in [42], where successful computations on  $20^3$ - and  $40^3$ -element meshes are performed, using a Godunov-type finite volume method. These results are summarized in Figures 32, 33, and 34, to help the reader in the comparisons.

Although the absence of quantitative results in [2] makes it difficult to precisely compare results, a few observations can be made. In the opinion of the authors, the AMR refinement/definement procedure applied in the computations in [2] may have a beneficial effect in filtering out hourglass modes. These effects are however difficult to reliably control, as the AMR technique is not targeted at removing hourglass *per se*. The density contour/mesh deformation plot of Figure 32 shows still a considerable amount of distortion in the element near the coordinate origin, due to the onset of an hourglass mode (for more details on this interpretation, see [55, 56]).

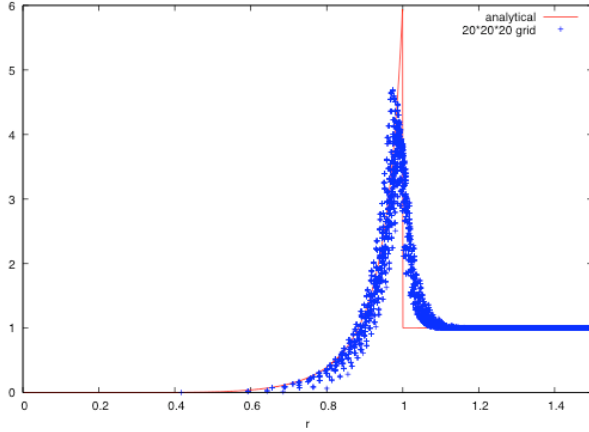
A similar distortion pattern is also seen in the case of the results in Figure 33 using the method in [42], which did not however prevent the computations from running to completion on  $20^3$ - and  $40^3$ -element meshes. Considering the density contours in Figure 33, the effect of the mesh distortion may be responsible for a larger dispersion of the data (especially near the density peak) in Figure 34. Analyzing more carefully the color scheme in Figure 33 (relative to the  $40^3$ -cell grid), it is possible to observe that the darker red color (representing higher density values) is found in the center of the computational domain, away from the edges aligned with the Cartesian axes. This seems to indicate that the density peaks at the interior of

the computational domain, away from edge boundaries. In the case of the VMS-C method in Figure 30(b), instead, this pattern does not appear, and the iso-surfaces at constant density stay very close to spherical. The results in Figure 34 compare otherwise well with the VMS-C method. Considering Figure 34 and the 20-element computation, most of the data points cluster at the peak value of 4, and some reach the higher value of 4.8: these results compare well with the  $22^3$ -element computations performed with the VMS-C method in Figure 31. In particular, the VMS-C method yields a lower peak of the density, probably due to the fact that at this resolution level, the mentioned nodal projection of the initial condition may reduce the peak value of the initial internal energy pulse. For finer meshes, instead, the density peak produced by the VMS-C method at the final instant of the computation becomes considerably sharper. Returning to Figure 34, in the 40-element computation, most of the data points cluster at the peak value 5, and some reach the value 5.5, in good comparison with the results for the VMS-C method on the  $44^3$ -element mesh in Figure 31. No results on meshes of fineness comparable with the  $88^3$ -element case of Figure 31 are presented in [42].

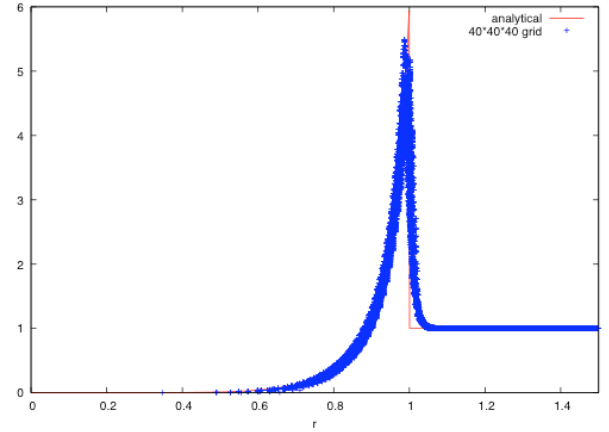
## 8. Summary

This work documents the development of a variational multiscale framework for the stabilization of updated Lagrangian stabilized formulations of shock hydrodynamics. The analysis applies to materials obeying a generalized caloric (e.g., Mie-Grüneisen) equation of state. The proposed algorithm derives from and combines recent work of the authors in the context of stabilization of Lagrangian hydrodynamics systems [52, 53] and strictly conservative time integration techniques [55, 56].





(a)  $20^3$ -mesh.



(b)  $40^3$ -mesh.

Figure 34: Three-dimensional Sedov test on a Cartesian mesh, results from the computations performed in [42]. The density is plotted for a resolution of  $20^3$  elements (left) and  $40^3$  elements. The density is plotted as a function of the radius  $r = \sqrt{x_1^2 + x_2^2 + x_3^2}$ , and all the data is collapsed on a single radial plot.

Although the proposed approach was first developed in the general nonlinear setting, the presentation of the main concepts has been performed first in the simpler linearized system of shock hydrodynamics equations, which corresponds to an acoustic system of equations in Lagrangian coordinates. A predictor/multi-corrector approach, based on a mid-point discretization in time has been presented as a specific implementation of the general concepts, yielding a numerical method which preserves global conservation and Galilean invariance properties in the nonlinear case. It is clear however, that the general methodology can also be extended to a more general class of time integration schemes.

A complete von Neumann analysis of the mentioned predictor/multi-corrector scheme has been performed (in the case of one-dimensional, periodic domains), to study the stability and accuracy properties of the method, and to estimate appropriate values of the stabilization parameters present in the formulation. In this regard, the von Neumann analysis becomes an integral part in its design of the predictor/multi-corrector algorithm. In particular, it was found that the proposed iterative method is formally second-order accurate in space and time. In addition, robust and tight time-stepping bounds have been derived, also in the case when shock capturing operators are active. It appears from this analysis that the effect of variational multiscale operators in shock hydrodynamics computations is to improve the stability and dispersion characteristics of time integrators without adding overly restrictive conditions on the time step. The linearized theory suggests that best results can be achieved with a CFL safety factor of 0.8, and numerical experiments confirm these findings.

Extensive numerical computations on quadrilateral and hexahedral elements in two and three dimensions have been presented and compared with results from previous developments by some the authors and with state-of-the-practice computations by other research groups. In particular, a number of three-dimensional Sedov test computations showed encouraging results in terms of the robustness of the method with respect to

instabilities of hourglass type, which can be considered as virtually absent. Additional work should be devoted to thoroughly testing the present methodology in the case of triangular and tetrahedral meshes in two and three dimensions, and comparing the results to the ones produced in [53].

## Acknowledgments

The authors would like to acknowledge and thank for very valuable discussion Professor T. J. R. Hughes, at the University of Texas in Austin, Dr. M. Shashkov and Dr. L. Margolin at Los Alamos National Laboratory, Dr. A. Robinson, and Dr. P. Bochev at Sandia National Laboratories, Dr. B. D  spres and Dr. B. Rebouret at Commissariat    l'Energie Atomique (CEA, France), Dr. P.-H. Maire at UMR-CELIA-CEA-University of Bordeaux, Dr. M. Ricchiuto at INRIA-Bordeaux, Prof. R. Abgrall at the University of Bordeaux, and Dr. Santiago Badia, at Universitat Polit  cnica de Catalunya (Barcelona). The authors would also like to thank Dr. R. Summers and Dr. S. Collis at Sandia National Laboratories, for support and encouragement during the development of this research work.

## A. Von Neumann analysis

This appendix presents the von Neumann analysis of the predictor/multi-corrector method developed in Section 4, for the interested reader. As a first step, consider the stabilized equations (67)–(68), discretized using the predictor/multi-corrector algorithm described in Section 4.2, in the one-dimensional, periodic case. More precisely, equations (67)–(68) are augmented by diffusive operators deriving from the linearization of the discontinuity capturing operators defined by (148)–(149). Namely, denoting by  $\mathbb{T}$  the unit periodic torus along the real line  $\mathbb{R}$ , and considering a piece-wise linear finite element decomposition, we have that, for every discrete

test functions  $\psi$  and  $\phi$ ,

$$0 = \int_{\mathbb{T}} \psi \dot{V} dX - \int_{\mathbb{T}} \psi_{,X} P dX + \int_{\mathbb{T}} \psi_{,X} \tau (\dot{P} + c_s^2 V_{,X}) dX + \int_{\mathbb{T}} \psi_{,X} \nu_V V_{,X} dX, \quad (212)$$

$$0 = \int_{\mathbb{T}} \phi \dot{P} dX + \int_{\mathbb{T}} \phi c_s^2 V_{,X} dX + \int_{\mathbb{T}} \phi_{,X} \tau c_s^2 (\dot{V} + P_{,X}) dX + \int_{\mathbb{T}} \phi_{,X} \nu_P P_{,X} dX, \quad (213)$$

where we have dropped the "h" superscript and we have used the notation  $V = \rho v$  (recall  $\rho = \text{const.}$ ) and  $P = p$ . For the sake of simplicity, we assume  $\nu_V = \nu_P = \nu$ . Hence, the discretization in time of (212)-(213) yields:

$$0 = \int_{\mathbb{T}} \psi (V_{n+1}^{(i+1)} - V_n) dX - \Delta t \int_{\mathbb{T}} \psi_{,X} P_{n+1/2}^{(i)} dX + \Delta t \int_{\mathbb{T}} \psi_{,X} \tilde{\tau} (P_{n+1}^{(i)} - P_n + \Delta t c_s^2 (V_{,X})_{n+1/2}^{(i)}) dX + \Delta t \int_{\mathbb{T}} \psi_{,X} \nu (V_{,X})_{n+1/2}^{(i)} dX, \quad (214)$$

$$0 = \int_{\mathbb{T}} \phi (P_{n+1}^{(i+1)} - P_n) dX + \Delta t \int_{\mathbb{T}} \phi c_s^2 (V_{,X})_{n+1/2}^{(i+1)} dX + \Delta t \int_{\mathbb{T}} \phi_{,X} \tilde{\tau} c_s^2 (V_{n+1}^{(i+1)} - V_n + \Delta t (P_{,X})_{n+1/2}^{(i)}) dX + \Delta t \int_{\mathbb{T}} \phi_{,X} \nu (P_{,X})_{n+1/2}^{(i)} dX, \quad (215)$$

where  $\tilde{\tau} = \frac{\tau}{\Delta t} = \frac{c_s}{2}$ ,  $(\cdot)^{(i)}$  and  $(\cdot)^{(i+1)}$  are used to denote quantities computed with the predictor/corrector iterates  $(i)$  and  $(i+1)$ , respectively.

We assume a uniform, equispaced subdivision of the torus  $\mathbb{T}$  into finite elements of measure  $h$ . Recalling that both pressure and velocity are approximated by piece-wise linear functions, and using mass lumping, the following finite difference equations are derived:

$$0 = V_{j,n+1}^{(i+1)} - V_{j,n} + \frac{\sigma}{4c_s} (P_{j+1,n+1}^{(i)} + P_{j+1,n} - P_{j-1,n+1}^{(i)} - P_{j-1,n}) - \frac{\sigma}{2c_s} \tilde{\tau} (P_{j+1,n+1}^{(i)} - P_{j+1,n} - P_{j-1,n+1}^{(i)} + P_{j-1,n}) - \frac{\kappa + \tilde{\tau}\sigma^2}{2} (V_{j+1,n+1}^{(i)} + V_{j+1,n} - 2V_{j,n+1}^{(i)} - 2V_{j,n} + V_{j-1,n+1}^{(i)} + V_{j-1,n}), \quad (216)$$

$$0 = P_{j,n+1}^{(i+1)} - P_{j,n} + \frac{c_s\sigma}{4} (V_{j+1,n+1}^{(i+1)} + V_{j+1,n} - V_{j-1,n+1}^{(i+1)} - V_{j-1,n}) - \frac{c_s\sigma}{2} \tilde{\tau} (V_{j+1,n+1}^{(i+1)} - V_{j+1,n} - V_{j-1,n+1}^{(i+1)} + V_{j-1,n}) - \frac{\kappa + \tilde{\tau}\sigma^2}{2} (P_{j+1,n+1}^{(i)} + P_{j+1,n} - 2P_{j,n+1}^{(i)} - 2P_{j,n} + P_{j-1,n+1}^{(i)} + P_{j-1,n}), \quad (217)$$

where  $j$  is the node index,  $\sigma = \frac{c_s \Delta t}{h}$  is the acoustic Courant number and  $\kappa = \frac{\nu \Delta t}{h^2}$ .

**Remark23.** In order to keep the analysis as close as possible to the predictor/multi-corrector algorithm of Section 4, the latest available velocity iterate  $V_{n+1}^{(i+1)}$  is used in (215) and (217).

In conformity with the von Neumann stability analysis (see [48, 60] for details), because the boundary conditions are periodic, we can expand the solution degrees-of-freedom as a finite, linear combination of complex exponentials with complex coefficients. This eventually amounts to applying a Discrete Fourier Transform (DFT) operator to the discrete equations (216)–(217). In particular, we have:

$$V_{j,n}^{(i)} = \sum_{k=-N/2+1}^{N/2} \hat{V}_{k,n}^{(i)} e^{i\beta_k j}, \quad (218)$$

$$P_{j,n}^{(i)} = \sum_{k=-N/2+1}^{N/2} \hat{P}_{k,n}^{(i)} e^{i\beta_k j}, \quad (219)$$

where  $i = \sqrt{-1}$ , and  $\hat{V}_{k,n}^{(i)}$  and  $\hat{P}_{k,n}^{(i)}$  are the Fourier coefficients for velocity and pressure, relative to the  $k$ th harmonic, the  $n$ th time step and the  $i$ th iterate. Note that  $N$  is the number of elements (a multiple of 2), and  $\beta_k = \frac{2\pi h k}{|\mathbb{T}|} = \frac{2\pi k}{N}$  is an angularly scaled version of the integer wave number  $k$  (with  $|\mathbb{T}| = \text{meas}(\mathbb{T}) = Nh = 1$  the measure of the torus). Complex exponentials associated to different wave numbers satisfy a discrete orthogonality property:

$$\sum_{m=-N/2}^{N/2-1} e^{i\beta_k m} e^{i\beta_q m} = \delta_{kq}, \quad \text{for } -N/2 \leq k, q \leq N/2, \quad (220)$$

with  $\delta_{kq}$  the Kronecker delta tensor ( $\delta_{kq} = 1$  if  $k = q$ , and  $\delta_{kq} = 0$  if  $k \neq q$ ). We then replace (218)–(219) into (216)–(217) multiplied by  $e^{i\beta_k j}$  and  $e^{i\beta_r j}$ , respectively, and we sum over  $j$ . Due to the orthogonality property (220), and the linearity of the system of equations (216)–(217), it is easy to verify that the previous steps lead to  $N$  pairs of equations, coupling the dynamics of the  $k$ th pressure and velocity modes, with  $-N/2 + 1 \leq k \leq N/2$ . Namely:

$$(\mathbf{I} + \mathbf{A}_0) \hat{\mathbf{Z}}_{k,n+1}^{(i+1)} = \mathbf{A}_1 \hat{\mathbf{Z}}_{k,n+1}^{(i)} + (\mathbf{I} + \mathbf{A}_2) \hat{\mathbf{Z}}_{k,n}, \quad (221)$$

where

$$\hat{\mathbf{Z}}_{k,n}^{(i)} = \begin{Bmatrix} \hat{V}_{k,n}^{(i)} \\ \hat{P}_{k,n}^{(i)} \end{Bmatrix} \quad (222)$$

is the  $k$ th velocity/pressure modal pair, relative to the  $n$ th time

step and the  $i$ th iterate, and

$$\mathbf{I} = \begin{bmatrix} 1 & 0 \\ 0 & 1 \end{bmatrix}, \quad (223)$$

$$\mathbf{A}_0 = \begin{bmatrix} 0 & 0 \\ -i\left(\tilde{\tau} - \frac{1}{2}\right)c_s \sigma \sin(\beta_k) & 0 \end{bmatrix}, \quad (224)$$

$$\mathbf{A}_1 = \begin{bmatrix} (\tilde{\tau}\sigma^2 + \kappa)(\cos(\beta_k) - 1) & i\left(\tilde{\tau} - \frac{1}{2}\right)\frac{\sigma}{c_s} \sin(\beta_k) \\ 0 & (\tilde{\tau}\sigma^2 + \kappa)(\cos(\beta_k) - 1) \end{bmatrix}, \quad (225)$$

$$\mathbf{A}_2 = \begin{bmatrix} (\tilde{\tau}\sigma^2 + \kappa)(\cos(\beta_k) - 1) & -i\left(\tilde{\tau} + \frac{1}{2}\right)\frac{\sigma}{c_s} \sin(\beta_k) \\ -i\left(\tilde{\tau} + \frac{1}{2}\right)c_s \sigma \sin(\beta_k) & (\tilde{\tau}\sigma^2 + \kappa)(\cos(\beta_k) - 1) \end{bmatrix}. \quad (226)$$

It is also very important to observe that because the degrees-of-freedom “signal” has real values, the discrete Fourier coefficients must satisfy the complex conjugacy property

$$\hat{\mathbf{Z}}_{-k,n}^{(i)} = \left(\hat{\mathbf{Z}}_{k,n}^{(i)}\right)^*, \quad \text{for } 0 \leq k \leq N/2 - 1, \quad (227)$$

where  $\hat{\mathbf{W}}^*$  indicates the complex conjugate of  $\hat{\mathbf{W}}$  (componentwise), and, in addition, the following condition for the often called “odd ball” mode holds:

$$\hat{\mathbf{Z}}_{N/2,p}^{(i)} = \mathbf{0}. \quad (228)$$

Because complex conjugates have the same absolute value and opposite phase, it is sufficient to limit the study of the amplification factors to the discrete modes in the range  $0 \leq k < N/2$ , that is,  $0 \leq \beta_k < \pi$ .

The vector equation (221) is a recurrence relationship between the predictor/multi-corrector iterates of the proposed time-integration approach. Set

$$\mathbf{B}_0 = (\mathbf{I} + \mathbf{A}_0)^{-1}(\mathbf{I} + \mathbf{A}_2), \quad (229)$$

$$\mathbf{B}_1 = (\mathbf{I} + \mathbf{A}_0)^{-1}\mathbf{A}_1. \quad (230)$$

Recalling that the first guess for the new iterate at time  $t_{n+1}$  is the solution at time  $t_n$ , namely  $\hat{\mathbf{Z}}_{k,n+1}^{(0)} = \hat{\mathbf{Z}}_{k,n}$ , we can derive explicit recurrence formulas for the computation of  $\hat{\mathbf{Z}}_{k,n+1}^{(i+1)}$  in terms of  $\hat{\mathbf{Z}}_{k,n}$ :

$$\begin{aligned} \hat{\mathbf{Z}}_{k,n+1}^{(1)} &= \mathbf{B}_1 \hat{\mathbf{Z}}_{k,n+1}^{(0)} + \mathbf{B}_0 \hat{\mathbf{Z}}_{k,n} \\ &= (\mathbf{B}_0 + \mathbf{B}_1) \hat{\mathbf{Z}}_{k,n} \\ &= \mathbf{G}^{(1)} \hat{\mathbf{Z}}_{k,n}, \end{aligned} \quad (231)$$

$$\begin{aligned} \hat{\mathbf{Z}}_{k,n+1}^{(i+1)} &= \mathbf{B}_1 \hat{\mathbf{Z}}_{k,n+1}^{(i)} + \mathbf{B}_0 \hat{\mathbf{Z}}_{k,n} \\ &= (\mathbf{B}_1 \mathbf{G}^{(i)} + \mathbf{B}_0) \hat{\mathbf{Z}}_{k,n} \\ &= \mathbf{G}^{(i+1)} \hat{\mathbf{Z}}_{k,n}. \end{aligned} \quad (232)$$

In the limit for an infinite number of iterations, we obtain the amplification matrix for the original implicit mid-point algorithm from which the predictor/corrector time integrator is derived:

$$(\mathbf{I} + \mathbf{A}_0) \hat{\mathbf{Z}}_{k,n+1}^{(\infty)} = \mathbf{A}_1 \hat{\mathbf{Z}}_{k,n+1}^{(\infty)} + (\mathbf{I} + \mathbf{A}_2) \hat{\mathbf{Z}}_{k,n}, \quad (233)$$

that is, removing the superscript  $(\infty)$  from  $\hat{\mathbf{Z}}_{k,n+1}^{(\infty)}$ , and rearranging terms,

$$\hat{\mathbf{Z}}_{k,n+1} = (\mathbf{I} + \mathbf{A}_0 - \mathbf{A}_1)^{-1}(\mathbf{I} + \mathbf{A}_2) \hat{\mathbf{Z}}_{k,n} = \mathbf{G}^{(\infty)} \hat{\mathbf{Z}}_{k,n}. \quad (234)$$

**Remark24.** The predictor/multi-corrector method has the nature of a Gauss-Seidel iterative, fixed-point scheme, since the matrix  $\mathbf{I} + \mathbf{A}_0$  is lower diagonal.

**Remark25.** Convergence of the fixed-point iteration is ensured if  $\|\mathbf{B}_1\| < 1$  (sufficient condition). It will be subsequently shown that this condition is equivalent to the temporal stability condition.

## B. Stability of the highest wavembers

Stability of the highest modes in a computation is only a necessary condition for overall stability, but is of practical use in computations since it can provide simple time-step control estimates.

The amplification of the highest wave number is governed by the matrices  $\mathbf{G}^{(i)}$ , when  $\beta_k$  is set equal to  $\pi$ . In this case, it is easy to observe that  $\mathbf{A}_0 = \mathbf{0}$ , and that  $\mathbf{A}_1$  and  $\mathbf{A}_2$  become diagonal and equal to a multiple of the identity matrix  $\mathbf{I}$ . In particular,

$$\mathbf{A}_1 = \mathbf{A}_2 = -(c_\tau \sigma^2 + 2\kappa)\mathbf{I}. \quad (235)$$

Therefore, the time evolution of the highest pressure and velocity Fourier modes is decoupled and identical. The study of the proposed predictor/multi-corrector method can therefore be reduced to a scalar problem. Setting  $\alpha = c_\tau \sigma^2 + 2\kappa \geq 0$ , we obtain:

$$\mathbf{G}^{(1)} = (1 - 2\alpha)\mathbf{I}, \quad (236)$$

$$\mathbf{G}^{(2)} = (1 - 2\alpha + 2\alpha^2)\mathbf{I}, \quad (237)$$

$$\mathbf{G}^{(3)} = (1 - 2\alpha + 2\alpha^2 - 2\alpha^3)\mathbf{I}, \quad (238)$$

$$\mathbf{G}^{(4)} = \dots. \quad (239)$$

Using the classical formulas for polynomial division, the results for the first few iterates suggest the following general formula:

$$\mathbf{G}^{(i)} = \left(2 \frac{1 - (-\alpha)^{i+1}}{1 + \alpha} - 1\right) \mathbf{I}. \quad (240)$$

Proving (240) is easily achieved by recurrence. In fact (240) applies for  $i = 1$ , and assuming (240) holds for a given  $i$ , we

have that, using (229), (230), and (232),

$$\begin{aligned}
\mathbf{G}^{(i+1)} &= \mathbf{B}_1 \mathbf{G}^{(i)} + \mathbf{B}_0 \\
&= -\alpha \mathbf{G}^{(i)} + (1 - \alpha) \mathbf{I} \\
&= \left( -\alpha \left( 2 \frac{1 - (-\alpha)^{i+1}}{1 + \alpha} - 1 \right) + 1 - \alpha \right) \mathbf{I} \\
&= \left( \frac{1 - \alpha + 2\alpha(-\alpha)^{i+1}}{1 + \alpha} \right) \mathbf{I} \\
&= \left( \frac{-1 - \alpha + 2(1 - (-\alpha)^{i+2})}{1 + \alpha} \right) \mathbf{I} \\
&= \left( 2 \frac{1 - (-\alpha)^{i+2}}{1 + \alpha} - 1 \right) \mathbf{I}. \tag{241}
\end{aligned}$$

For stability, the following inequalities must be satisfied:

$$-1 \leq \left( 2 \frac{1 - (-\alpha)^{i+1}}{1 + \alpha} - 1 \right) \leq 1. \tag{242}$$

Observing that  $\alpha \geq 0$ , the left inequality in (242) yields  $(-\alpha)^{i+1} \leq 1$ , which holds true either if  $i$  is even or if  $i$  is odd and  $\alpha \leq 1$ . Analogously, the right inequality yields  $(-\alpha)^i \leq 1$ , which holds true either if  $i$  is odd or if  $i$  is even and  $\alpha \leq 1$ . In conclusion, the condition

$$\alpha \leq 1 \tag{243}$$

is sufficient for stability of the highest wave numbers. Condition (243) can then be used to estimate the stable time-step size, as it implies

$$c_\tau \sigma^2 + 2\kappa - 1 \leq 0, \quad \text{or,} \quad c_\tau c_s^2 \Delta t^2 + 2\nu \Delta t - h^2 \leq 0. \tag{244}$$

Solving the associated quadratic equation yields the bounds

$$\frac{-\nu - \sqrt{\nu^2 + c_\tau c_s^2 h^2}}{c_\tau c_s^2} \leq \Delta t \leq \frac{-\nu + \sqrt{\nu^2 + c_\tau c_s^2 h^2}}{c_\tau c_s^2}. \tag{245}$$

The left bound is always verified, the right gives the stability limit. Multiplying and dividing the right inequality by  $\nu + \sqrt{\nu^2 + c_\tau c_s^2 h^2}$  (always a strictly positive quantity in computations) and simplifying the term  $c_\tau c_s^2$ , we obtain

$$\Delta t \leq \frac{h^2}{\nu + \sqrt{\nu^2 + c_\tau c_s^2 h^2}}. \tag{246}$$

**Remark26.** As already mentioned, the predictor multi-corrector approach can also be interpreted as a fixed-point iteration procedure [56]. A sufficient condition for the convergence (in spectral space) of such procedure is  $\|\mathbf{B}_1\| < 1$ , that is  $\rho(\mathbf{B}_1) < 1$  (where, as usual,  $\rho(\mathbf{B}_1)$  denotes the spectral radius of the matrix  $\rho(\mathbf{B}_1)$ ). It is not difficult to verify that, in the case of the highest wave number, that is  $\beta_k = \pi$ , this condition coincides with (244). By plotting contour surfaces at  $\rho(\mathbf{B}_1) = 1$ , we were also able to graphically verify that the stability implies convergence of the corrector iterates on the entire space  $[\sigma, \kappa, \beta_k]$ . This approach is virtually identical to the one outlined in Section 6.5 (particularly, Figure 11) and will not be reported here, for the sake of brevity.

## References

- [1] M. L. Abell and J. P. Braselton. *Mathematica by Example*. Academic Press, 4th edition, 2008.
- [2] R. W. Anderson, N. S. Elliott, and R. B. Pember. An arbitrary Lagrangian-Eulerian method with adaptive mesh refinement for the solution of the Euler equations. *Journal of Computational Physics*, **199**(2):598–617, 2004.
- [3] A. Barlow. A compatible finite element multi-material ALE hydrodynamics algorithm. *International Journal for Numerical Methods in Fluids*, **56**(8):953–964, 2008.
- [4] T. Belytschko, W. K. Liu, and B. Moran. *Nonlinear Finite Elements for Continua and Structures*. J. Wiley & Sons, New York, 2000.
- [5] D. J. Benson. A new two-dimensional flux-limited shock viscosity for impact calculations. *Computer Methods in Applied Mechanics and Engineering*, **93**:39–95, 1991.
- [6] D. J. Benson. Computational methods in Lagrangian and Eulerian hydrocodes. *Computer Methods in Applied Mechanics and Engineering*, **99**:235–394, 1992.
- [7] H. Brezis. *Analyse Fonctionnelle: Théorie et Applications*. Dunod, Paris, 1983.
- [8] F. Brezzi, L. P. Franca, T. J. R. Hughes, and A. Russo.  $b = \int g$ . *Computer Methods in Applied Mechanics and Engineering*, **145**(3-4):329–339, 1997.
- [9] J. C. Campbell and M. J. Shashkov. A compatible Lagrangian algorithm for unstructured grids. Technical report, LA-UR-00-3231, Los Alamos National Laboratory, 2000.
- [10] J. C. Campbell and M. J. Shashkov. A tensor artificial viscosity using a mimetic finite difference algorithm. Technical report, LA-UR-00-2290, Los Alamos National Laboratory, 2000.
- [11] J. C. Campbell and M. J. Shashkov. A tensor artificial viscosity using a mimetic finite difference algorithm. *Journal of Computational Physics*, **172**:739–765, 2001.
- [12] E. J. Caramana, C. L. Rousculp, and D. E. Burton. A compatible, energy and symmetry preserving Lagrangian hydrodynamics algorithm in three-dimensional Cartesian geometry. *Journal of Computational Physics*, **157**, 2000.
- [13] E. J. Caramana and M. J. Shashkov. Elimination of artificial grid distortion and hourglass-type motions by means of Lagrangian subzonal masses and pressures. *Journal of Computational Physics*, **142**(2):521–561, 1998.
- [14] E. J. Caramana, M. J. Shashkov, and P. P. Whalen. Formulations of artificial viscosity for multi-dimensional shock wave computations. *Journal of Computational Physics*, **144**:70–97, 1998.
- [15] R. Codina. Finite element approximation of the hyperbolic wave equation in mixed form. *Computer Methods in Applied Mechanics and Engineering*, **197**(13-16):1305–1322, 2008.
- [16] R. Codina, J. Principe, O. Guasch, and S. Badia. Time dependent sub-scales in the stabilized finite element approximation of incompressible flow problems. *Computer Methods in Applied Mechanics and Engineering*, **196**(21-24):2413–2430, 2007.
- [17] A. W. Cook and W. H. Cabot. A high-wavenumber viscosity for high-resolution numerical methods. Technical Report UCRL-ID-152002, Lawrence Livermore National Laboratory, Livermore, CA, 2003.
- [18] A. W. Cook and W. H. Cabot. A high-wavenumber viscosity for high-resolution numerical methods. *Journal of Computational Physics*, **195**(2):594–601, 2004.
- [19] B. Després and C. Mazeran. Symmetrization of Lagrangian gas dynamic in dimension two and multidimensional solvers. *Comptes Rendus Mécanique*, **331**(7):475–480, 2003.
- [20] B. Després and C. Mazeran. Lagrangian gas dynamics in two dimensions and Lagrangian systems. *Archives of Rational Mechanics and Analysis*, **178**(3):327–372, 2005.
- [21] D. P. Flanagan and T. Belytschko. A uniform strain hexahedron and quadrilateral with orthogonal hourglass control. *International Journal for Numerical Methods in Engineering*, **17**(5):679–706, 1981.
- [22] G. Hauke and T. J. R. Hughes. A unified approach to compressible and incompressible flows. *Computer Methods in Applied Mechanics and Engineering*, **113**:389–396, 1994.
- [23] G. Hauke and T. J. R. Hughes. A comparative study of different sets of variables for solving compressible and incompressible flows. *Computer Methods in Applied Mechanics and Engineering*, **153**:1–44, 1998.
- [24] R. A. Horn and C. R. Johnson. *Matrix Analysis*. Cambridge University Press, Cambridge, UK, 1985.



- [25] T. J. R. Hughes. *The Finite Element Method: Linear Static and Dynamic Finite Element Analysis*. Prentice-Hall, Englewood Cliffs, New Jersey, 1987. (Dover reprint, 2000).
- [26] T. J. R. Hughes. Multiscale phenomena: Green's functions, the Dirichlet-to-Neumann formulation, subgrid-scale models, bubbles and the origin of stabilized methods. *Computer Methods in Applied Mechanics and Engineering*, **127**:387–401, 1995.
- [27] T. J. R. Hughes, G.R. Feijóo, L. Mazzei, and J.-B. Quincy. The Variational Multiscale Method — a paradigm for computational mechanics. *Computer Methods in Applied Mechanics and Engineering*, **166**:3–24, 1998.
- [28] T. J. R. Hughes, L. P. Franca, and G. M. Hulbert. A new finite element formulation for computational fluid dynamics: VIII. The Galerkin/least-squares method for advective-diffusive equations. *Computer Methods in Applied Mechanics and Engineering*, **73**:173–189, 1989.
- [29] T. J. R. Hughes, L. P. Franca, and M. Mallet. A new finite element formulation for computational fluid dynamics: I. Symmetric forms of the compressible Euler and Navier-Stokes equations and the second law of thermodynamics. *Computer Methods in Applied Mechanics and Engineering*, **54**:223–234, 1986.
- [30] T. J. R. Hughes, L. P. Franca, and M. Mallet. A new finite element formulation for computational fluid dynamics: VI. Convergence analysis of the generalized SUPG formulation for linear time-dependent multidimensional advective-diffusive systems. *Computer Methods in Applied Mechanics and Engineering*, **63**:97–112, 1987.
- [31] T. J. R. Hughes and M. Mallet. A new finite element formulation for computational fluid dynamics: III. The generalized streamline operator for multidimensional advective-diffusive systems. *Computer Methods in Applied Mechanics and Engineering*, **58**:305–328, 1986.
- [32] T. J. R. Hughes, M. Mallet, and A. Mizukami. A new finite element formulation for computational fluid dynamics: II. Beyond SUPG. *Computer Methods in Applied Mechanics and Engineering*, **54**:341–355, 1986.
- [33] T. J. R. Hughes, G. Scovazzi, and Franca L.P. Multiscale and stabilized methods. In E. Stein, R. de Borst, and T. J. R. Hughes, editors, *Encyclopedia of Computational Mechanics*. John Wiley & Sons, 2004.
- [34] T. J. R. Hughes and T. E. Tezduyar. Finite element methods for first-order hyperbolic systems with particular emphasis on the compressible Euler equations. *Computer Methods in Applied Mechanics and Engineering*, **45**:217–284, 1984.
- [35] C. Johnson and A. Szepessy. On the convergence of a finite element method for a nonlinear hyperbolic conservation law. *Mathematics of Computation*, **49**:427–444, 1987.
- [36] C. Johnson, A. Szepessy, and P. Hasnbo. On the convergence of shock-capturing streamline diffusion finite element methods for hyperbolic conservation laws. *Mathematics of Computation*, **54**:107–129, 1990.
- [37] H.-O. Kreiss. On difference approximations of the dissipative type for hyperbolic differential equations. *Communications on Pure and Applied Mathematics*, **15**:335–353, 1964.
- [38] G. J. Le Beau, S. E. Ray, S. K. Aliabadi, and T. E. Tezduyar. SUPG finite element computation of compressible flows with the entropy and conservation variables formulations. *Computer Methods in Applied Mechanics and Engineering*, **195**:1621–1632, 2006.
- [39] E. Love and G. Scovazzi. On the angular momentum conservation and incremental objectivity properties of a predictor/multi-corrector method for Lagrangian shock hydrodynamics. *Computer Methods in Applied Mechanics and Engineering*, **198**(41-44):3207–3213, 2009.
- [40] P.-H. Maire. A high-order cell-centered Lagrangian scheme for two-dimensional compressible fluid flows on unstructured meshes. *Journal of Computational Physics*, **228**(7):2391–2425, 2009.
- [41] P.-H. Maire and J. Breil. A second-order cell-centered Lagrangian scheme for two-dimensional compressible flow problems. *International Journal for Numerical Methods in Fluids*, **56**:1417–1423, 2008.
- [42] P.-H. Maire and B. Nkonga. Multi-scale Godunov-type method for cell-centered discrete Lagrangian hydrodynamics. *Journal of Computational Physics*, **228**(3):799–821, 2009.
- [43] L. G. Margolin. A centered artificial viscosity for cells with large aspect ratios. Technical report, UCRL-53882, Lawrence Livermore National Laboratory, 1988.
- [44] L. G. Margolin and M. Shashkov. Second-order sign-preserving conservative interpolation (remapping) on general grids. *Journal of Computational Physics*, **184**(1):266–298, 2003.
- [45] L. G. Margolin and M. Shashkov. Remapping, recovery and repair on a staggered grid. *Computer Methods in Applied Mechanics and Engineering*, **193**(39-41):4139–4155, 2004.
- [46] L. G. Margolin and M. Shashkov. Finite volume methods and the equations of finite scale: A mimetic approach. *International Journal for Numerical Methods in Fluids*, **56**(8):991–1002, 2008.
- [47] R. Menikoff and B. J. Plohr. The Riemann problem for fluid flow of real materials. *Reviews of Modern Physics*, **61**(1):75–130, 1989.
- [48] A. R. Mitchell and D. F. Griffiths. *The Finite Difference Method in Partial Differential Equation*. John Wiley, London, 1980.
- [49] W. F. Noh. Errors for calculations of strong shocks using an artificial viscosity and an artificial heat flux. *Journal of Computational Physics*, **72**:78–120, 1987.
- [50] G. Scovazzi. A discourse on Galilean invariance and SUPG-type stabilization. *Computer Methods in Applied Mechanics and Engineering*, **196**(4–6):1108–1132, 2007.
- [51] G. Scovazzi. Galilean invariance and stabilized methods for compressible flows. *International Journal for Numerical Methods in Fluids*, **54**(6–8):757–778, 2007.
- [52] G. Scovazzi. Stabilized shock hydrodynamics: II. Design and physical interpretation of the SUPG operator for Lagrangian computations. *Computer Methods in Applied Mechanics and Engineering*, **196**(4–6):966–978, 2007.
- [53] G. Scovazzi, M. A. Christon, T. J. R. Hughes, and J. N. Shadid. Stabilized shock hydrodynamics: I. A Lagrangian method. *Computer Methods in Applied Mechanics and Engineering*, **196**(4–6):923–966, 2007.
- [54] G. Scovazzi and E. Love. A generalized view on Galilean invariance in stabilized compressible flow computations. Technical report, SAND2007-5238J, Sandia National Laboratories, New Mexico, 2009. Submitted to International Journal for Numerical Methods in Fluids and available at: <http://www.cs.sandia.gov/~gscovaz/pubs.html>.
- [55] G. Scovazzi, E. Love, and M. J. Shashkov. A multi-scale Q1/P0 approach to Lagrangian shock hydrodynamics. Technical report, SAND2007-1423, Sandia National Laboratories, New Mexico, March 2007. Available at: <http://www.cs.sandia.gov/~gscovaz/pubs.html>.
- [56] G. Scovazzi, E. Love, and M. J. Shashkov. A multi-scale Q1/P0 approach to Lagrangian shock hydrodynamics. *Computer Methods in Applied Mechanics and Engineering*, **197**(9–12):1056–1079, 2008.
- [57] G. Scovazzi, W. J. Rider, E. Love, and J. N. Shadid. Stabilized shock hydrodynamics: V. Von Neumann stability analysis of a predictor/multi-corrector Lagrangian method. *Computer Methods in Applied Mechanics and Engineering*, 2009. Submitted.
- [58] L. I. Sedov. *Similarity and Dimensional Methods in Mechanics*. Academic Press, New York, 1959.
- [59] J. C. Simo and T. J. R. Hughes. *Computational Inelasticity*. Springer, New York, 1998.
- [60] J. C. Strikwerda. *Finite Difference Schemes and Partial Differential Equations*. Chapman & Hall, New York, 1989.
- [61] J.C Strikwerda and B.A. Wade. An extension of the Kreiss matrix theorem. *SIAM Journal on Numerical Analysis*, **25**:1272–1278, 1988.
- [62] A. Szepessy. Convergence of a shock-capturing streamline diffusion finite element method for a scalar conservation law in two space dimensions. *Mathematics of Computation*, **53**:527–545, 1989.
- [63] T. E. Tezduyar and M. Senga. Stabilization and shock-capturing parameters in SUPG formulation of compressible flows. *Computer Methods in Applied Mechanics and Engineering*, **104**:397–422, 1993.
- [64] T. E. Tezduyar, M. Senga, and D. Vicker. Computation of inviscid supersonic flows around cylinders and spheres with the SUPG formulation and YZ $\beta$  shock-capturing. *Computational Mechanics*, **38**:469–481, 2006.
- [65] J. von Neumann and R. D. Richtmyer. A method for the numerical computation of hydrodynamic shocks. *Journal of Applied Physics*, **21**:232–237, 1950.
- [66] M. L. Wilkins. Use of artificial viscosity in multidimensional shock wave problems. *Journal of Computational Physics*, **36**:281–303, 1979.
- [67] S. Wolfram. *The Mathematica Book*. Cambridge University Press, 4th edition, 1999.
- [68] K. Yosida. *Functional Analysis*. Springer, New York, 1995.